ANALYSIS OF OIL LUBRICATED THRUST COLLARS FOR APPLICATION IN INTEGRALLY GEARED COMPRESSORS

A Thesis

by

TRAVIS ALEXANDER CABLE

Submitted to the Office of Graduate and Professional Studies of
Texas A&M University
in partial fulfillment of the requirements for the degree of

MASTER OF SCIENCE

Chair of Committee, Luis San Andrés
Committee Members, Dara Childs
Theofanis Strouboulis
Head of Department, Andreas Polycarpou

August 2015

Major Subject: Mechanical Engineering

ABSTRACT

Integrally geared compressors (IGCs) comprise of single stage impellers installed on the ends of pinion shafts, all driven by a main bull gear (BG) and shaft system. When compared to single shaft multistage centrifugal compressors, the benefits of IGCs include better thermal efficiency, reduced footprint and simple foundation, dispensing with a high speed coupling, as well as better access for maintenance and overhauls. In IGCs the compression of the process gas induces axial loads on the pinion shafts that are transmitted via thrust collars (TCs) to the main drive shaft and balanced by a single thrust bearing. The TCs, located on either side of pinion gears, slightly overlap with the BG outer diameter to form lentil-shaped lubricant-wetted regions.

A numerical model, based on classical thin film lubrication theory, predicts the force response of lubricated thrust collars for use in integrally geared compressors. The predictive model determines performance parameters such as lubricant flow rate, mechanical power loss, peak pressure, lubricant temperature rise, as well as rotordynamic stiffness and damping coefficients for a lubricated TC and bull gear pair. A Newton-Raphson based iterative procedure determines an equilibrium operating position for a given set of TC and BG operating conditions and geometry. Periodic, dynamic displacements from the equilibrium position renders complex dynamic stiffnesses ($H = K+i\omega C$), from which the fluid film force and moment stiffness and damping coefficients are determined.

In a lubricated thrust collar and bull gear, a hydrodynamic pressure builds in the lower half of the lubricated zone and lubricant cavitation occurs in the upper half. The

minimum film thickness and peak pressure in the lubricated zone shift location due to the difference in taper angles between the TC and BG surfaces.

For a given applied load, a study on the differences in taper angle between the TC and BG surfaces reveals that current angular tolerances of $\pm 0.1^{\circ}$ produce TC/BG pairs with similar performance parameters (power loss, lubricant temperature rise, etc.) and dynamic force and moment stiffness and damping coefficients. Increasing the taper angles of both the TC and BG decreases mechanical power loss and lubricant temperature rise, but also decreases the fluid film axial stiffness and damping coefficients. In addition, static angular misalignments of the TC and BG about the horizontal (x) axis joining the BG and TC centers alters the shape and extent of the lubricant cavitation region. This change alters the load carrying capacity and mechanical power losses of the lubricated element.

For the specific TC/BG pair investigated herein, there exists a maximum difference between the two taper angles for which the mechanical element can support an imposed thrust load. Increasing the speed of the BG (and proportionally the TC speed) increases the mechanical power loss and lubricant temperature rise and decreases the fluid film axial stiffness and damping coefficients. As with most fluid film bearings, increasing the applied load increases the power loss, lubricant temperature rise, and axial stiffness and damping coefficients.

The thesis delivers a predictive tool, yet to be benchmarked against experimental data, that provides insight to both the static and dynamic force performance of a lubricated thrust collar, not currently in the archived literature.

DEDICATION

To Michelle, my beautiful wife, for the constant love and encouragement. To my parents for the provision and basis for my continued success and to my sister for sharing in the struggles of school and life. To the Lord, because it was, and is, always His.

ACKNOWLEDGEMENTS

Firstly, I thank Samsung Techwin for the funding and support of this work. In particular, I thank Dr. Karl Wygant and Ms. Yujiao Tao for they provided insight and experience for thrust collars in industry. I am grateful for the encouragement, help and support that Dr. Wygant provided throughout the duration of my research.

I also thank Dr. Luis San Andrés, my committee chair, for his guidance and support throughout the course of this research. In addition, thanks to my committee members, Dr. Theofanis Strouboulis, and Dr. Dara Childs, for taking the time to review and provide valuable insight to my work.

Thanks also go to my friends and colleagues at the Turbomachinery Lab for your friendship and encouragement. In particular, I thank Joshua Norsworthy for sharing in my struggles and successes throughout these two years.

NOMENCLATURE

A^e	Area of a finite element [m^2]
a_T, b_T	Coefficients for solution of thermal energy transport equation [m^3/s]
b	Radius from bull gear center to the lubricated zone [m]
C	Damping coefficient
c_p	Lubricant specific heat at constant pressure [J/kg.°C]
d	$a+b$. Distance between pinion and bull gear centers [m]
F_z	Thrust collar axial reaction force [N]
H	Complex dynamic stiffness ($H = K + i\omega C$)
$\bar{h}$	Heat convection coefficient [$W/m^2.°C$]
h	Film thickness [m]
h_{R1}	Reference distance at the thrust collar outer radius [m]
i	Imaginary unit
K	Stiffness coefficient
M_x, M_y	Moments about x and y axes [N.m]
$\bar{P}$	Nodal pressure [Pa]
p, p_a	Hydrodynamic and ambient pressures [Pa]
p_z, p_α, p_β	Dynamic (first order) pressures [N/m^3, $N/(m^2.rad)$]
Q	Lubricant flow rate [m^3/s]
q	Lubricant flow rates per unit length [m^2/s]
R_1, R_2	TC and Bull gear radii [m]

r,θ,z	Polar coordinate system (radial, angular and axial) with origin at pinion gear center
T	Lubricant temperature [°C]
t	Time [s]
V_r,V_θ,V_z	Fluid film velocity components [m/s]
W	Applied thrust load [N]
x,y,z	Cartesian coordinate system with origin at pinion gear center
α_x, α_y	Thrust collar static misalignment angle about x and y axes [rad]
α_v	Lubricant temperature viscosity coefficient [1/°C]
β_x, β_y	Bull gear misalignment angle about x and y axes [rad]
Γ	Boundary of the lubricated zone
ε	Angle between tangential velocity of bull gear surface and (r,θ) [rad]
$\bar{\kappa}$	Lubricant thermal conductivity [W/m.°C]
η_κ	Change in film thickness associated with perturbation κ [- or m]
μ	Lubricant viscosity [Pa.s]
ρ	Lubricant density [kg/m^3]
φ	Taper angle [rad]
Φ	Mechanical energy dissipation function [W/m^2]
Ψ	Bilinear shape functions
ω	Angular speed [rad/s]
Ω	Area of a finite element

$\wp^e$	Mechanical power loss in a finite element (W)

DIMENSIONLESS VARIABLES

$\bar{C}$	Dimensionless damping coefficient (refer to Eq. 80)
$\bar{K}$	Dimensionless stiffness coefficient (refer to Eq. 81)
f	Friction factor ($\wp / \omega_{TC} W^* R_1$)
$\bar{P}$	Dimensionless pressure ($\bar{P} = p / p^*$)
$\bar{r}$	Dimensionless radial distance ($\bar{r} = r / R_1$)
$\bar{W}$	Dimensionless axial thrust load ($\bar{W} = W / W^*$)
$\bar{\varphi}$	Dimensionless surface taper angle ($\bar{W} = W / W^*$)
Λ	Thrust collar speed number ($\frac{6\mu\omega_{TC} A_{\text{lub}}}{W}\left(\frac{R_1}{h^*}\right)^2$)
$\bar{\omega}$	Dimensionless rotational speed ($\bar{\omega} = \bar{\omega}_{TC} / \bar{\omega}_B$)

SUBSCRIPTS

B	Bull gear
TC	Thrust Collar
i, j	Summation indices
κ	First order (perturbed) quantity (axial or angular).
0	Zeroth order (equilibrium) quantity.

SUPERSCRIPTS

e	Element number within the finite element mesh

VECTORS AND MATRICES

$\vec{n}$	Normal vector
$\vec{s}$	Vector of surface speeds
$\mathbf{C}$	Matrix of force and moment damping coefficients
$\mathbf{f}^{\mathbf{e}}$	Vector of shear flow rates
$\mathbf{H}$	Matrix of complex dynamic stiffnesses ($\mathbf{H} = \mathbf{K} + i\omega\mathbf{C}$)
$\mathbf{K}$	Matrix of force and moment stiffness coefficients
$\mathbf{i, j, k}$	Unit normal vectors (Cartesian coordinate system at pinion center)
$\mathbf{k}^{\mathbf{e}}$	Matrix of fluidity coefficients
$\mathbf{q}^{\mathbf{e}}$	Vector of lubricant flow rates through the boundaries
$\bar{\mathbf{P}}^{\mathbf{e}}$	Vector of nodal pressures

ACRONYMS-ABREVIATIONS

IGC	Integrally geared compressor
TETE	Thermal energy transport equation

TABLE OF CONTENTS

Page

ABSTRACT ii

DEDICATION iv

ACKNOWLEDGEMENTS v

NOMENCLATURE vi

TABLE OF CONTENTS x

LIST OF FIGURES xii

LIST OF TABLES xviii

INTRODUCTION 1

TASKS 4

LITERATURE REVIEW 6

LUBRICATED THRUST COLLAR MODEL 14

- Film Thickness 14
- Reynolds Equation 17
- Thermal Energy Transport Equation 18
- Mechanical Energy Dissipation Function 21
- Axial Force and Moments on the Thrust Collar Surface 24
- Thrust Collar Stiffness and Damping Coefficients 27

NUMERICAL FORMULATION 33

- Reynolds Equation 33
- Thermal Energy Transport Equation 36

PREDICTIONS FOR THE PERFORMANCE OF A STATICALLY ALIGNED THRUST COLLAR 40

- Normalized Parameters 40
- Hydrodynamic Pressure and Film Thickness Profiles 42
- Effect of Taper Angles on the Performance of a Lubricated Thrust Collar 49

PREDICTIONS FOR THE PERFORMANCE OF A STATICALLY MISALIGNED THRUST COLLAR 66

PREDICTIONS FOR THE PERFORMANCE OF A TYPICAL THRUST COLLAR AND BULL GEAR PAIR FOR VARIOUS LOADS AND ROTATIONAL SPEEDS 85

CONCLUSIONS 96

REFERENCES 100

APPENDIX A: COMPUTER IMPLEMENTATION 102

Newton-Raphson Iterative Scheme 104

APPENDIX B: MODEL FOR HEAT CONVECTION COEFFICIENTS 106

LIST OF FIGURES

Page

Figure 1. Cut view of a two stage integrally geared compressor [1].....1

Figure 2. Schematic view of an integrally geared compressor with thrust collars and thrust bearing depicted. 3

Figure 3. Test rig for measuring frictional torque between a thrust washer and driven gear [9-11]. 10

Figure 4. Depiction of lubricated (non-contacting) zone for a thrust collar and bull gear. 14

Figure 5. Schematic view of the lubricated zone for a thrust collar and bull gear along the line $\theta = 0$. 15

Figure 6. Depiction of a thrust collar with (a) no misalignment (b) angular misalignment (α_x) about the x axis and (c) angular misalignment (α_y) about the y axis.....16

Figure 7. Depiction of a thrust collar with (a) no static misalignment and bull gear with (b) angular misalignment (β_x) about the x axis and (c) angular misalignment (β_y) about the y axis. 17

Figure 8. Schematic view of a fluid traction component (t_θ) at the thrust collar surface (taper angles not depicted for simplicity).....22

Figure 9. Schematic representation of [a] imposed axial force on the thrust collar in the y-z plane and [b] a hydrodynamic pressure field (P) acting on the thrust collar surface.. 25

Figure 10. Typical finite element mesh of the lubricated zone and a single control volume comprised of a row of finite elements. 36

Figure 11. Schematic side views of thrust collars with different taper angles. 43

Figure 12. Contour plots of [a] hydrodynamic pressure and [b] film thickness in a thrust collar with $\left(\bar{\varphi}_B/\bar{\varphi}_{TC}\right)=1.0$. $\bar{W}=1,\bar{\omega}=10,R_2/R_1=7.14$. 46

Figure 13. Contour plots of [a] hydrodynamic pressure and [b] film thickness in a thrust collar with $\left(\bar{\varphi}_B/\bar{\varphi}_{TC}\right)$=1.2. $\bar{W}=1,\bar{\omega}=10,R_2/R_1=7.14$. 47

Figure 14. Contour plots of [a] hydrodynamic pressure and [b] film thickness in a thrust collar with $\left(\bar{\varphi}_B/\bar{\varphi}_{TC}\right)$=0.8. $\bar{W}=1,\bar{\omega}=10,R_2/R_1=7.14$. 48

Figure 15. Minimum film thickness ($\bar{h}_{\min}$) versus thrust collar taper angle ($\bar{\varphi}_{TC}$) for five taper angle configurations. $\bar{W}=1,\bar{\omega}=10,R_2/R_1=7.14$. 50

Figure 16. Peak pressure ($\bar{P}_{\max}$) versus thrust collar taper angle ($\bar{\varphi}_{TC}$) for five taper angle configurations. $\bar{W}=1,\bar{\omega}=10,R_2/R_1=7.14$. 51

Figure 17. Friction factor (*f*) versus thrust collar taper angle ($\bar{\varphi}_{TC}$) for five taper angle configurations. $\bar{W}=1,\bar{\omega}=10,R_2/R_1=7.14$. 52

Figure 18. Lubricant flow rate ($\bar{Q}$) versus thrust collar taper angle ($\bar{\varphi}_{TC}$). $\bar{W}=1,\bar{\omega}=10,R_2/R_1=7.14$. 53

Figure 19. Lubricant temperature rise ($\Delta\bar{T}$) versus thrust collar taper angle ($\bar{\varphi}_{TC}$). $\bar{W}=1,\bar{\omega}=10,R_2/R_1=7.14$. 54

Figure 20. Axial stiffness ($\bar{K}_{zz}$) versus thrust collar taper angle ($\bar{\varphi}_{TC}$).
$\bar{W}=1, \bar{\omega}=10, R_2/R_1=7.14$ 55

Figure 21. Moment Angle stiffness [a] $\overline{K}_{\alpha_x\alpha_x}, \overline{K}_{\alpha_x\alpha_y}, \overline{K}_{\alpha_y\alpha_x}$ and [b] $\overline{K}_{\alpha_y\alpha_y}$ versus thrust collar taper angle ($\bar{\varphi}_{TC}$). $\bar{W}=1, \bar{\omega}=10, R_2/R_1=7.14$ 57

Figure 22. Axial-angular stiffness [a] $\overline{K}_{\alpha_x z}$, $\overline{K}_{z\alpha_x}$ and [b] $\overline{K}_{\alpha_y z}, \overline{K}_{z\alpha_y}$ versus thrust collar taper angle ($\bar{\varphi}_{TC}$). $\bar{W}=1, \bar{\omega}=10, R_2/R_1=7.14$ 59

Figure 23. Axial damping ($\bar{C}_{zz}$) versus thrust collar taper angle ($\bar{\varphi}_{TC}$).
$\bar{W}=1, \bar{\omega}=10, R_2/R_1=7.14$ 60

Figure 24. Moment-angle damping [a] $\overline{C}_{\alpha_x\alpha_x}, \overline{C}_{\alpha_x\alpha_y}, \overline{C}_{\alpha_y\alpha_x}$ and [b] $\overline{C}_{\alpha_y\alpha_y}$ versus thrust collar taper angle ($\bar{\varphi}_{TC}$). $\bar{W}=1, \bar{\omega}=10, R_2/R_1=7.14$ 62

Figure 25. Force and moment velocity damping [a] $\overline{C}_{z\alpha_x}, \overline{C}_{\alpha_x z}$ and [b] $\overline{C}_{z\alpha_y}, \overline{C}_{\alpha_y z}$ versus thrust collar taper angle ($\bar{\varphi}_{TC}$). $\bar{W}=1, \bar{\omega}=10, R_2/R_1=7.14$ 64

Figure 26. Contour plots of film thickness in the lubricated zone for a TC and BG with angular misalignment about the *x* axis. Properties and operating conditions as in Table 1. $\bar{W}=1.0$, $\bar{\varphi}_{TC}=\bar{\varphi}_B=1.0$, $\bar{\omega}$=10 68

Figure 27. Contour plots of hydrodynamic pressure in the lubricated zone for a TC and BG with angular misalignment about the *x* axis. Properties and operating conditions as in Table 1. $\bar{W}=1.0$, $\bar{\varphi}_{TC}=\bar{\varphi}_B=1.0$, $\bar{\omega}$=10 69

Figure 28. Schematic views of the lubricated zone in which there is (a) no angle misalignment and (b) misalignment of the BG about the vertical axis ($\beta_y > 0$). 71

Figure 29. Normalized film thickness ($\bar{h}_{\min}$) versus [a] TC misalignment angle $\bar{\alpha}_x$, [b] BG misalignment angle $\bar{\beta}_x$, [c] TC misalignment angle $\bar{\alpha}_y$ and [d] BG misalignment angle $\bar{\beta}_y$. $\bar{W} = 1, \bar{\omega} = 10,\ R_2/R_1 = 7.14,\ \bar{\varphi}_{TC} = \bar{\varphi}_B = 1.0$. 73

Figure 30. Peak pressure ($\bar{P}_{\max}$) versus thrust collar misalignment angle ($\bar{\alpha}_x$ or $\bar{\alpha}_y$). $\bar{W} = 1, \bar{\omega} = 10,\ R_2/R_1 = 7.14,\ \bar{\varphi}_{TC} = \bar{\varphi}_B = 1.0$. 75

Figure 31. Friction factor (*f*) versus thrust collar misalignment angle ($\bar{\alpha}_x$ or $\bar{\alpha}_y$). $\bar{W} = 1, \bar{\omega} = 10,\ R_2/R_1 = 7.14,\ \bar{\varphi}_{TC} = \bar{\varphi}_B = 1.0$. 76

Figure 32. Lubricant flow rate ($\bar{Q}$) versus thrust collar misalignment angle ($\bar{\alpha}_x$ or $\bar{\alpha}_y$). $\bar{W} = 1, \bar{\omega} = 10,\ R_2/R_1 = 7.14,\ \bar{\varphi}_{TC} = \bar{\varphi}_B = 1.0$ 77

Figure 33. Lubricant temperature rise ($\Delta\bar{T}$) versus thrust collar misalignment angle ($\bar{\alpha}_x$ or $\bar{\alpha}_y$). $\bar{W} = 1, \bar{\omega} = 10,\ R_2/R_1 = 7.14,\ \bar{\varphi}_{TC} = \bar{\varphi}_B = 1.0$ 78

Figure 34. Axial stiffness ($\bar{K}_{zz}$) versus thrust collar misalignment angle ($\bar{\alpha}_x$ or $\bar{\alpha}_y$). $\bar{W} = 1, \bar{\omega} = 10,\ R_2/R_1 = 7.14,\ \bar{\varphi}_{TC} = \bar{\varphi}_B = 1.0$. 79

Figure 35. Moment Angle stiffness versus thrust collar misalignment angle ($\bar{\alpha}_x$ or $\bar{\alpha}_y$). $\bar{W} = 1, \bar{\omega} = 10,\ R_2/R_1 = 7.14,\ \bar{\varphi}_{TC} = \bar{\varphi}_B = 1.0$ 80

Figure 36. Axial-angular stiffness versus thrust collar misalignment angle ($\bar{\alpha}_x$ or $\bar{\alpha}_y$). $\bar{W} = 1, \bar{\omega} = 10,\ R_2/R_1 = 7.14,\ \bar{\varphi}_{TC} = \bar{\varphi}_B = 1.0$ 81

Figure 37. Axial damping ($\bar{C}_{zz}$) versus thrust collar misalignment angle ($\bar{\alpha}_x$ or $\bar{\alpha}_y$). $\bar{W}=1, \bar{\omega}=10,\ R_2/R_1=7.14,\ \bar{\varphi}_{TC}=\bar{\varphi}_B=1.0$ 82

Figure 38. Moment-angle damping ($\bar{C}_{\alpha_x\alpha_x}, \bar{C}_{\alpha_y\alpha_y}, \bar{C}_{\alpha_x\alpha_y}, \bar{C}_{\alpha_y\alpha_x}$) versus thrust collar misalignment angle ($\bar{\alpha}_x$ or $\bar{\alpha}_y$). $\bar{W}=1, \bar{\omega}=10,\ R_2/R_1=7.14,\ \bar{\varphi}_{TC}=\bar{\varphi}_B=1.0$ ... 83

Figure 39. Force and moment-angle velocity damping ($\bar{C}_{z\alpha_x}, \bar{C}_{z\alpha_y}, \bar{C}_{\alpha_x z}, \bar{C}_{\alpha_y z}$) versus thrust collar misalignment angle ($\bar{\alpha}_x$ or $\bar{\alpha}_y$). $\bar{W}=1, \bar{\omega}=10,\ R_2/R_1=7.14,\ \bar{\varphi}_{TC}=\bar{\varphi}_B=1.0$. 84

Figure 40. Normalized load capacity versus normalized taper angles difference ($\Delta\bar{\varphi}=\bar{\varphi}_B-\bar{\varphi}_{TC}$). $\bar{\omega}=10,\ R_2/R_1=7.14,\ \bar{\varphi}_{TC}=1.0$ 86

Figure 41. Minimum film thickness ($\bar{h}_{\min}$) versus TC speed ($\bar{\omega}_{TC}$) for three loads. $\bar{\omega}=10,\ \bar{\varphi}_{TC}=\bar{\varphi}_B=2.0, \alpha_x=\alpha_x=\beta_x=\beta_y=0$. 88

Figure 42. Peak pressure ($\bar{P}_{\max}$) versus TC speed ($\bar{\omega}_{TC}$) for three loads. $\bar{\omega}=10,\ \bar{\varphi}_{TC}=\bar{\varphi}_B=2.0, \alpha_x=\alpha_x=\beta_x=\beta_y=0$. 89

Figure 43. Friction factor (*f*) versus TC speed ($\bar{\omega}_{TC}$) for three loads. $\bar{\omega}=10,\ \bar{\varphi}_{TC}=\bar{\varphi}_B=2.0, \alpha_x=\alpha_x=\beta_x=\beta_y=0$. 90

Figure 44. Lubricant flow rate ($\bar{Q}$) versus TC speed ($\bar{\omega}_{TC}$) for three loads. $\bar{\omega}=10,\ \bar{\varphi}_{TC}=\bar{\varphi}_B=2.0, \alpha_x=\alpha_x=\beta_x=\beta_y=0$. 91

Figure 45. Lubricant temperature rise ($\Delta\bar{T}$) versus TC speed ($\bar{\omega}_{TC}$) for three loads. $\bar{\omega}=10,\ \bar{\varphi}_{TC}=\bar{\varphi}_B=2.0, \alpha_x=\alpha_x=\beta_x=\beta_y=0$. 92

Figure 46. Axial stiffness ($\bar{K}_{zz}$) versus TC speed ($\bar{\omega}_{TC}$) for three loads.
$\bar{\omega} = 10,\ \bar{\varphi}_{TC} = \bar{\varphi}_B = 2.0, \alpha_x = \alpha_x = \beta_x = \beta_y = 0$ 93

Figure 47. Axial damping ($\bar{C}_{zz}$) versus TC speed ($\bar{\omega}_{TC}$) for three loads.
$\underline{\omega} = 10,\ \varphi_{TC} = \varphi_B = 2.0, \alpha_x = \alpha_x = \beta_x = \beta_y = 0$ 94

Figure 48. Axial damping ratio (ζ) versus TC speed ($\bar{\omega}_{TC}$) for three loads.
$\bar{\omega} = 10,\ \bar{\varphi}_{TC} = \bar{\varphi}_B = 2.0, \alpha_x = \alpha_x = \beta_x = \beta_y = 0$ 95

Figure A1. Flow chart for determining the operating film thickness and performance parameters of a lubricated thrust collar. 103

Figure B1. Depiction of the lubricated zone between a thrust collar and bull gear as a parallel channel. 107

LIST OF TABLES

Page

Table 1. Bull gear and thrust collar operating conditions, geometric ratios, and lubricant properties……..……....44

INTRODUCTION*

Figure 1 shows a typical two stage integrally geared compressor (IGC) with thrust collars. Industry prefers IGCs for their increased thermal efficiency, decreased footprint, and ease of access for maintenance and overhaul. In an IGC, the main bull gear (BG) drives pinion shafts, each having single stage centrifugal compressors at its ends.

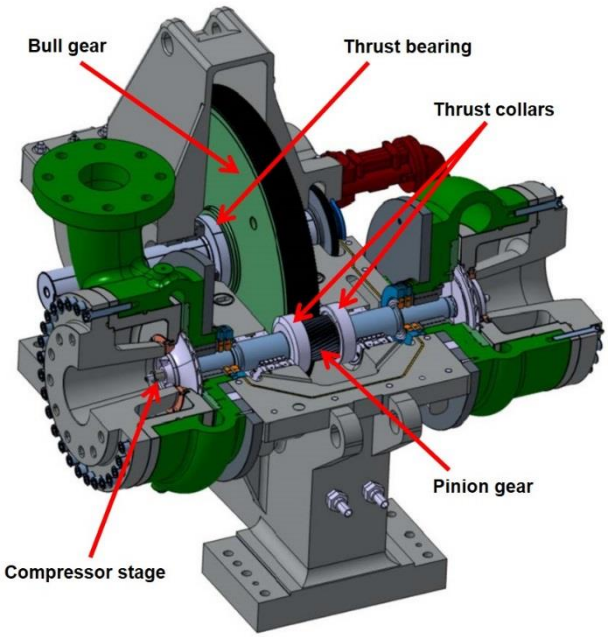

Figure 1. Cut view of a two stage integrally geared compressor [1,12].

* Portions of this work are reproduced from San Andrés, L, Cable, T.A., Wygant, K. and Morton, A., 2015, "On the Predicted Performance of Oil Lubricated Thrust Collars in Integrally Geared Compressors," ASME J. Eng. Gas Turbines Power, vol. 137 (5), pp. 1-9 [12].

The compression of process gas in each compressor generates axial thrust loads along the pinion shafts that must be balanced to prevent contact between the bull gear and thrust collars in the compressor casing. Thrust collars (TCs), press fit on either side of pinion gears (see Figure 2), slightly overlap with the bull gear to form a small area where lubricant prevents the surfaces from colliding. In the lubricated area, the rotation of the TC and BG generates a hydrodynamic pressure field opposing the axial thrust load along the pinion shaft.

Figure 2 displays a schematic view of a typical TC arrangement in an integrally geared compressor with one pinion shaft. The BG and its drive shaft rotate with angular speed ω_B, and the pinion shaft with angular speed ω_P. Both speeds relate by $\omega_B N_B = \omega_P N_P$ with N denoting the number of teeth in a gear. Since the thrust collar rides on the same shaft as the pinion gear, $\omega_P = \omega_{TC}$. In Figure 2, notice the small clearance between the pinion gear and the TC that fills with lubricant.

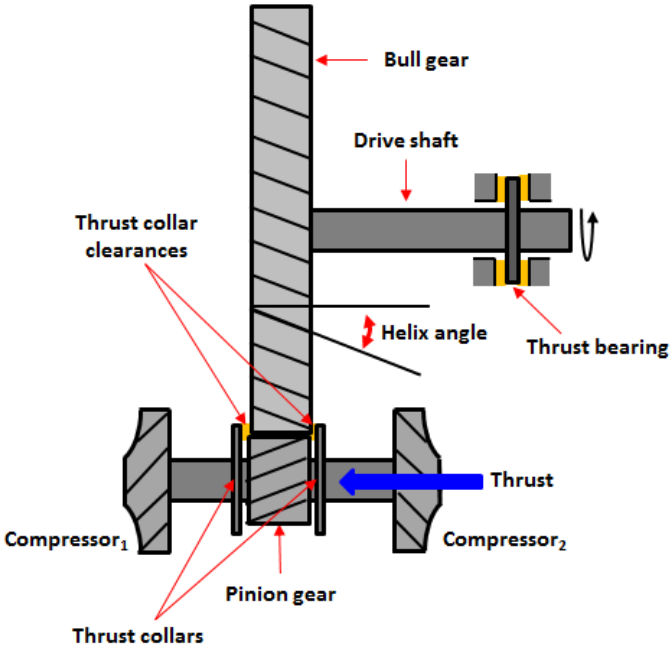

Figure 2. Schematic view of an integrally geared compressor with thrust collars and thrust bearing depicted [12].

TASKS

The present work advances an analysis for prediction of the performance of oil lubricated, radially tapered thrust collars (TCs) in IGCs. The performance of a lubricated TC is determined by operating parameters such as lubricant flow rate, drag friction factor, minimum film thickness, mechanical power loss, temperature rise, as well as the axial force and moment coefficients (stiffness and damping) for both aligned and misaligned configurations. The following tasks define a comprehensive model to assess the performance of lubricated thrust collars.

a) The physical analysis for the thin film flow in a lubricated thrust collar assumes a thin film condition under laminar flow and disregards fluid inertia effects. A Finite Element approach solves the Reynolds equation to predict the pressure field and reaction load, and a control volume approach solves the thermal energy transport equation to predict the temperature field (and update the fluid viscosity). Steady-state performance characteristics include the prediction of minimum film thickness, drag friction coefficient, maximum film temperature rise, and peak hydrodynamic pressure for specified thrust load conditions.
b) Develop a perturbation analysis (small amplitude axial and angular displacements) of the thrust collar about an equilibrium operating position yields both zeroth and first order equations for the flow field. Integration of the first order pressure fields on the lubricated surface predicts the thrust collar axial force and moment stiffness and damping coefficients.
c) Assess the effect of static misalignment from the bull gear or the thrust collar on the forced performance of the lubricated mechanical element. Analysis provides

performance characteristics for a lubricated thrust collar as a function of the degree of surface misalignment.

d) Perform parametric studies to determine radial taper angle configurations, for both the bull gear and thrust collar, producing desirable performance such as low power loss, minimum fluid film temperature rise, etc.

LITERATURE REVIEW

Common applications of thrust collars/thrust washers in industry include integrally geared compressors, vertical pumps, and passenger vehicle transmissions. In an integrally geared compressor with a helical gear pair, the helix angle of the gear teeth along with the axial thrust from the compressor stages generate the axial load sustained by the thrust collars on either side of the pinion gear (refer to Figure 2).

The current research on thrust collars in integrally geared compressors aims to determine the performance of the thrust collars operating with a full fluid film between the bull gear and thrust collar. This brief literature review focuses on the analytical and experimental research conducted on thrust collars and thrust washers.

In 1968 Sadykovand and Shneerson [2] investigated the performance of different thrust collar geometries in a helical gear transmission. The authors use single helical gears with the thrust collars fixed to the pinion shaft with taper angles from 30 minutes of arc ($1\ \text{MOA} = {}^{1}\!/_{60}\ \text{degrees}$) to 1° from the vertical plane. Sadykov and Shneerson state outright that no method is known for calculating the load carrying capacity of a thrust collar, so the authors present a table of experimentally determined parameters for the selection of the optimum thrust collar geometry for a given load and rotational speed. This table presents the displacement of the thrust collar for seven configurations; each configuration with a thrust collar affixed to the shaft in a different manner (i.e., clamping

nut or a different interference fit, for example) and a force is applied at various circumferential locations along the thrust collar. The authors derive a formula for the calculation of the appropriate diametric interference fit by approximating the collar as an infinitely wide cantilever plate.

Fingerhut et al. [3] describe the function and design considerations for modern integrally geared turbomachines (IGTMs). The authors discuss the importance of thrust collars as an efficient method of balancing the axial thrust that results from the helix angle of the gear pair as well as the thrust generated by the compressor stages. In IGTMs with multiple pinion shafts, thrust collars provide a balance of forces between all of the shafts, allowing the total thrust load in the compressor to be transferred to the thrust bearing on the bull gear shaft. When compared to large diameter hydrodynamic thrust bearings, thrust collars save space and complexity.

Dietz and Mupende [4] discuss the use of thrust collars for implementation in gearboxes for marine propulsion as a weight and cost saving alternative to thrust bearings. The authors state that thrust collars decrease power losses in high-power transmission gearboxes and offer promise to applications for passenger vehicles. For relatively low loads, the thrust collar should be simply press fit onto the shaft, whereas for higher axial loads the thrust collar should be press fit as well as affixed by another means, such as with a safety ring or shoulder.

Dietz and Mupende [4] use Kirchoff's plate theory to analyze the deformation of TCs under a certain load. The authors warn that the simple plate theory assumes a linear

load distribution along the TC, and as such may not accurately model the loading of the TC under actual operating conditions. Using both commercial finite element software as well as an analytical model, a TC made of high-strength, heat-treated steel is analyzed to determine the axial load at which the connection between the TC and the pinion shaft fails, and the TC slips axially. The results show that the addition of a safety ring close to the press fit TC increases the load carrying capacity before the TC slips. When compared with a simple press fit, welding the TC to the shaft increases the axial load capability before the weld gives. Adding a shoulder near the TC also increases load carrying capacity.

Thoden [5, 6] conducts an elastohydrodynamic (EHD) analysis of the fluid flow between a tapered thrust collar and bull gear to determine an optimal geometry with regards to rotational speed and axial load. Thoden determines the relative velocity between the thrust collar and the bull gear at the contact zone and proceeds to analyze the pressure distribution via EHD analysis. Thoden, for simplicity, uses an empirical temperature correction factor, based on the lubricant thermal conductivity and a temperature-viscosity coefficient. For a thrust collar diameter of 440 mm, a rotational speed of 200 rpm and an axial force of 10,000N, the predicted minimum film thickness is ~18 μm. Thoden also derives the frictional force in the fluid film region from the shear stress and the speeds' difference, as well as the coefficient of friction from the frictional force and the area of the lubricated region.

For a different application, Kucinschi, DeWitt and Pascovici [7] examine the thermoelastohydrodynamic (TEHD) behavior of a radially grooved thrust washer. The numerical evaluation solves the thermal energy transport equation in three dimensions and the Reynolds equation considering elastic deformation of the stator with finite elements. The predictions for the TEHD model shows that the deformation of the entire stator surface (0-360°) allows for hydrodynamic pressure generation over the entire area rather than just at the grooves. Compared to the results from the thermohydrodynamic (THD) model with no elastic deformation, the hydrodynamic pressure in the radial grooves for the TEHD case is almost half as large. This result in Ref. [7] demonstrates that local elastic deformations have a large effect on the hydrodynamic pressures generated in a lubricated thrust washer.

Jackson and Green [8, 9, 10] conduct a series of numerical analyses and experiments on flat faced thrust washers in the gear transmissions of passenger vehicles. Figure 3 shows the test rig and schematic of the thrust washer between a driving gear and carrier [8, 9]. The flat faced thrust washer rides on the same shaft as the driven gear. Lubricant is supplied to the interface between the thrust washer and the driven gear, and the thrust washer absorbs an axial load on the driven shaft.

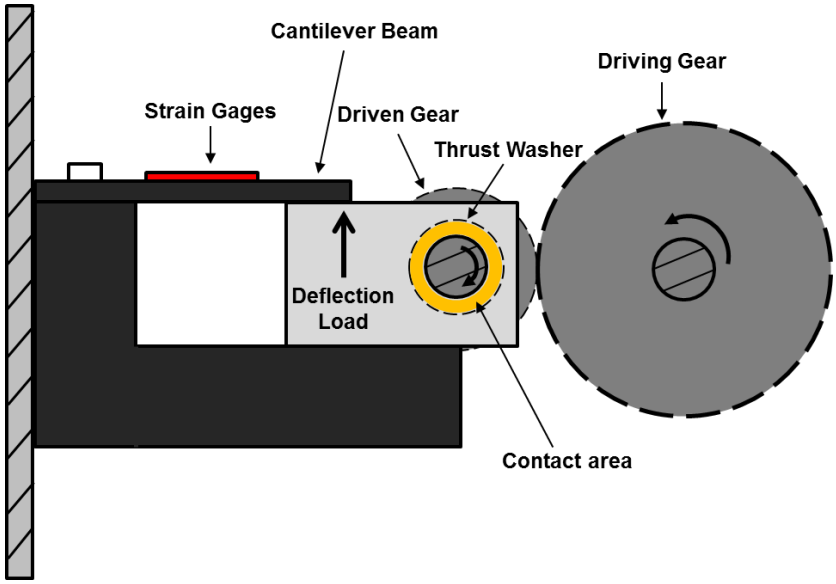

Figure 3. Test rig for measuring frictional torque between a thrust washer and driven gear [8-10].

In Ref. [8], Jackson and Green determine experimentally the parameters that distress a flat faced thrust washer between a helical gear and its carrier. The test rig consists of a single helical gear pair, a carrier and a strain gauge to measure the frictional torque generated by the driving gear. The test rig also incorporates several thermocouples. Jackson and Green measure the frictional torque on the thrust washer in three tests. First, only the load is increased while the operational speed is held constant; in the second test the load is held constant while the speed is increased; and in the third test, the speed and load are both increased simultaneously until distress is achieved. The results of the experiments show that an increase in rotational speed and load cause thrust washer distress due to increased friction as well as actual metal to metal contact. In conclusion,

Jackson and Green identify the presence of both hydrodynamic and elastohydrodynamic effects between the thrust washer and helical gear.

In Ref. [9] Jackson and Green develop a numerical simulation to compare analytical results against the prior experimentally obtained results [8]. Jackson and Green consider operation of the lubricated contact in the boundary lubrication, mixed lubrication and the full film lubrication regimes. The first case considered is boundary lubrication, where the asperities on one surface are in sliding contact with the other surface and disrupt the thin film that forms between the thrust washer and gear face. For this model, a finite difference method is used. The authors allow the lubricant viscosity to vary with temperature but not pressure. In high-pressure contacts, the lubricant viscosity generally varies with pressure; however, Jackson and Green use the Roelands equation for viscosity, which is pressure independent. In the Roelands temperature-viscosity model, the coefficients (G_0 and S_0) are determined experimentally with the lubricant used during the thrust washer experiments (common transmission fluid). The results show the typical results for hydrodynamic bearings mainly that as the applied load increases, the film thickness decreases, the film temperature increases and eventually solid contact occurs. For low rotational speeds (545 rad/s) “lift off” occurs shortly after start up, but the hydrodynamic lift separating the two surfaces is overcome when loads in excess of 500 N are applied and solid contact between the thrust washer and the disk occurs. When the rotational speed increases to 1,367 rad/s it takes a load of 1,750N for contact to occur. Numerical results do not correlate well with the experimental results in Ref. [9]. The

authors posit that the discrepancy in the results is likely because the numerical model does not consider macro scale deformation of the thrust washer due to solid contact.

In Ref. [10] Jackson and Green consider thermo-elastic deformations of the thrust washer. The same numerical scheme developed in [9] is used to solve the system of equations for pressure, temperature, and film thickness. However, before the iterative scheme is run the commercial FE program ANSYS is implemented to model the three dimensional deformations of the thrust washer for a given load. For a load range of 261 N-1,239 N and a rotational speed range of 1,300 rpm to 13,000 rpm, calculated Stribeck curves compare the numerical results to the previously obtained experimental results in [9]. The form of the predictions and experimental data in the Stribeck curve agree, and show the transition between boundary lubrication and full film lubrication. The numerical solution and experimental results show that a thermoelastic instability (TEI) occurs for the thrust washer at an increased surface speed and high loads. This TEI causes the thin film between the two surfaces to collapse with an immediate distress of the thrust washer.

Yu and Sadeghi [11] investigate the thermohydrodynamic performance of a thrust washer bearing with radial grooves. This analysis, unlike the one of Jackson and Green, considers the thrust washer to be parallel to the runner with the generation of hydrodynamic pressure only occurring at grooves evenly distributed around the radius of the washer. As in Ref. [7], the simplifying assumptions do not allow for the deformation of the runner or the thrust washer. In Ref. [7] the thrust washer surface is rigid for

“simplicity”, however Yu and Sadeghi do not state the reason for this simplifying assumption outright. The authors do consider the effects of lubricant cavitation within the fluid domain at the exit of the radial grooves. Yu and Sadeghi [11] use the Elrod cavitation model in the numerical solution along with the modified Reynolds equation and the 3D thermal energy transport equation. Ref. [11] displays three different situations, adiabatic pad and runner, plastic pad, and steel pad. The predictions show that as the lubricant temperature increases (i.e is not carried away via conduction or convection) that the load carrying capacity of the thrust washer is greatly decreased, and that the cavitation zone covers a smaller area of the washer. The viscosity of the fluid varies only with temperature as in Refs. [8, 9, 10].

From the brief review of the available literature on thrust collars and thrust washers, little information is in circulation about the design of radially tapered thrust collars or their optimization for use in integrally geared compressors. The majority of publications focus on flat faced thrust washers in passenger vehicle transmissions. Thoden [5] has performed the most extensive review on tapered thrust collars; his model must be extended to include taper on the bull gear surface. The effect of both thrust collar and bull gear taper angles needs to be assessed to aid in the design of efficient machines (IGCs).

LUBRICATED THRUST COLLAR MODEL

Film Thickness

Figure 4 depicts a typical thrust collar, bull gear and pinion gear arrangement. The parameter *d* refers to the fixed distance between the centers of the bull gear (*B*) and pinion gear (*P*). The lubricated area lies inside the intersection of two arcs; one with radius R_1 denoting the outer radius of the thrust collar, and another with radius R_2, the outer radius of the bull gear. For the current analysis, polar coordinates (r, θ, z) with origin at *P*, the center of the pinion gear, serve to define the boundaries of the lubricated zone, and the film thickness (*h*) within the lubricated thrust zone [12].

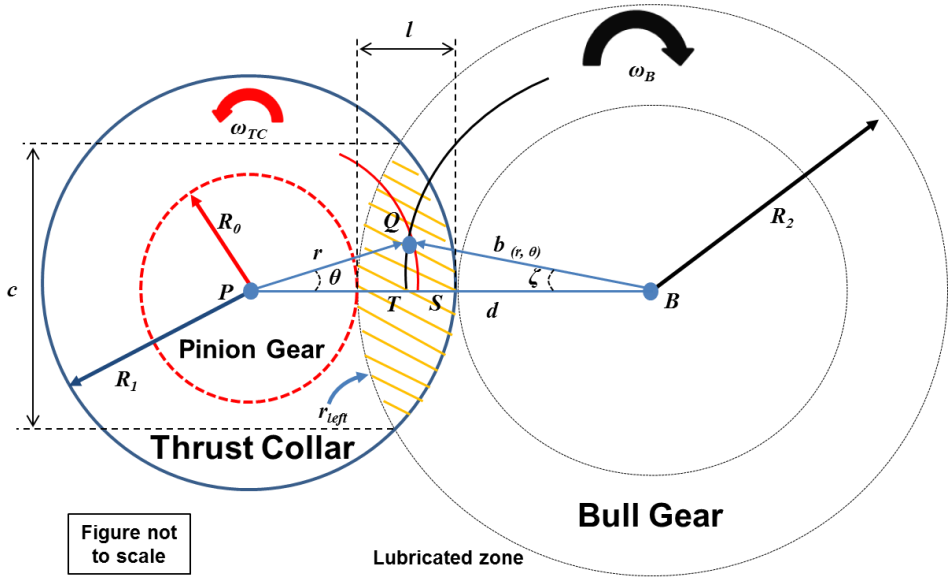

Figure 4. Depiction of lubricated (non-contacting) zone for a thrust collar and bull gear [12].

In Figure 4, Q represents an arbitrary point in the fluid film zone, with r as a radius from P to Q. The parameter $b_{(r,\theta)}$ is a radius from the bull gear center (B) to point Q and is $b_{(r,\theta)} = \sqrt{d^2 + r^2 - 2rd\cos(\theta)}$. Figure 5 shows a schematic view of the fluid film region between a TC and BG pair. The film thickness extends from the TC surface to the BG surface, and is

$$h(r,\theta) = h_{R_1} + (R_1 - d + b)\tan(\varphi_B) - (R_1 - r)\tan(\varphi_{TC}) \quad (1)$$

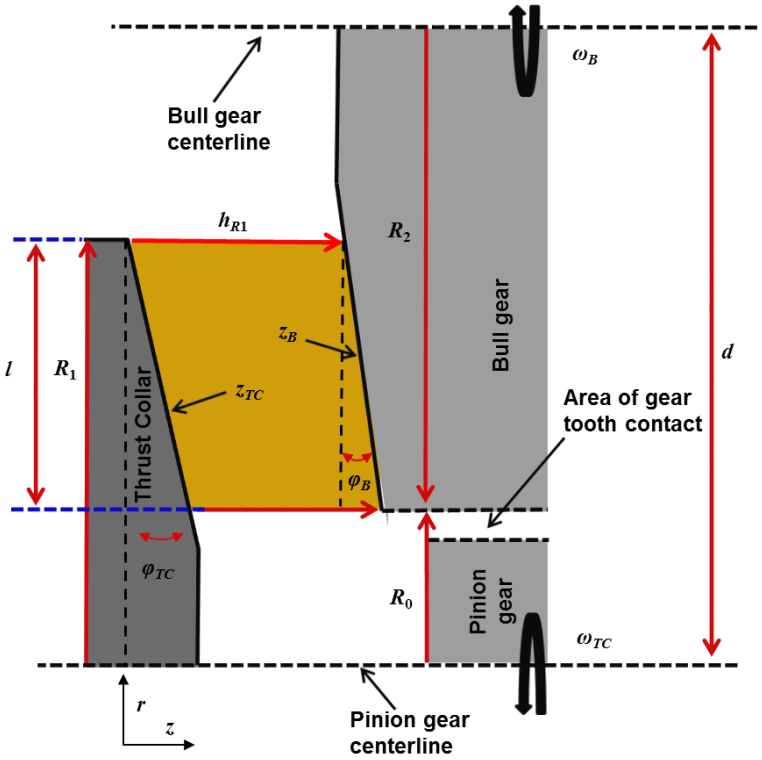

Figure 5. Schematic view of the lubricated zone for a thrust collar and bull gear along the line θ = 0.

If small static angular misalignments (tilts) of the thrust collar or bull gear are introduced, as in Figures 6 and 7 below, the film thickness equation becomes

$$h(r,\theta) = h_{R_1} + (R_1 - d + b)\tan(\varphi_B) - (R_1 - r)\tan(\varphi_{TC}) + r\cos(\theta)\{\alpha_y - \beta_y\} + d\ \beta_y + r\sin(\theta)\{\beta_x - \alpha_x\} \quad (2)$$

where angles (α_x, α_y) refer to static misalignments (or tilts) of the TC, and angles (β_x, β_y) refer to static misalignments (or tilts) of the BG about the *x* and *y* axes, respectively.

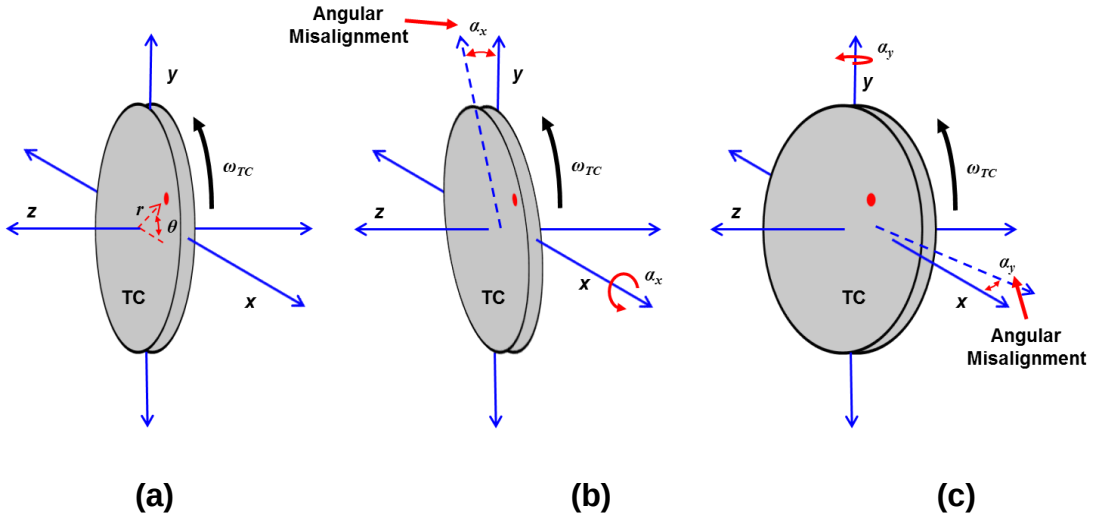

Figure 6. Depiction of a thrust collar with (a) no misalignment (b) angular misalignment (α_x) about the *x* axis and (c) angular misalignment (α_y) about the *y* axis.

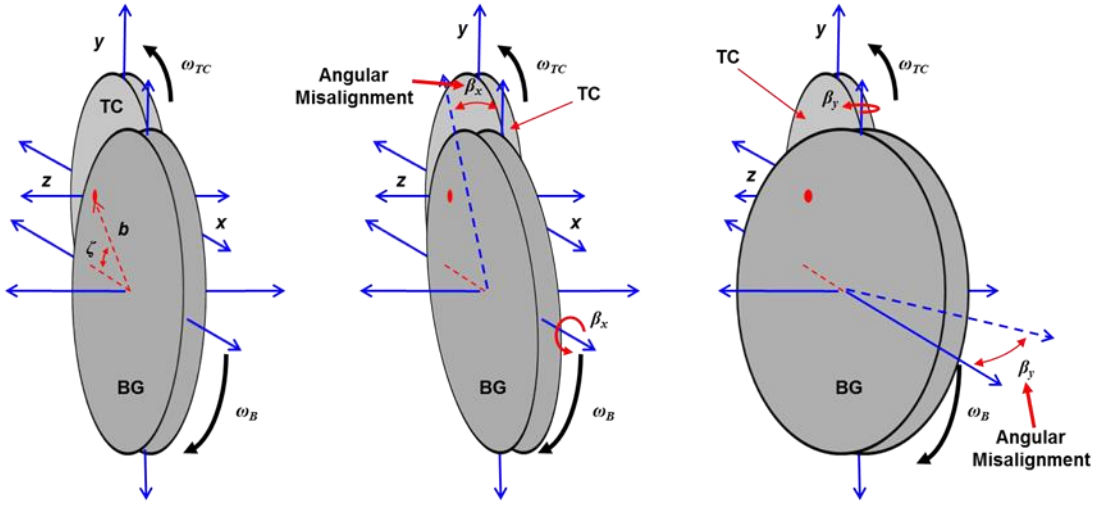

Figure 7. Depiction of a thrust collar with (a) no static misalignment and bull gear with (b) angular misalignment (β_x) about the *x* axis and (c) angular misalignment (β_y) about the *y* axis.

Reynolds Equation

The equation of flow continuity in cylindrical coordinates for an incompressible fluid is [13]

$$\frac{1}{r}\frac{\partial}{\partial r}(rV_r)+\frac{1}{r}\frac{\partial}{\partial \theta}(V_\theta)+\frac{\partial}{\partial z}(V_z)=0 \qquad (3)$$

Classical lubrication disregards fluid inertia effects, and in a thin film region ($h <<< R_1$, R_2), shows that the momentum transport equations reduce to [13]

$$\frac{\partial p}{\partial r}=\frac{\partial}{\partial z}\left(\mu\frac{\partial V_r}{\partial z}\right)\ ;\ \frac{1}{r}\frac{\partial p}{\partial \theta}=\frac{\partial}{\partial z}\left(\mu\frac{\partial V_\theta}{\partial z}\right)\ ;\ \frac{\partial p}{\partial z}\approx 0 \qquad (4)$$

Integrating the momentum transport equations across the film thickness and applying no-slip boundary conditions at the surface of the thrust collar and bull gear, the fluid velocities in the radial and circumferential directions are

$$V_r = \frac{1}{2\mu}\frac{\partial p}{\partial r}\left\{\left(z - z_B\right)\left(z - z_{TC}\right)\right\} + b\omega_B \sin\left(\varepsilon\right)\left\{\frac{\left(z - z_{TC}\right)}{h}\right\} \tag{5}$$

$$V_\theta = \frac{1}{2\mu}\frac{\partial p}{r\partial \theta}\left\{\left(z - z_B\right)\left(z - z_{TC}\right)\right\} + b\omega_B \cos\left(\varepsilon\right)\left\{\frac{\left(z - z_{TC}\right)}{h}\right\} + r\omega_{TC}\left(1 - \frac{z - z_{TC}}{h}\right) \tag{6}$$

Integrating the continuity equation across the film thickness and incorporating the radial and circumferential velocities, a Reynolds equation appears as

$$\begin{aligned} &\frac{1}{r}\frac{\partial}{\partial r}\left(r\frac{h^3}{12\mu}\frac{\partial p}{\partial r}\right) + \frac{1}{r}\frac{\partial}{\partial \theta}\left(\frac{h^3}{12\mu}\frac{\partial p}{r\partial \theta}\right) \\ &= \frac{\partial}{\partial t}h + \frac{1}{r}\frac{\partial}{\partial r}\left\{r\left[b\omega_B \sin\left(\varepsilon\right)\right]\left(\frac{h}{2}\right)\right\} + \frac{1}{r}\frac{\partial}{\partial \theta}\left\{\left[b\omega_B \cos\left(\varepsilon\right) + r\omega_{TC}\right]\left(\frac{h}{2}\right)\right\} \end{aligned} \tag{7}$$

Thrust collars are hydrodynamic, mechanical elements such that the pressure at the boundary of the lubricated zone equals ambient pressure,

$$p_{\Gamma_B} \to p_a \ , \ \Gamma_B = \left\{\theta_{\min} \le \theta \le \theta_{\max}, r = r_{left_{(\theta)}} \ \cup \ \theta_{\min} \le \theta \le \theta_{\max}, r = R_1 \right. \tag{8}$$

Thermal Energy Transport Equation

Ref. [14] states that the complete thermal energy transport equation in cylindrical coordinates for the laminar flow of an incompressible fluid is

$$\rho c_P\left[\frac{\partial T}{\partial t}+V_r\frac{\partial T}{\partial r}r+\frac{V_\theta}{r}\frac{\partial T}{\partial \theta}+V_z\frac{\partial T}{\partial z}\right]=\bar{k}\left[\frac{1}{r}\frac{\partial}{\partial r}\left(r\frac{\partial T}{\partial r}\right)+\frac{1}{r^2}\frac{\partial^2 T}{\partial \theta^2}+\frac{\partial^2 T}{\partial z^2}\right]$$
$$+2\mu\left[\left(\frac{\partial V_r}{\partial r}\right)^2+\left(\frac{1}{r}\left\{\frac{\partial V_\theta}{\partial \theta}+V_r\right\}\right)^2+\left(\frac{\partial V_z}{\partial z}\right)^2\right] \quad (9)$$
$$+\mu\left[\left(\frac{\partial V_\theta}{\partial z}+\frac{1}{r}\frac{\partial V_z}{\partial \theta}\right)^2+\left(\frac{\partial V_z}{\partial r}+\frac{\partial V_r}{\partial z}\right)^2+\left(\frac{1}{r}\frac{\partial V_r}{\partial \theta}+r\frac{\partial}{\partial r}\left\{\frac{V_\theta}{r}\right\}\right)^2\right]$$

where $\bar{\kappa}$ is the thermal conductivity of the lubricant, c_p is the lubricant specific heat at constant pressure, and ρ is the lubricant density.

An order of magnitude analysis for thin film flows shows that only velocity gradients and temperature gradients across the thin film are important [14]. Simplifying Eq. (9) to keep the axial shear stresses and axial temperature gradients, a thermal energy transport equation for a lubricated thrust collar is

$$\rho c_P\left[\frac{\partial T}{\partial t}+V_r\frac{\partial T}{\partial r}r+\frac{V_\theta}{r}\frac{\partial T}{\partial \theta}+V_z\frac{\partial T}{\partial z}\right]=\frac{\partial}{\partial z}\left(\bar{k}\frac{\partial T}{\partial z}\right)+\mu\left[\left(\frac{\partial V_r}{\partial z}\right)^2+\left(\frac{\partial V_\theta}{\partial z}\right)^2\right] \quad (10)$$

Rewriting the material derivative of the temperature on the left hand side of Eq. (10) in a conservative form yields

$$\rho c_P\left[\frac{\partial T}{\partial t}+\frac{1}{r}\frac{\partial}{\partial r}\left(rV_rT\right)+\frac{1}{r}\frac{\partial}{\partial \theta}\left(V_\theta T\right)+\frac{\partial}{\partial z}\left(V_zT\right)\right]=\frac{\partial}{\partial z}\left(\bar{k}\frac{\partial T}{\partial z}\right)+\mu\left[\left(\frac{\partial V_r}{\partial z}\right)^2+\left(\frac{\partial V_\theta}{\partial z}\right)^2\right] \quad (11)$$

Integrating Eq. (11) across the film thickness and using Leibniz's integration formula, the energy equation becomes

$$\rho c_P \left\{ \left[\frac{\partial}{\partial t}\{Th\} - T_{z_B}\frac{\partial z_B}{\partial t} + T_{z_{TC}}\frac{\partial z_{TC}}{\partial t} \right] + \left[\frac{1}{r}\frac{\partial}{\partial r}\left\{ \int_{z_{TC}}^{z_B} rV_r T dz \right\} - \left(b_{(r,\theta)}\omega_B \sin(\theta) \right) T_{z_B}\frac{\partial z_B}{\partial r} \right] \right.$$
$$+ \left[\frac{\partial}{r\partial\theta}\left\{ \int_{z_{TC}}^{z_B} V_\theta T dz \right\} - \left(b_{(r,\theta)}\omega_B \cos(\varepsilon) \right) T_{z_B}\frac{\partial z_B}{r\partial\theta} \right]$$
$$\left. + \left[T_{z_B}\left(\frac{\partial z_B}{\partial t} + b_{(r,\theta)}\omega_B \sin(\varepsilon)\frac{\partial z_B}{\partial r} + b_{(r,\theta)}\omega_B \cos(\varepsilon)\frac{\partial z_B}{r\partial\theta} \right) - T_{z_{TC}}\left(\frac{\partial z_B}{\partial t} \right) \right] \right\} \tag{12}$$
$$= \left(\bar{k}\frac{\partial T}{\partial z} \right)\Bigg|_{z_{TC}}^{z_B} + \mu \left[\int_{z_{TC}}^{z_B} \left(\frac{\partial V_r}{\partial z} \right)^2 dz + \int_{z_{TC}}^{z_B} \left(\frac{\partial V_\theta}{\partial z} \right)^2 dz \right]$$

In the current analysis, the lubricant temperature is assumed not to vary across the film thickness[1], thus $T_{(x,y,z)} \sim T_{(x,y)}$. The integral terms on the left hand side of Eq. (12) are approximated as the product of the film temperature and the mean lubricant flows (q_r, q_θ), i.e.

$$\int_{z_{TC}}^{z_B} V_r T dz \approx T\left(\int_{z_{TC}}^{z_B} V_r dz \right) \approx T q_r \quad , \quad \int_{z_{TC}}^{z_B} V_\theta T dz \approx T \left(\int_{z_{TC}}^{z_B} V_\theta dz \right) \approx T q_\theta \tag{13}$$

With the approximations in Eq. (13) a thermal energy transport equation for the lubricated thrust collar is

$$\rho c_P \left[\frac{\partial}{\partial t}\{hT\} + \frac{1}{r}\frac{\partial}{\partial r}\{rq_r T\} + \frac{1}{r}\frac{\partial}{\partial\theta}\{q_\theta T\} \right] + \bar{h}_B \left(T - T_B \right) + \bar{h}_{TC} \left(T - T_{TC} \right) = \Phi \tag{14}$$

where $\bar{h}_B$, $\bar{h}_{TC}$ are heat convection coefficients towards the thrust collar and bull gear surfaces[2], T_B, T_{TC} are the temperatures of the bull gear and thrust collar surfaces, T is the lubricant temperature, and Φ is the mechanical energy dissipation function for a

[1]Fluid film temperatures typically vary across the film thickness [14], however, a three-dimensional thermohydrodynamic analysis is out of the scope.

[2] See Appendix B for definitions and derivation of heat convection coefficients $\bar{h}_B$, $\bar{h}_{TC}$.

lubricated thrust collar (discussed in the following section). When the lubricant enters the lubricated zone, the lubricant temperature is equal to the supply temperature $T_{(r,\theta,t)} = T_s$ on Γ_s.

For both the thermal energy transport equation and Reynolds equation, the lubricant viscosity is based on an effective lubricant temperature. The relationship between viscosity and temperature is [15]

$$\mu_{(T)} = \mu_s \, \mathrm{e}^{-\alpha_V \{T - T_s\}} \tag{15}$$

where the subscript *s* denotes "supply", and α_v is a temperature viscosity coefficient. The temperature viscosity coefficient is derived from known lubricant viscosities at two temperatures (T_1, T_2), i.e.,

$$\alpha_V = \frac{\ln\left(\frac{\mu_1}{\mu_2}\right)}{T_2 - T_1} \tag{16}$$

Mechanical Energy Dissipation Function

Mechanical power loss in the lubricated zone arises from lubricant shear and pressure extrusion. The wall shear stresses at the thrust collar and bull gear surfaces are [13]

$$\tau_{\theta z} = \mu \frac{\partial V_\theta}{\partial z} = \frac{1}{2}\frac{\partial p}{r\partial\theta}\{2z - z_B - z_{TC}\} + \frac{\mu}{h}\left(b\omega_B \cos(\varepsilon) - r\,\omega_{TC}\right)$$
$$\tau_{rz} = \mu \frac{\partial V_r}{\partial z} = \frac{1}{2}\frac{\partial p}{\partial r}\{2z - z_B - z_{TC}\} + \frac{\mu}{h}\left(b\omega_B \sin(\varepsilon)\right) \qquad (17)$$
$$\tau_{zz} \approx 0$$

For steady state operation the fluid velocities at the thrust collar surface ($z = z_{TC}$) are

$$V_r = 0 \;\;,\;\; V_\theta = r\,\omega_{TC},\;\; V_z = \frac{Dz_{TC}}{Dt} \rightarrow \mathbf{V_{TC}} = \left(0, r\omega_{TC}, \dot{z}_{TC}\right) \qquad (18)$$

Figure 8 shows a projection of the fluid film area on the thrust collar surface with t_θ denoting a component of the traction vector **t** at the surface.

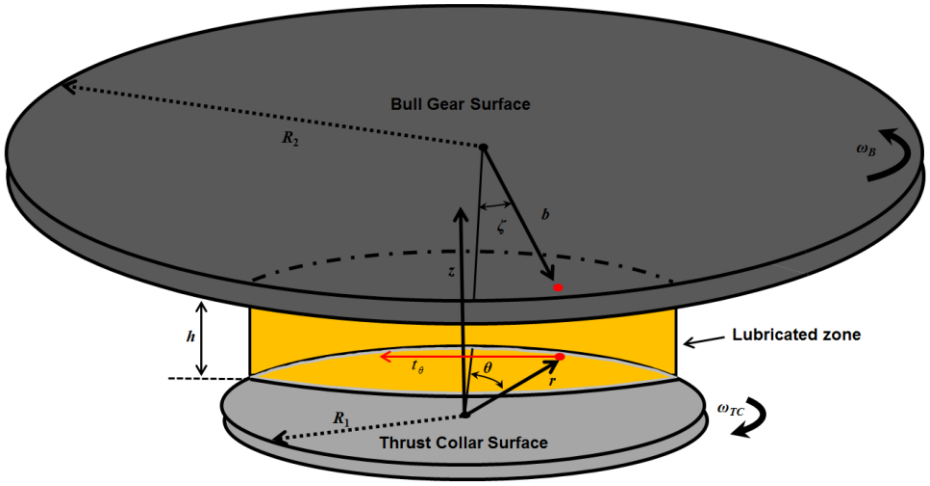

Figure 8. Schematic view of a fluid traction component (t_θ) at the thrust collar surface (taper angles not depicted for simplicity).

The traction **t** at the thrust collar/fluid film interface is the product of the stress tensor **τ** and the normal vector **η** at the surface.

$$\mathbf{t} = \boldsymbol{\tau}\boldsymbol{\eta} = \begin{bmatrix} \tau_{rr} & \tau_{r\theta} & \tau_{rz} \\ \tau_{\theta r} & \tau_{\theta\theta} & \tau_{\theta z} \\ \tau_{zr} & \tau_{z\theta} & \tau_{zz} \end{bmatrix} \begin{bmatrix} \eta_r \\ \eta_\theta \\ \eta_z \end{bmatrix} \tag{19}$$

The traction vector at the thrust collar surface with $\boldsymbol{\eta} = (0,0,1)$, is

$$\mathbf{t_{TC}} = \boldsymbol{\tau}\boldsymbol{\eta} = \begin{bmatrix} \tau_{rr} & \tau_{r\theta} & \tau_{rz} \\ \tau_{\theta r} & \tau_{\theta\theta} & \tau_{\theta z} \\ \tau_{zr} & \tau_{z\theta} & \tau_{zz} \end{bmatrix} \begin{bmatrix} 0 \\ 0 \\ 1 \end{bmatrix} = \begin{bmatrix} \tau_{rz} \\ \tau_{\theta z} \\ \tau_{zz} \end{bmatrix} \tag{20}$$

The mechanical energy dissipation function is the product of the velocity vector and the traction vector[3],

$$\Phi \sim \mathbf{t} \cdot \mathbf{V} = \left(\tau_{rz} V_r + \tau_{\theta z} V_\theta\right) \tag{21}$$

Inserting Eqs. (17) and (18) into Eq. (21), the energy dissipation at the thrust collar surface is

$$\Phi_{TC} = \frac{r\omega_{TC} h}{2} \frac{\partial p}{r\partial\theta} + \frac{\mu}{h}\left[\left(r\omega_{TC}\right)^2 - b\omega_B \cos(\varepsilon) r\omega_{TC}\right] \tag{22}$$

At the bull gear surface ($z = z_B$), the procedure is the same; however, the unit normal vector is $\boldsymbol{\eta} = (0,0,-1)$ and the velocity vector is $\mathbf{V_B} = \left(b\omega_B \sin(\varepsilon), b\omega_B \cos(\varepsilon), \dot{z}_B\right)$. The energy dissipation function at the bull gear surface is

$$\Phi_B = \frac{b\omega_B h}{2}\left[\sin(\varepsilon)\frac{\partial p}{\partial r} + \cos(\varepsilon)\frac{\partial p}{r\partial\theta}\right] + \frac{\mu}{h}\left[\left\{b\omega_B\right\}^2 - b\omega_B \cos(\varepsilon) r\,\omega_{TC}\right] \tag{23}$$

The mechanical energy dissipation function for a lubricated thrust collar combines both losses at the thrust collar surface and at the bull gear surface, i.e.,

---

[3] The contribution of the product $\left(\tau_{zz} V_z\right)$ is second order and may be neglected.

$$\Phi = \Phi_B + \Phi_{TC} = \frac{h}{2}\left[\left\{b\omega_B \sin(\varepsilon)\right\}\frac{\partial p}{\partial r} + \left\{r\omega_{TC} + b\omega_B \cos(\varepsilon)\right\}\frac{\partial p}{r\partial\theta}\right] + \frac{\mu}{h}\left[\left\{b\omega_B\right\}^2 - 2\left(b\omega_B \cos(\varepsilon) r\,\omega_{TC}\right) + \left\{r\omega_{TC}\right\}^2\right] \quad (24)$$

The integral of the mechanical energy dissipation function over the lubricated area between the TC taper and BG taper renders the mechanical power loss in the lubricated zone ($\wp = \iint \Phi dA$) .

Axial Force and Moments on the Thrust Collar Surface

Figure 9 [a] shows a diagram indicating the direction of the applied thrust load (*W*) on the thrust collar in the *y*-*z* plane, as well as the fluid film reaction forces on the thrust collar and bull gear surfaces ($F_{TC,z}$, $F_{B,z}$) . Similarly, Figure 9 [b] depicts a schematic representation of the hydrodynamic pressure field (*P*) acting on the TC surface. As shown in Figure 9 [a], the pressure field (*P*) exerts an axial force (F_z) on the TC and BG surfaces, as well as moments (M_x, M_y) about the TC and BG centers.

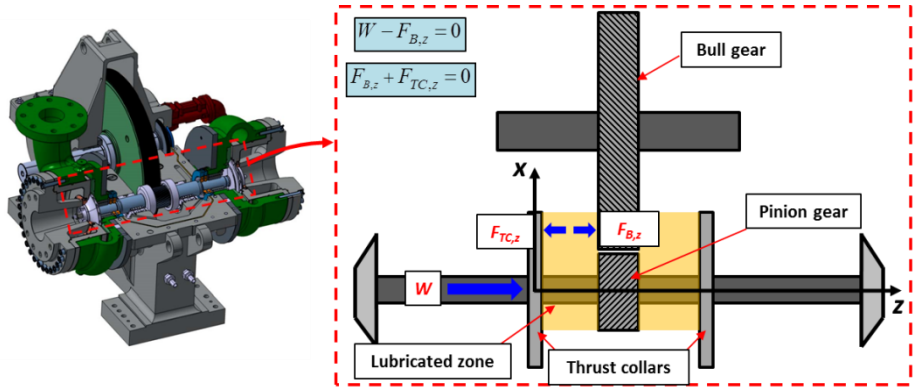

[a]

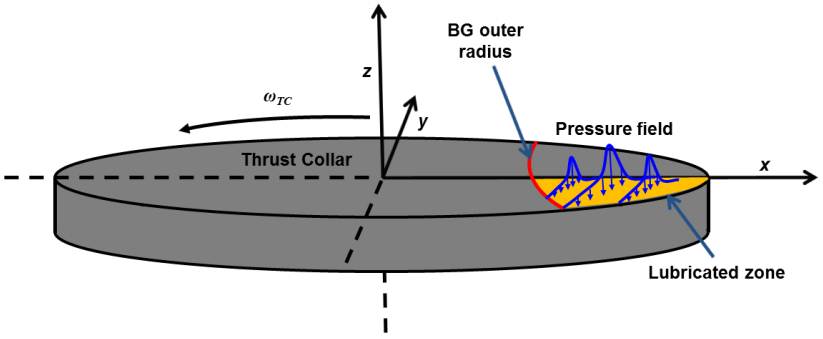

[b]

Figure 9. Schematic representation of [a] imposed axial force on the thrust collar in the *y-z* plane and [b] a hydrodynamic pressure field (*P*) acting on the thrust collar surface.

The pressure difference vector acting on the thrust collar surface is $\mathbf{P}_{\mathbf{TC}} = -(p - p_a)\mathbf{K}$ and the position vector for a point in the lubricated zone is $\mathbf{r} = r\left[\cos(\theta)\mathbf{I} + \sin(\theta)\mathbf{J}\right]$. Integration of the pressure difference over the lubricated area gives the axial force acting on the TC surface.

$$-F_{TC,z} = \int_{-\theta_{\max}}^{\theta_{\max}} \int_{r_{left}}^{R_1} \left(p - p_a\right) r dr d\theta \tag{25}$$

The pressure difference field on the TC surface generates moments about the TC center,

$$\mathbf{M_{TC}} = \int_{-\theta_{\max}}^{\theta_{\max}} \int_{r_{left}}^{R_1} \left(\mathbf{r} \times \mathbf{P}_{TC}\right) r dr d\theta = M_{TC,x}\mathbf{I} + M_{TC,y}\mathbf{J} \tag{26}$$

The *x* and *y* components are

$$\begin{aligned} M_{TC,x} &= -\int_{-\theta_{\max}}^{\theta_{\max}} \int_{r_{left}}^{R_1} \left[\sin\theta \ \left(p - p_a\right) \ r\right] r dr d\theta \\ M_{TC,y} &= \int_{-\theta_{\max}}^{\theta_{\max}} \int_{r_{left}}^{R_1} \left[\cos\theta \ \left(p - p_a\right) \ r\right] r dr d\theta \end{aligned} \tag{27}$$

The pressure difference field on the bull gear surface is $\mathbf{P_B} = \left(p - p_a\right)\mathbf{K} = -\mathbf{P_{TC}}$. The position vector from the bull gear center is $\mathbf{b} = b_{(r,\theta)}\left[-\cos\left(\zeta\right)\mathbf{I} + \sin\left(\zeta\right)\mathbf{J}\right]$. The pressure difference acting on the bull gear surface also produces a moment about the bull gear center,

$$\mathbf{M_B} = \int_{-\theta_{\max}}^{\theta_{\max}} \int_{r_{left}}^{R_1} \left(\mathbf{b} \times \mathbf{P}_B\right) r dr d\theta = M_{B,x}\mathbf{I} + M_{B,y}\mathbf{J} \tag{28}$$

In addition, note that

$$M_{B,x} = M_{TC,x} \tag{29}$$

The moment acting on the BG surface ($M_{B,y}$) can be expressed in terms of the axial force (F_z) and the *y* component of the moment acting on the TC surface ($M_{TC,y}$), i.e.,

$$M_{B_y} = \int_{-\theta_{\max}}^{\theta_{\max}} \int_{r_{left}}^{R_1} -\left\{b\cos(\zeta)(p-p_a)\right\} r dr d\theta = M_{TC,y} - d\ F_z \tag{30}$$

Recall that *d* is the fixed distance between the TC and BG centers.

Thrust Collar Stiffness and Damping Coefficients

In polar coordinates (r,θ) the operators for the gradient of a scalar (w) and divergence of a vector $\vec{\mathrm{v}}$ are,

$$\vec{\nabla}(w) = \frac{\partial}{\partial r}(w)\vec{e}_r + \frac{\partial}{r\partial\theta}(w)\vec{e}_\theta \tag{31}$$

$$\vec{\nabla}\cdot\vec{\mathrm{v}} = \frac{1}{r}\frac{\partial}{\partial r}(r v_r) + \frac{\partial}{r\partial\theta}(v_\theta) \tag{32}$$

With these definitions, Reynolds equation (Eq. (7)) is rewritten as

$$\frac{\partial h}{\partial t} + \vec{\nabla}\cdot\left(-\frac{h^3}{12\mu}\vec{\nabla}p + \vec{s}\frac{h}{2}\right) = 0 = \frac{\partial h}{\partial t} + \vec{\nabla}\cdot\vec{q} \tag{33}$$

where $\vec{q} = -\frac{h^3}{12\mu}\vec{\nabla}p + \vec{s}\frac{h}{2}$ is a vector of flow rates (per unit length), and

$$\vec{s} = \left\{b\omega_B \sin(\varepsilon)\right\}\vec{e}_r + \left\{b\omega_B\cos(\varepsilon) + r\omega_{TC}\right\}\vec{e}_\theta \tag{34}$$

is a vector containing the surface speeds of the trust collar and bull gear.

Superimposed on the static equilibrium position, consider dynamic angular displacements $(\Delta\alpha_x, \Delta\alpha_y)e^{i\omega t}$ for the thrust collar, and $(\Delta\beta_X, \Delta\beta_y)e^{i\omega t}$ for the bull gear,

as well as an axial displacement ($\Delta z\, e^{i\omega t}$), with ω as an arbitrary excitation frequency[4] [16]. The tilts of the thrust collar (TC) and bull gear (BG) are thus

$$\begin{aligned} \alpha_x &= \alpha_{x_0} + \Delta\alpha_x\, e^{i\omega t} \;\;,\;\; \alpha_y = \alpha_{y_0} + \Delta\alpha_y\, e^{i\omega t} \\ \beta_x &= \beta_{x_0} + \Delta\beta_x\, e^{i\omega t} \;\;,\;\; \beta_y = \beta_{y_0} + \Delta\beta_y\, e^{i\omega t} \end{aligned} \tag{35}$$

Substitute Eqs. (35) into the film thickness equation (Eq. (2)) to obtain[5]

$$h_{(r,\theta,t)} = h_0 + \left(\sum \eta_\kappa \Delta\kappa\right) e^{i\omega t} \tag{36}$$

where the sub-index 0 above denotes an equilibrium (or zeroth order condition). The zeroth order film thickness in Eq. (36) equals to

$$\begin{aligned} h_0 = h_{(r,\theta)} = h_{R_{1_0}} &+ \left(R_1 - d + b\right)\varphi_B - \left(R_1 - r\right)\varphi_{TC} + r\cos\theta\left\{\alpha_{y_0} - \beta_{y_0}\right\} \\ &+ d\;\beta_{y_0} + r\sin\theta\left\{\beta_{x_0} - \alpha_{x_0}\right\} \end{aligned} \tag{37}$$

In Eq. (37), $\Delta\kappa = \begin{bmatrix} \Delta z & \Delta\alpha_x & \Delta\beta_x & \Delta\alpha_y & \Delta\beta_y \end{bmatrix}$ denotes the direction of a small amplitude displacement (axial or angular); and

$$\eta_\kappa = \begin{bmatrix} 1 & -r\sin(\theta) & r\sin(\theta) & r\cos(\theta) & d - r\cos(\theta) \end{bmatrix} \tag{38}$$

is a set of geometric functions related to each displacement.

The perturbations in film thickness also cause perturbations in the hydrodynamic pressure; hereby written as

$$p = p_0 + \left(\sum p_\kappa \Delta\kappa\right) e^{i\omega t} \tag{39}$$

---

[4]Note that each perturbation could be associated to a separate or unique frequency; however, for simplicity the perturbations are assumed to have the same arbitrary frequency ω.

[5] In Eq. (36), $\sum \eta_\kappa \Delta\kappa = 1\Delta z + r\sin(\theta)\left[\Delta\beta_x - \Delta\alpha_x\right] + r\cos(\theta)\left[\Delta\alpha_y - \Delta\beta_y\right] + d\,\Delta\beta_y$

where $p_\kappa = \begin{bmatrix} p_z & p_{\alpha_x} & p_{\beta_x} & p_{\alpha_y} & p_{\beta_y} \end{bmatrix}$. Above, p_0 is also known as the zeroth-order or steady state film pressure field.

Substitution of Eqs. (36) and (39) into the Reynolds Eq. (33) gives the zeroth order equation for the equilibrium pressure field p_0,

$$\vec{\nabla} \cdot \left[\frac{h_0^3}{12\mu} \vec{\nabla} p_0 \right] = \tfrac{1}{2} \vec{\nabla} \cdot \left(\vec{s}\, h_0 \right) \tag{40}$$

and the first order (linear) equations

$$\vec{\nabla} \cdot \left[\frac{h_0^3}{12\mu} \vec{\nabla} p_\kappa \right] = i\,\omega\,\eta_\kappa + \vec{\nabla} \cdot \left(\vec{s}\,\frac{\eta_\kappa}{2} - \frac{3h_0^2\,\eta_\kappa}{12\mu} \vec{\nabla} p_0 \right); \quad \kappa = \begin{bmatrix} z & \alpha_x & \beta_x & \alpha_y & \beta_y \end{bmatrix} \tag{41}$$

The pressure field is specified as ambient (p_a) at the boundary of the lubricated zone; hence

$$p_0 = p_a \,;\, p_\kappa = 0 \text{ at } \left\{ \theta_{\min} \le \theta \le \theta_{\max}, r = r_{left}, R_1 \right\} \tag{42}$$

Note that

$$p_{\beta_x} = - p_{\alpha_x} ;\; p_{\beta_y} = d\; p_z - p_{\alpha_y} \tag{43}$$

Inserting the definition of the hydrodynamic pressure field (Eq. 39) into the axial force and moment equations (Eqs. 25, 27 & 30) renders the equations for the zeroth and first order forces and moments, i.e.

$$-F_{TC,z} = \int_{-\theta_{\max}}^{\theta_{\max}} \int_{r_{left}}^{R_1} (p - p_a) r dr d\theta = F_{B,z}$$

$$M_{TC,x} = \int_{-\theta_{\max}}^{\theta_{\max}} \int_{r_{left}}^{R_1} \left[-\sin\theta \ (p - p_a) \ r \right] r \, dr \, d\theta = \int_{-\theta_{\max}}^{\theta_{\max}} \int_{r_{left}}^{R_1} \eta_{\alpha_X} \ (p - p_a) r \, dr \, d\theta = -M_{B,x}$$

$$M_{TC,y} = \int_{-\theta_{\max}}^{\theta_{\max}} \int_{r_{left}}^{R_1} \left[\ \cos\theta \ (p - p_a) \ r \right] r \, dr \, d\theta = \int_{-\theta_{\max}}^{\theta_{\max}} \int_{r_{left}}^{R_1} \eta_{\alpha_Y} (p - p_a) \ r \, dr \, d\theta = d \ F_{TC,z} - M_{B,y}$$

(44)

Since $\eta_z = 1, \ \eta_{\alpha_Y} = r\cos(\theta), \ \eta_{\alpha_X} = -r\sin(\theta)$; Eq. (44) is written as

$$\begin{bmatrix} -F_{TC,z} \\ M_{TC,x} \\ M_{TC,y} \end{bmatrix} = \int_{-\theta_{\max}}^{\theta_{\max}} \int_{r_{left}}^{R_1} \begin{bmatrix} \eta_z \\ \eta_{\alpha_X} \\ \eta_{\alpha_Y} \end{bmatrix} (p - p_a) r \, dr \, d\theta \qquad (45)$$

Substitution of Eq. (39) into Eqs. (45) gives

$$\begin{bmatrix} -F_{TC,z} \\ M_{TC,x} \\ M_{TC,y} \end{bmatrix} = \int_{-\theta_{\max}}^{\theta_{\max}} \int_{r_{left}}^{R_1} \begin{bmatrix} \eta_z \\ \eta_{\alpha_X} \\ \eta_{\alpha_Y} \end{bmatrix} \left(p_0 - p_a + \left[p_z \Delta z + p_{\alpha_x} \Delta\alpha_x + p_{\beta_x} \Delta\beta_x + p_{\alpha_y} \Delta\alpha_y + p_{\beta_y} \Delta\beta_y \right] e^{i\omega t} \right) r \, dr \, d\theta$$

(46)

or

$$\begin{bmatrix} -F_{TC,z} \\ M_{TC,x} \\ M_{TC,y} \end{bmatrix} = \begin{bmatrix} -F_{TC,z_0} \\ M_{TC,x_0} \\ M_{TC,y_0} \end{bmatrix} + \left\{ \int_{-\theta_{\max}}^{\theta_{\max}} \int_{r_{left}}^{R_1} \begin{bmatrix} \eta_z \\ \eta_{\alpha_X} \\ \eta_{\alpha_Y} \end{bmatrix} \left[p_z \Delta z + p_{\alpha_x} \Delta\alpha_x + p_{\beta_x} \Delta\beta_x + p_{\alpha_y} \Delta\alpha_y + p_{\beta_y} \Delta\beta_y \right] r dr d\theta \right\} e^{i\omega t}$$

(47)

From this Eqn., the zeroth order or equilibrium axial force and moments on the thrust collar are

$$\begin{bmatrix} -F_{TC,z_0} \\ M_{TC,x_0} \\ M_{TC,y_0} \end{bmatrix} = \int_{-\theta_{\max}}^{\theta_{\max}} \int_{r_{left}}^{R_1} \begin{bmatrix} \eta_z \\ \eta_{\alpha_X} \\ \eta_{\alpha_Y} \end{bmatrix} (p_0 - p_a) r \, dr \, d\theta \tag{48}$$

An expansion of the right hand side of Eq. (47) gives

$$\begin{bmatrix} -F_{TC,z} \\ M_{TC,x} \\ M_{TC,y} \end{bmatrix} = \begin{bmatrix} -F_{TC,z_0} \\ M_{TC,x_0} \\ M_{TC,y_0} \end{bmatrix} - \begin{bmatrix} H_{zz} & H_{z\alpha_x} & H_{z\beta_x} & H_{z\alpha_y} & H_{z\beta_y} \\ H_{\alpha_x z} & H_{\alpha_x\alpha_x} & H_{\alpha_x\beta_x} & H_{\alpha_x\alpha_y} & H_{\alpha_x\beta_y} \\ H_{\alpha_y z} & H_{\alpha_y\alpha_x} & H_{\alpha_y\beta_x} & H_{\alpha_y\alpha_y} & H_{\alpha_y\beta_y} \end{bmatrix} \begin{Bmatrix} \Delta z \\ \Delta\alpha_x \\ \Delta\beta_x \\ \Delta\alpha_y \\ \Delta\beta_y \end{Bmatrix} e^{i\omega t}$$

(49)

where the *H*'s are known as complex dynamic stiffnesses, whose real and imaginary parts make up the fluid film stiffness and damping coefficients ($H = K + i\omega C$), respectively. From Eqs. (47) and (49) one easily infers

$$\begin{bmatrix} H_{zz} & H_{z\alpha_x} & H_{z\beta_x} & H_{z\alpha_y} & H_{z\beta_y} \\ H_{\alpha_x z} & H_{\alpha_x\alpha_x} & H_{\alpha_x\beta_x} & H_{\alpha_x\alpha_y} & H_{\alpha_x\beta_y} \\ H_{\alpha_y z} & H_{\alpha_y\alpha_x} & H_{\alpha_y\beta_x} & H_{\alpha_y\alpha_y} & H_{\alpha_y\beta_y} \end{bmatrix} = -\int_{-\theta_{\max}}^{\theta_{\max}} \int_{r_{left}}^{R_1} \begin{bmatrix} \eta_z \\ \eta_{\alpha_X} \\ \eta_{\alpha_Y} \end{bmatrix} \begin{bmatrix} p_z & p_{\alpha_x} & p_{\beta_x} & p_{\alpha_y} & p_{\beta_y} \end{bmatrix} r \, dr \, d\theta$$

(50)

And because $p_{\beta_x} = -p_{\alpha_x}$; $p_{\beta_y} = d\, p_z - p_{\alpha_y}$, Eq. (49) reduces to

$$\begin{bmatrix} -F_{TC,z} \\ M_{TC,x} \\ M_{TC,y} \end{bmatrix} = \begin{bmatrix} -F_{TC,z_0} \\ M_{TC,x_0} \\ M_{TC,y_0} \end{bmatrix} - \begin{bmatrix} H_{zz} & H_{z\alpha_x} & H_{z\alpha_y} \\ H_{\alpha_x z} & H_{\alpha_x\alpha_x} & H_{\alpha_x\alpha_y} \\ H_{\alpha_y z} & H_{\alpha_y\alpha_x} & H_{\alpha_y\alpha_y} \end{bmatrix} \begin{Bmatrix} \Delta z \\ \Delta\alpha_x - \Delta\beta_x \\ \Delta\alpha_y - \Delta\beta_y \end{Bmatrix} e^{i\omega t} - d \begin{bmatrix} H_{zz} \\ H_{\alpha_x z} \\ H_{\alpha_y z} \end{bmatrix} \Delta\beta_y e^{i\omega t}$$

(51)

Similarly, the equation for a BG is (refer to Eq. (44))

$$\begin{bmatrix} F_{B,z} \\ M_{B,x} \\ M_{B,y} \end{bmatrix} = \begin{bmatrix} -F_{TC,z} \\ -M_{TC,x} \\ dF_{TC,z} - M_{TC,y} \end{bmatrix} = \begin{bmatrix} -F_{TC,z_0} \\ -M_{TC,x_0} \\ dF_{TC,z_0} - M_{TC,y_0} \end{bmatrix} - \begin{bmatrix} H_{zz} & H_{z\alpha_x} & H_{z\alpha_y} \\ H_{\alpha_x z} & H_{\alpha_x\alpha_x} & H_{\alpha_x\alpha_y} \\ H_{\alpha_y z} & H_{\alpha_y\alpha_x} & H_{\alpha_y\alpha_y} \end{bmatrix} \begin{Bmatrix} \Delta z \\ \Delta\beta_x - \Delta\alpha_x \\ \Delta\beta_y - \Delta\alpha_y \end{Bmatrix} e^{i\omega t}$$

$$+ d \left\{ \begin{bmatrix} -H_{zz} \\ H_{\alpha_x z} \\ H_{\alpha_y z} \end{bmatrix} \Delta\beta_y + \begin{bmatrix} 0 \\ 0 \\ H_{zz} \end{bmatrix} \Delta z \right\} e^{i\omega t}$$

(52)

NUMERICAL FORMULATION[6]

The Finite Element method is selected for solution of the lubricant pressure field (equilibrium plus perturbed), whereas a control volume approach is utilized to approximate the oil temperature in the lubricated zone [17].

Reynolds Equation

Considering the equilibrium and perturbed pressure fields (Eqs. (34 & 36)) the PDEs for the zeroth and first order pressure fields may be written as

$$\vec{\nabla}\cdot\vec{q} = -i\omega\left(\sum \eta_\kappa \Delta\kappa\right)\mathrm{e}^{i\omega t} \tag{53}$$

where $\vec{q}$ represents the additions of the first order and equilibrium flow rates, and the variables κ and η are as previously defined (Eq. (38)). Above, the first order and equilibrium flow rates are

$$\vec{q} = -\frac{h^3}{12\mu}\vec{\nabla}p + \vec{s}\frac{h}{2} = \vec{q}_0 + \left(\sum \vec{q}_\kappa \Delta\kappa\right)\mathrm{e}^{i\omega t}$$

where

$$\vec{q}_0 = -\frac{h_0^3}{12\mu}\vec{\nabla}p_0 + \vec{s}\frac{h_0}{2}; \tag{54}$$

$$\vec{q}_\kappa = -\frac{h_0^3}{12\mu}\vec{\nabla}p_\kappa - \frac{3h_0^2}{12\mu}\eta_k\vec{\nabla}p_0 + \vec{s}\frac{\eta_k}{2}$$

A weak form of Eq. (53) is

$$\iint \Psi_i \left\{\vec{\nabla}\cdot\vec{q} + i\omega\left(\sum \eta_\kappa \Delta\kappa\right)\mathrm{e}^{i\omega t}\right\} d\Omega = 0 \quad \text{for} \quad i, j = 1\ldots N_{pe} \tag{55}$$

---

[6] Refer to Appendix A for details on computer implementation of the numerical formulation presented in this chapter.

where $d\Omega = rdrd\theta$ and Ψ_i are a set of bilinear shape functions. For four nodded elements (N_{pe} = 4), as utilized in the current numerical program, the shape and test function counters (*i*,*j*) run from $i, j = 1 \ldots N_{pe}$. With the properties of the divergence operator[7], Eq. (55) is rewritten as

$$\left(\sum\left\{\iint \vec{\nabla}\cdot\left(\Psi_i \vec{q}_\kappa\right) d\Omega\right\}\Delta\kappa\right)\mathrm{e}^{i\omega t} - \left(\sum\left\{\iint\left(\vec{\nabla}\Psi_i\right)\cdot\vec{q}_\kappa d\Omega\right\}\Delta\kappa\right)\mathrm{e}^{i\omega t} + \iint \vec{\nabla}\cdot\left(\Psi_i\vec{q}_0\right)d\Omega$$
$$-\iint\left(\vec{\nabla}\Psi_i\right)\cdot\vec{q}_0 d\Omega = -i\omega\left(\sum\left\{\iint \eta_\kappa \Psi_i d\Omega\right\}\Delta\kappa\right)\mathrm{e}^{i\omega t} \tag{56}$$

Using the divergence theorem, the first and third terms on the left hand side of Eq. (56) become

$$\left(\sum\left\{\oint\left(\Psi_i \vec{q}_\kappa\right)\cdot\vec{n}dS\right\}\Delta\kappa\right)\mathrm{e}^{i\omega t} - \left(\sum\left\{\iint\left(\vec{\nabla}\Psi_i\right)\cdot\vec{q}_\kappa d\Omega\right\}\Delta\kappa\right)\mathrm{e}^{i\omega t} + \oint\left(\Psi_i\vec{q}_0\right)\cdot\vec{n}dS$$
$$-\iint\left(\vec{\nabla}\Psi_i\right)\cdot\vec{q}_0 d\Omega = -i\omega\left(\sum\left\{\iint \eta_\kappa \Psi_i d\Omega\right\}\Delta\kappa\right)\mathrm{e}^{i\omega t} \tag{57}$$

In the Galerkin formulation, the pressure fields (zeroth order and first order) equal to linear combinations of nodal values and bilinear shape functions, i.e.,

$$p_0 = \sum_{j=1}^{n_{pe}} \Psi_j \bar{P}_{0j};\ p_\kappa = \sum_{j=1}^{n_{pe}} \Psi_j \bar{P}_{\kappa j} \tag{58}$$

Substituting the definitions in Eq. (58) into Eq. (57), the finite element formulations for the zeroth and first order pressure fields are [17]

---

[7] $a\left(\vec{\nabla}\cdot\vec{b}\right) = \vec{\nabla}\cdot\left(a\ \vec{b}\right) - \left(\vec{\nabla}a\right)\cdot\vec{b}$, where *a* is a scalar function and $\vec{b}$ is a vector.

$$k_{ij}^{e}\bar{P}_{0j}^{e} = -q_{0i}^{e} + f_{0i}^{e}$$
$$k_{ij}^{e}\bar{P}_{\kappa_j} = -q_{\kappa_i} + f_{\kappa_i} - S_{ij}^{\kappa}\bar{P}_{0j}^{e} \tag{59}$$

where the coefficients of the fluidity matrices are

$$k_{ij}^{e} = \iint \left(\frac{h_0^3}{12\mu}\right)\left\{\frac{\partial\Psi_i}{\partial r}\frac{\partial\Psi_j}{\partial r} + \frac{\partial\Psi_i}{r\partial\theta}\frac{\partial\Psi_j}{r\partial\theta}\right\}d\Omega$$
$${}^{e}S_{ij}^{\kappa} = \iint \eta_{\kappa}\left(\frac{h_0^2}{4\mu}\right)\left\{\frac{\partial\Psi_i}{\partial r}\frac{\partial\Psi_j}{\partial r} + \frac{\partial\Psi_i}{r\partial\theta}\frac{\partial\Psi_j}{r\partial\theta}\right\}d\Omega \tag{60}$$

and the vectors denoting the effects of shear flow are

$$f_{0_i}^{e} = \frac{1}{2}\iint h_0\left(\frac{\partial\Psi_i}{\partial r}[s_r] + \frac{\partial\Psi_i}{r\partial\theta}[s_\theta]\right)d\Omega$$
$$f_{\kappa_i} = -i\omega\iint(\eta_{\kappa}\Psi_i)\,d\Omega + \frac{1}{2}\iint \eta_{\kappa}\left(\frac{\partial\Psi_i}{\partial r}[s_r] + \frac{\partial\Psi_i}{r\partial\theta}[s_\theta]\right)d\Omega \tag{61}$$

where, again, where $d\Omega = rdrd\theta$ and $\vec{s} = \{b\omega_B\sin(\varepsilon)\}\vec{e}_r + \{b\omega_B\cos(\varepsilon) + r\omega_{TC}\}\vec{e}_\theta$. The flows through the boundaries of the finite elements are

$$q_{0_i}^{e} = \oint \Psi_i\,\vec{q}_0\cdot\vec{n}\,dS; \quad q_{\kappa_i} = \oint \Psi_i\,\vec{q}_{\kappa}\cdot\vec{n}\,dS \tag{62}$$

For computer implementation, 2x2 Gauss-Legendre-Quadrature numerical integration with the appropriate weight functions [17] is utilized to evaluate the integrals in Eqs. (60-61). Once the boundary conditions (Eq. (42)) are enforced, the set of linear algebraic equations in Eq. (59) is solved via a process of backward and forward-substitution [17].

Thermal Energy Transport Equation

A control volume approach is utilized for the solution of the thermal energy transport equation. Figure 10 shows a finite element mesh, consisting of four elements in the horizontal direction and eight elements in the vertical direction (4x8) with 45 total nodes. Figure 10 also highlights a typical row of finite elements used to analyze the fluid flow in the lubricated zone. This row of finite elements is hereby referred to as a control volume (CV).

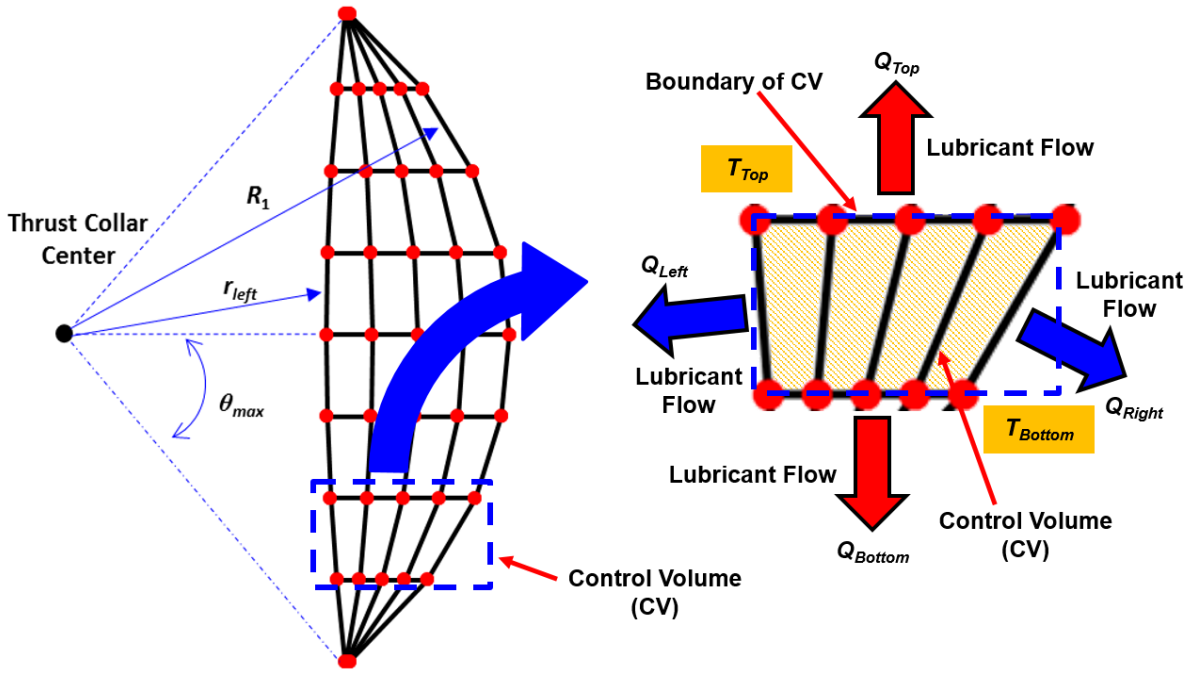

Figure 10. Typical finite element mesh of the lubricated zone and a single control volume comprised of a row of finite elements.

Under steady conditions the conservation of flow in a lubricated thrust collar is

$$\vec{\nabla} \cdot \vec{q} = 0 \tag{63}$$

where $\vec{q}$ is the lubricant flow rate (per unit length). As described above, the divergence theorem shows that the integral of Eq. (63) can be written as

$$\iint_A \left(\vec{\nabla} \cdot \vec{q}\right) dA = \oint_S \left(\vec{q} \cdot \vec{n}\right) dS = 0 \tag{64}$$

From Eq. (64), at the boundary of the CV (see Fig. 8),

$$\oint_S q_n dS = Q_{Top} + Q_{Bottom} + Q_{Left} + Q_{Right} = 0 \tag{65}$$

Eq. (65) states the balance of flows (leaving) through the boundaries of the control volume. The analysis of the thermal energy transport equation (TETE) herein utilizes rows of finite elements lumped into single control volumes (as shown in Figure 10).

Rewriting Eq. (14) in vector form, a steady state ($\frac{\partial h}{\partial t} = 0$) TETE for a lubricated thrust collar is

$$\rho c_p \vec{\nabla} \cdot \left(\vec{q} T\right) + \bar{h}_B \left(T - T_B\right) + \bar{h}_{TC} \left(T - T_{TC}\right) = \Phi \tag{66}$$

In Cartesian coordinates Eq. (66) is

$$\rho c_p \left[\frac{\partial}{\partial x}\left(q_x T\right) + \frac{\partial}{\partial y}\left(q_y T\right)\right] = \Phi - \bar{h}_B \left(T - T_B\right) - \bar{h}_{TC} \left(T - T_{TC}\right) \tag{67}$$

Integrating Eq. (67) over the CV shown in Figure 10,

$$\rho c_p \oint_S q_n T dS = \iint_A \left(\Phi - \bar{h}_B \left(T - T_B\right) - \bar{h}_{TC} \left(T - T_{TC}\right)\right) dA \tag{68}$$

Recall the CV adds a full row of finite elements. Thus, the right hand side of Eq. (68) sums the contributions from all the elements in a row,

$$\rho c_p \oint_S q_n T dS = \sum_{i=1}^{e_{CV}} \wp_i^e - \sum_{i=1}^{e_{CV}} \left(\left(\bar{h}_B + \bar{h}_{TC} \right) T - \left(\bar{h}_B T_B + \bar{h}_{TC} T_{TC} \right) \right)_i A_i^e \qquad (69)$$

where A_i^e is the area of element *i* and $\wp_i^e$ represents the power dissipated in element *i*. That is,

$$A_i^e = \iint d\Omega_i^e; \quad \wp_i^e = \iint \Phi_i^e d\Omega_i^e \qquad (70)$$

The surface integral on the left hand side (LHS) of Eq. (69) is expressed as the summation of the heat flows through the CV boundaries, i.e.,

$$\begin{aligned} &\rho c_p \left[T_{Top} Q_{Top} + T_{Bottom} Q_{Bottom} + T_{Left} Q_{Left} + T_{Right} Q_{Right} \right] \\ &\approx \sum_{i=1}^{ne_H} \wp_i^e - \sum_{i=1}^{ne_H} \left(\left(\bar{h}_B + \bar{h}_{TC} \right) T - \left(\bar{h}_B T_B + \bar{h}_{TC} T_{TC} \right) \right)_i A_i^e \end{aligned} \qquad (71)$$

When lubricant enters the bottom of the lubricated domain, or enters through the right or left boundaries, the fluid temperature is equal to the lubricant supply temperature ($T_{Left} = T_{Right} = T_{Bottom} = T_s$) and the unknowns become *T* and T_{top}. On the other hand, if the lubricant leaves through either the left or right boundaries, the respective temperature in Eq. (71) is unknown. To handle the multiple unknowns, the oil temperature (*T*) prevailing in the control volume is taken, for simplicity, as an arithmetic average of the temperatures at the top and bottom boundaries, i.e.,

$$T \sim \frac{T_{Bottom} + T_{Top}}{2} \qquad (72)$$

For the case where lubricant enters through the bottom and left faces of the CV (Q_{Bottom}, Q_{Left} <0), and leaves through the top and right faces (Q_{Right}, Q_{Top} >0), Eq. (71) becomes

$$a_T T_{Top} = S_P - b_T T_{Bottom} \tag{73}$$

where

$$a_T = \left[Q_{Top} + \frac{1}{2} Q_{Right} + \frac{\sum_{i=1}^{ne_H} \left(\bar{h}_B + \bar{h}_{TC} \right)_i A_i^e}{2\rho c_p} \right]$$

$$b_T = \left[Q_{Bottom} + \frac{1}{2} Q_{Right} + \frac{\sum_{i=1}^{ne_H} \left(\bar{h}_B + \bar{h}_{TC} \right)_i A_i^e}{2\rho c_p} \right] \tag{74}$$

$$S_P = \frac{\sum_{i=1}^{ne_H} \wp_i^e + \sum_{i=1}^{ne_H} \left(\bar{h}_B T_B + \bar{h}_{TC} T_{TC} \right)_i A_i^e}{\rho c_p} - T_s Q_{Left}$$

PREDICTIONS FOR THE PERFORMANCE OF A STATICALLY ALIGNED THRUST COLLAR

Parameters such as mechanical power loss, lubricant temperature rise, minimum film thickness, lubricant flow rate, peak hydrodynamic pressure, and fluid film stiffness and damping coefficients characterize the performance of a lubricated thrust collar. For a perfectly aligned TC, the taper angles of both the TC and BG, as well as the applied thrust load and shaft speeds have large effects on these performance parameters.

Normalized Parameters

Due to proprietary information restrictions, normalized dimensions, operating conditions and performance parameters are presented as [12]

$$\bar{\omega} = \frac{\omega_{TC}}{\omega_B} \ , \ \bar{r} = \frac{r}{R_1} \ , \ \bar{\varphi}_{TC} = \frac{\varphi_{TC}}{\varphi^*} \ , \ \bar{\varphi}_B = \frac{\varphi_B}{\varphi^*} \tag{75}$$

where φ^* is a typical taper angle for TCs applicable to IGCs. A dimensionless form of the Reynolds equation leads to a thrust collar speed number (Λ_{TC}), from which the characteristic film thickness h^* can be determined. In dimensionless form the Reynolds equation is,

$$\bar{\nabla} \cdot \left(\bar{\bar{\nabla}} \bar{P} \right) = \Lambda_{TC} \left[\frac{1}{\bar{\bar{r}}} \frac{\partial}{\partial \bar{r}} \left\{ \bar{r} \ \bar{b} \ \bar{\omega} \ \bar{h} \sin(\varepsilon) \right\} + \frac{1}{\bar{\bar{r}}} \frac{\partial}{\partial \theta} \left\{ \bar{h} \left[\bar{b} \ \bar{\omega} \cos(\varepsilon) + \bar{r} \right] \right\} \right] \tag{76}$$

where

$$\Lambda_{TC} = \frac{\frac{h^* \omega_{TC}}{2}}{\frac{h^{*3} p^*}{12 \mu R_1^2}} = \frac{6 \mu \omega_{TC} A_{\text{lub}}}{W} \left(\frac{R_1}{h^*} \right)^2 \tag{77}$$

To find a characteristic film thickness of the same order as the film thickness in the lubricated zone, arbitrarily set Λ_{TC}=100 and find h^*.

$$h^* = R_1 \left(\frac{6 \mu \omega_{TC} A_{\text{lub}}}{\Lambda_{TC} W} \right)^{\frac{1}{2}} \tag{78}$$

A normalized thrust load, pressure, film thickness, friction factor, lubricant temperature rise, and lubricant flow rate are defined as [12]

$$\overline{W} = \frac{W}{W^*} \ , \ \overline{P} = \frac{p}{p^*} \ , \ \overline{h} = \frac{h}{h^*} \ , \ f = \frac{\wp}{\omega_{TC} W^* R_1} \ , \ \Delta \overline{T} = \frac{\Delta T}{\Delta T^*} \ , \ \overline{Q} = Q \left(\frac{\omega_{TC}^*}{R_2^3} \right) \tag{79}$$

where $p^* = \left(W^* / A_{\text{lub}} \right)$ is a specific pressure (or load), h^* is a characteristic film thickness, and ω_{TC}^* is a characteristic TC speed.

In addition, normalized force and moment stiffness coefficients are

$$\begin{gathered} \overline{K}_{zz} = K_{zz} \left(\frac{h^*}{W^*} \right) \\ \left(\overline{K}_{\alpha_x \alpha_x}, \overline{K}_{\alpha_y \alpha_y}, \overline{K}_{\alpha_x \alpha_y}, \overline{K}_{\alpha_y \alpha_x} \right) = \left(K_{\alpha_x \alpha_x}, K_{\alpha_y \alpha_y}, K_{\alpha_x \alpha_y}, K_{\alpha_y \alpha_x} \right) \left(\frac{h^*}{W^* R_1^2} \right) \\ \left(\overline{K}_{z \alpha_x}, \overline{K}_{z \alpha_y}, \overline{K}_{\alpha_x z}, \overline{K}_{\alpha_y z} \right) = \left(K_{z \alpha_x}, K_{z \alpha_y}, K_{\alpha_x z}, K_{\alpha_y z} \right) \left(\frac{h^*}{W^* R_1} \right) \end{gathered} \tag{80}$$

In the same manner, normalized damping coefficients for a lubricated thrust collar are

$$\overline{C}_{zz} = C_{zz}\left(\frac{\omega_{TC}^{*} h^{*}}{W^{*}}\right)$$

$$\left(\overline{C}_{\alpha_x\alpha_x}, \overline{C}_{\alpha_y\alpha_y}, \overline{C}_{\alpha_x\alpha_y}, \overline{C}_{\alpha_y\alpha_x}\right) = \left(C_{\alpha_x\alpha_x}, C_{\alpha_y\alpha_y}, C_{\alpha_x\alpha_y}, C_{\alpha_y\alpha_x}\right)\left(\frac{\omega_{TC}^{*} h^{*}}{W^{*} R_1^2}\right) \qquad (81)$$

$$\left(\overline{C}_{z\alpha_x}, \overline{C}_{z\alpha_y}, \overline{C}_{\alpha_x z}, \overline{C}_{\alpha_y z}\right) = \left(C_{z\alpha_x}, C_{z\alpha_y}, C_{\alpha_x z}, C_{\alpha_y z}\right)\left(\frac{\omega_{TC}^{*} h^{*}}{W^{*} R_1}\right)$$

Hydrodynamic Pressure and Film Thickness Profiles

Figure 11 displays two BG/TC pairs with different taper angles. Notice that when $\varphi_B > \varphi_{TC}$ **,** the film thickness at the right edge ($r = R_1$) of the lubricated zone (h_{R_1}) is smaller than the film thickness at the left boundary ($r = r_{left}$) of the lubricated zone ($h_{r_{left}}$). However, when $\varphi_{TC} > \varphi_B$, the film thickness at the thrust collar radius (h_{R_1}) is lesser than $h_{r_{left}}$, the film thickness at the left boundary ($r = r_{left}$) or the location of the bull gear outer radius.

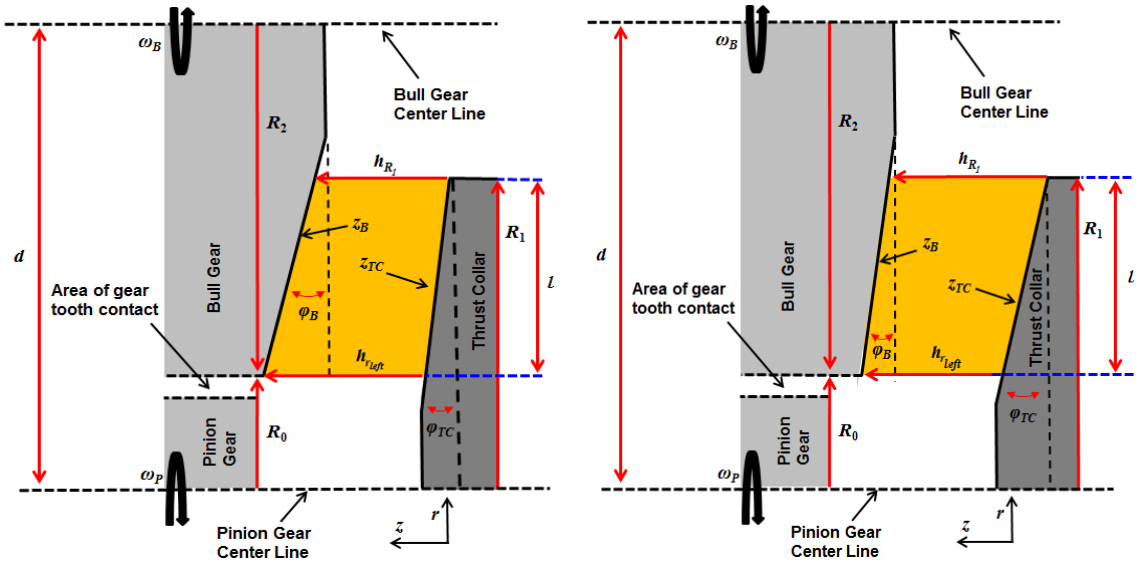

Figure 11. Schematic side views of thrust collars with different taper angles.

The difference in taper angles, displayed in Figure 11, results in changes to the film thickness profile, and consequently, changes in the hydrodynamic pressure profile between a lubricated TC and BG. Table 1 displays operating conditions and geometric ratios for the BG/TC pair under scrutiny. The lubricant is ISO VG 32. Note the width (l) and area of the lubricated zone are relatively small when compared to the TC radius and area ($A_{\text{lub}} / \pi R_1^2 = 0.12$).

Table 1. Bull gear and thrust collar operating conditions, geometric ratios, and lubricant properties.

Operating Conditions		
Load	$\bar{W}$	1.0
Speed (BG/TC)	$\bar{\omega}$	10
Geometry	R_2/R_1	7.14
	d/R_1	7.78
Lubricant ISO VG 32		
Supply Temperature	T_s	49 °C
Dynamic Viscosity (49°C)	μ	0.0204 Pa.s
Ambient Pressure	p_a	100 kPa
Max. angle	θ_{max}	47.3°
Length	c/R_1	1.47
Width at $\theta = 0$	l/R_1	0.36
Area	$A_{lub}/\pi R_1^2$	0.12

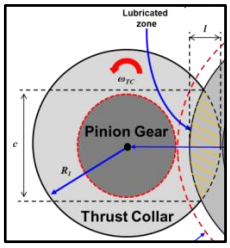

In the following analysis the lubricant viscosity varies with temperature according to Eq. (15). In addition, the TC and BG surfaces are maintained at constant temperatures of $T_{TC} = T_B = 50$°C, and heat transfer into the TC and BG surfaces is accounted for ($\bar{h}_{TC}, \bar{h}_B$ as defined in Appendix B). To analyze changes in film thickness and pressure profiles between different taper angle configurations, three TC/BG taper configurations are analyzed. The first configuration has the bull gear taper equal to the thrust collar taper $(\bar{\varphi}_B/\bar{\varphi}_{TC})$ =1.0; for the second taper configuration the bull gear taper is larger than

the thrust collar taper, $\left(\bar{\varphi}_B/\bar{\varphi}_{TC}\right)$>1; and for the third configuration, $\left(\bar{\varphi}_B/\bar{\varphi}_{TC}\right)$< 1.0. As mentioned previously, some of the following results are reproduced from Ref. [12].

For the first TC taper configuration $\left(\varphi_B/\varphi_{TC}\right)$=1, Figure 12 shows contour plots of the normalized pressure ($\bar{P}$) and film thickness ($\bar{h}$). For the specified thrust load ($\bar{W}$ =0.83), notice that the majority of the film thickness in the lubricated zone is between one to two times the minimum film thickness ($\bar{h}_{\min}$=0.59) and the peak pressure ($\bar{P}_{\max}=5.23$) occurs near the center of the lubricated zone. The ratio of the maximum film thickness to the minimum film thickness in the lubricated zone is $\bar{h}_{\max}/\bar{h}_{\min}$ =5.87**.** Note, the film thickness above the thrust collar center line (θ = 0) diverges to yield lubricant cavitation.

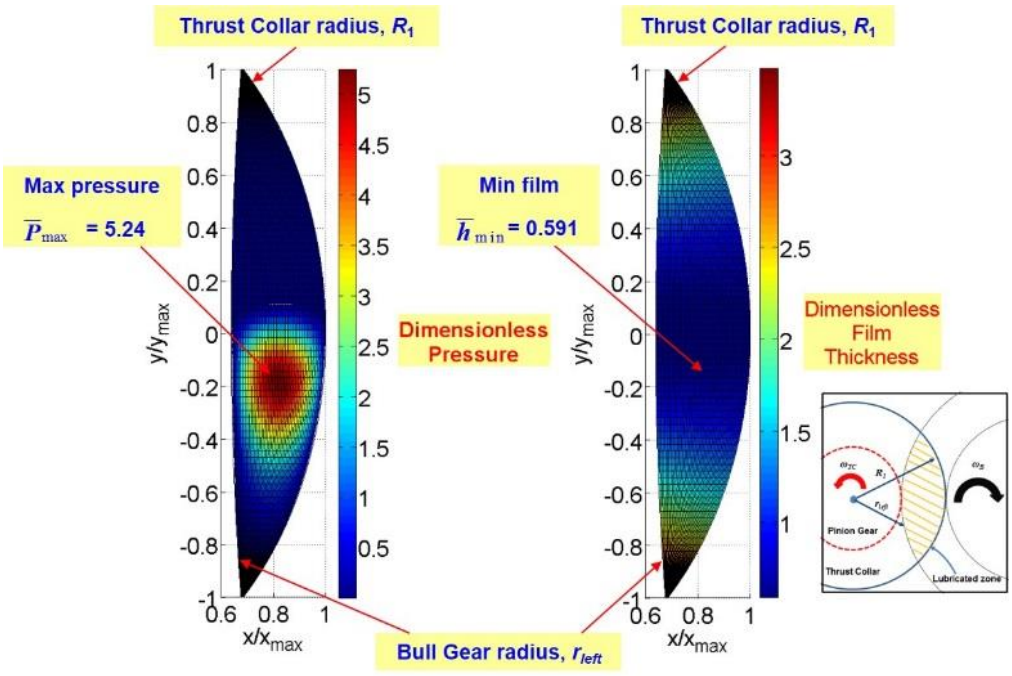

[a] Pressure [b] Film Thickness

Figure 12. Contour plots of [a] hydrodynamic pressure and [b] film thickness in a thrust collar with $(\bar{\varphi}_B/\bar{\varphi}_{TC})=1.0$. $\bar{W}=1, \bar{\omega}=10, R_2/R_1=7.14$ [12].

For the second taper configuration $(\bar{\varphi}_B/\bar{\varphi}_{TC})$=1.2, and the same thrust load, Figure 13 displays dimensionless pressure field and film thickness. Notice that the minimum film thickness shifts to the outer edge of the TC (R_1), also the location of the maximum pressure. Note that for this taper configuration $(\bar{\varphi}_B/\bar{\varphi}_{TC})$=1.2, the minimum film thickness ($\bar{h}_{min}=0.332$) is nearly half the minimum film thickness for the configuration

with $(\bar{\varphi}_B/\bar{\varphi}_{TC})$=1, whereas the peak pressure ($\bar{P}_{\max}=5.63$) is slightly larger. Note $\bar{h}_{\max}/\bar{h}_{\min}$ =9.59, almost twice that of the previous taper configuration.

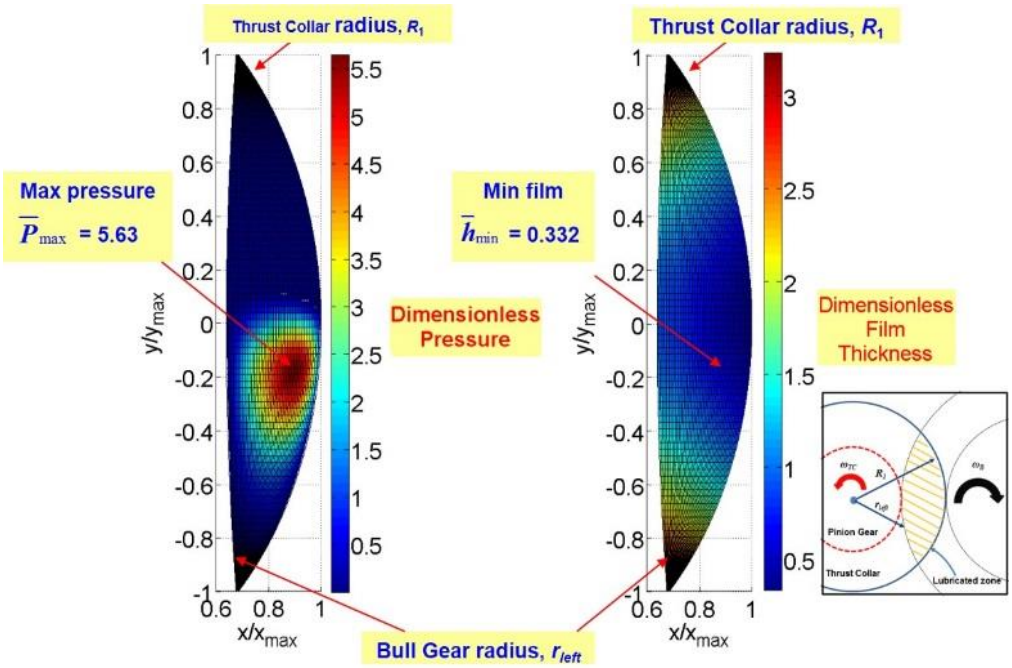

[a] Pressure [b] Film Thickness

Figure 13. Contour plots of [a] hydrodynamic pressure and [b] film thickness in a thrust collar with $(\bar{\varphi}_B/\bar{\varphi}_{TC})$=1.2. $\bar{W}=1, \bar{\omega}=10, R_2/R_1=7.14$ [12].

For the third taper configuration $(\bar{\varphi}_B/\bar{\varphi}_{TC})$=0.8 and the same thrust load, Figure 14 displays the dimensionless pressure field and film thickness. Notice that the minimum film thickness and maximum pressure shift toward the BG radius, r_{left} (left side of the lubricated zone). The peak pressure ($\bar{P}_{\max}=5.81$) is slightly larger and the minimum

film thickness ($\bar{h}_{\min} = 0.309$) is slightly smaller than for the TC taper configuration with $(\bar{\varphi}_B/\bar{\varphi}_{TC})$=1.25. In addition $\bar{h}_{\max}/\bar{h}_{\min}$ =10.31, as large as in the prior configuration, and twice that in the first one, $(\bar{\varphi}_B/\bar{\varphi}_{TC})$=1.0.

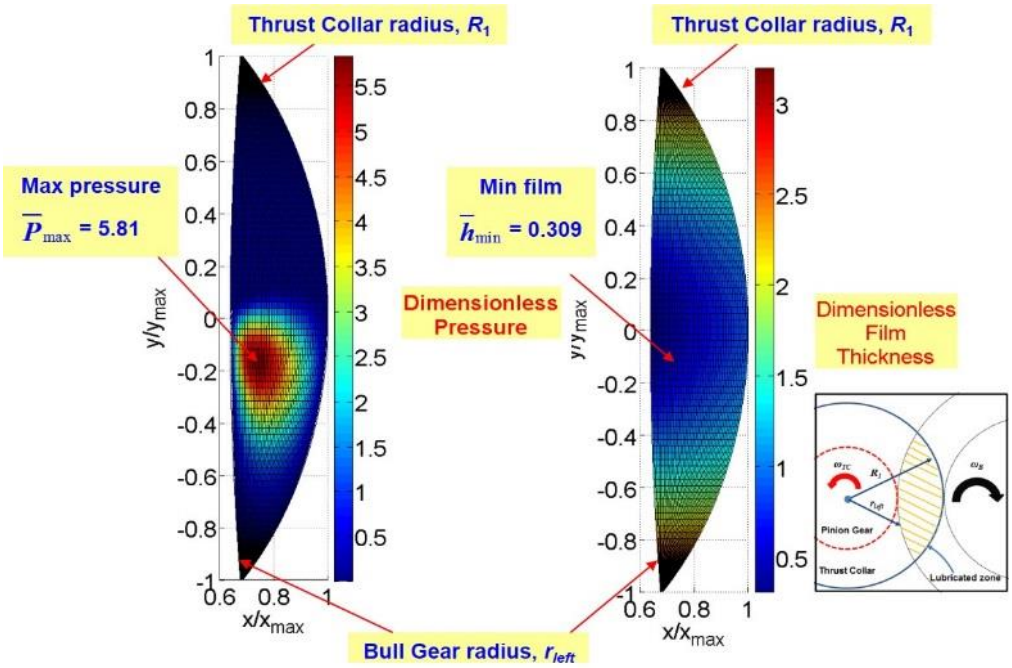

[a] Pressure [b] Film Thickness

Figure 14. Contour plots of [a] hydrodynamic pressure and [b] film thickness in a thrust collar with $(\bar{\varphi}_B/\bar{\varphi}_{TC})$=0.8. $\bar{W}=1, \bar{\omega}=10, R_2/R_1=7.14$ [12].

Effect of Taper Angles on the Performance of a Lubricated Thrust Collar

The sponsor of this work typically utilizes angular tolerances of $\bar{\varphi}_B, \bar{\varphi}_{TC} \pm 0.2$ for the taper angles on the BG and TC surfaces. The following section presents performance parameters for five different taper angle configurations. The first configuration has the bull gear taper angle equal to that of the thrust collar ($\bar{\varphi}_{TC} - \bar{\varphi}_B = 0$). For the second and third taper configurations, the bull gear taper angle is larger than the thrust collar taper angle ($\bar{\varphi}_B - \bar{\varphi}_{TC} = 0.1,\ 0.2$); and for the fourth and fifth configurations ($\bar{\varphi}_{TC} - \bar{\varphi}_B = 0.1,\ 0.2$). By using various taper angle combinations, the analysis aims to reveal a relationship between taper angle and the performance parameters of a lubricated TC. As a secondary goal, the analysis aims to determine if the current angular tolerance of $\bar{\varphi}_B, \bar{\varphi}_{TC} \pm 0.2$ produces TC/BG pairs with similar performance parameters. Note that if both the thrust collar and bull gear are not tapered ($\bar{\varphi}_B = \bar{\varphi}_{TC} = 0$), the lubricated area does not generate a hydrodynamic pressure. Thus, for null taper angle, the hydrodynamic pressure, stiffness and damping coefficients equal zero (not shown in following figures).

Figure 15 displays the normalized minimum film thickness ($\bar{h}_{\min}$) versus normalized TC taper angle for a TC/BG pair with dimensions and operating conditions as in Table 1 and the five taper configurations under investigation. Note that when $\bar{\varphi}_{TC} = \bar{\varphi}_B$ the minimum film thickness in the lubricated zone is the largest. The predictions show that a TC configuration where the TC taper is larger than the BG taper ($\bar{\varphi}_{TC} > \bar{\varphi}_B$) produces a

smaller minimum film thickness. Also, as the difference between the two taper angles increases, the film thickness over the majority of the lubricated zone increases and the minimum film thickness necessary to support the thrust load decreases.

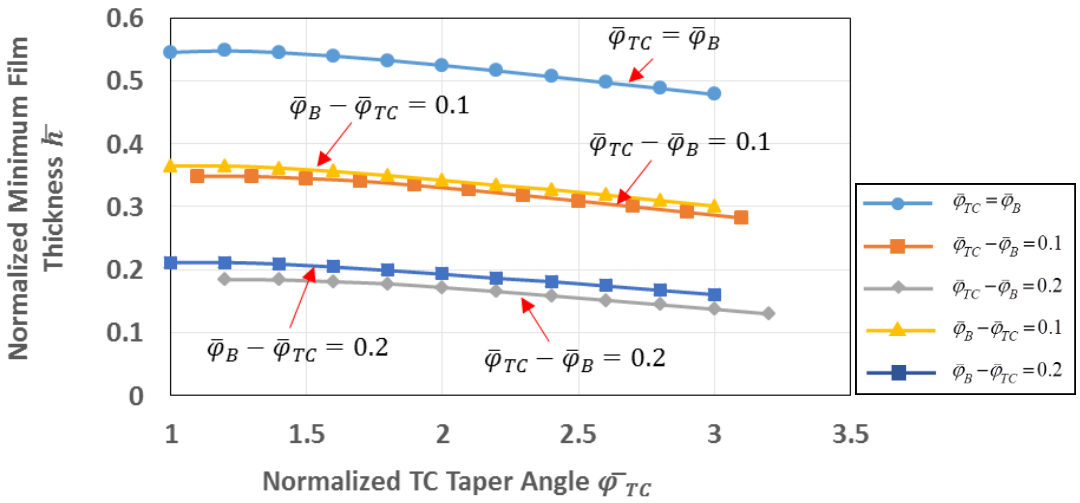

Figure 15. Minimum film thickness ($\bar{h}_{min}$) versus thrust collar taper angle ($\bar{\varphi}_{TC}$) for five taper angle configurations. $\bar{W} = 1, \bar{\omega} = 10, R_2/R_1 = 7.14$.

Figure 16 displays the maximum hydrodynamic pressure ($\bar{P}_{max}$) versus TC taper angle for the same taper configurations. For a slight difference in taper angle between the TC and BG, there is only a slight difference in peak pressures. Notice that the pressure increases almost linearly with thrust collar taper angle, and for a 0.2 difference between the taper angles ($\bar{\varphi}_{TC} - \bar{\varphi}_B = 0.2$), the peak pressure increases at a faster rate with TC taper angle. To support the thrust load as the thrust collar taper angle increases, the minimum film thickness decreases, generating a higher peak pressure near this

location. The minimum film thickness is also directly related to the axial film stiffness, as shown later.

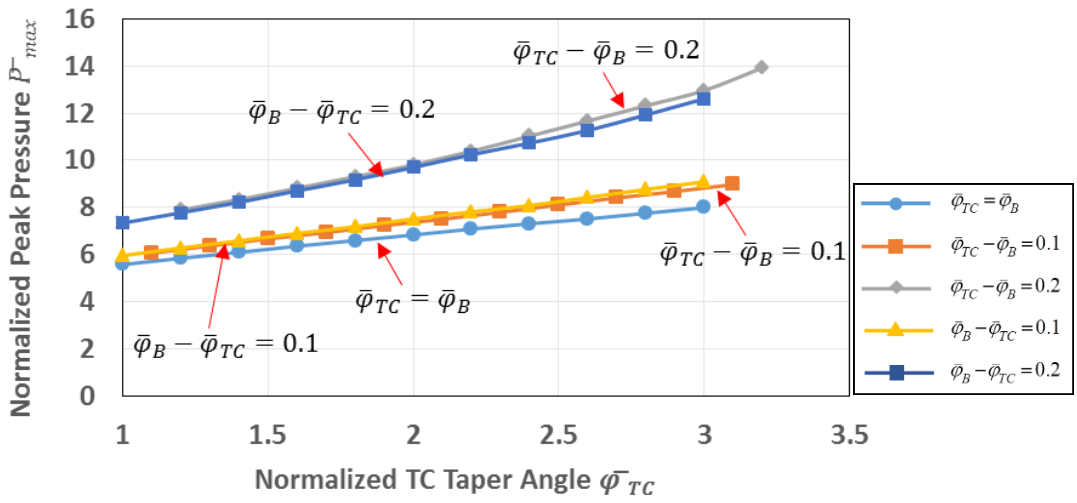

Figure 16. Peak pressure ($\bar{P}_{max}$) versus thrust collar taper angle ($\bar{\varphi}_{TC}$) for five taper angle configurations. $\bar{W} = 1, \bar{\omega} = 10, R_2/R_1 = 7.14$.

Figure 17 shows the friction factor (*f*) versus TC taper angle for several TC and BG pairs. As the taper angle increases the difference in the friction factor becomes more pronounced. Note that the friction factor decreases with increasing TC taper angle, denoting less lubricant shear, and mechanical power loss. As noted above, as the TC and BG taper angles increase, the majority of the film thickness in the lubricated zone increases, leading to the decrease in shear and power loss.

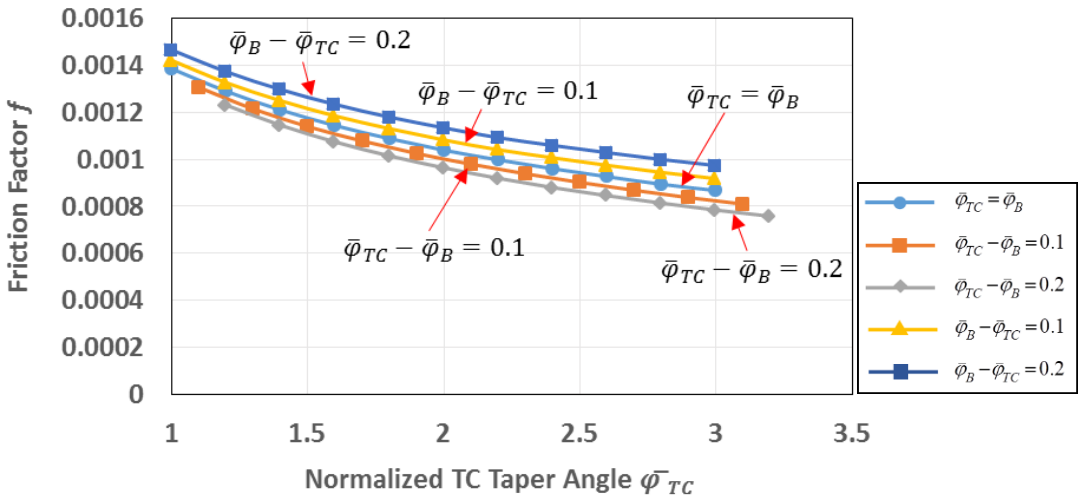

Figure 17. Friction factor (*f*) versus thrust collar taper angle ($\bar{\varphi}_{TC}$) for five taper angle configurations. $\bar{W} = 1, \bar{\omega} = 10, R_2/R_1 = 7.14$.

Figure 18 displays the lubricant flow rate (Q) required to maintain a full fluid film between the TC taper and BG taper. The predictions show that the lubricant flow rate increases linearly with the TC taper angle for all the configurations. The required flow rate for a TC/BG pair with $\bar{\varphi}_B > \bar{\varphi}_{TC}$ is slightly larger than the required flow for the other taper configurations. The difference in flow rates occurs because of the differences in the locations of the minimum film thicknesses and peak pressure. When the TC taper equals the BG taper ($\bar{\varphi}_B = \bar{\varphi}_{TC}$) or the TC taper is larger than the BG taper ($\bar{\varphi}_{TC} > \bar{\varphi}_B$), the peak pressure and large pressure gradients occur closer to the TC center, forcing less fluid out of the lubricated domain when compared to the configuration with $\bar{\varphi}_B > \bar{\varphi}_{TC}$.

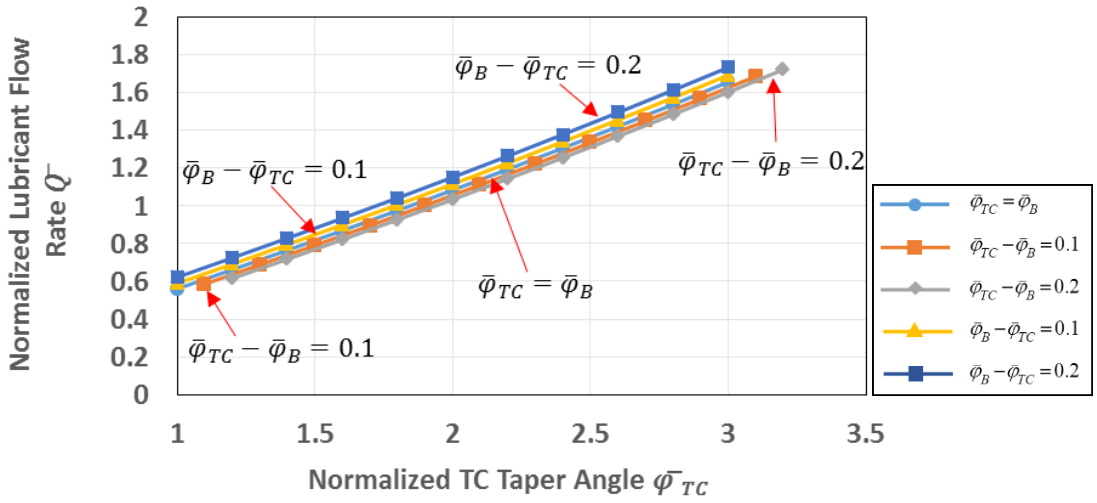

Figure 18. Lubricant flow rate ($\bar{Q}$) versus thrust collar taper angle ($\bar{\varphi}_{TC}$). $\bar{W} = 1, \bar{\omega} = 10, R_2/R_1 = 7.14$.

In the lubricated zone, heat is conducted into the bounding surfaces and carried away by the moving fluid. For the predictions in Figure 19, the TC and BG surfaces are maintained at an arbitrary constant, steady state, temperature of 50 °C, slightly above (+ 1 °C) that of the lubricant supply temperature (listed in Table 1). Figure 17 displays the lubricant temperature rise ($\Delta\bar{T}$) versus TC taper angle for the five taper angle configurations under investigation. The lubricant temperature rise decreases with increasing TC taper angle for all of the taper angle configurations under investigation. Although the configurations in which $\bar{\varphi}_{TC} > \bar{\varphi}_B$ have slightly smaller lubricant flow rates (as shown in Figure 18), these taper configurations also produce less mechanical power

loss (as shown in Figure 17). For the five taper configurations, the lubricant temperature rise is small for the listed operating conditions.

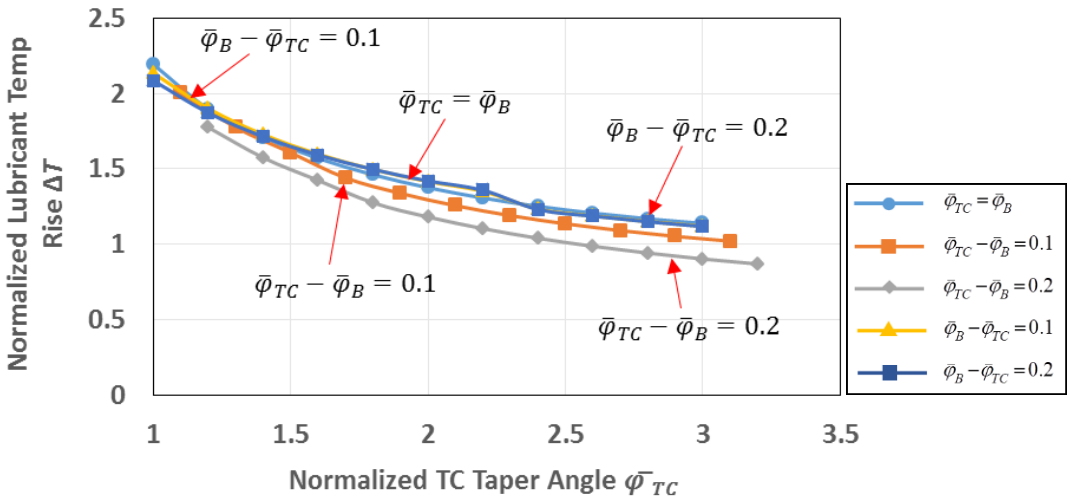

Figure 19. Lubricant temperature rise ($\Delta\bar{T}$) versus thrust collar taper angle ($\bar{\varphi}_{TC}$). $\bar{W} = 1, \bar{\omega} = 10, R_2/R_1 = 7.14$.

Figure 20 displays the fluid film axial stiffness ($\bar{K}_{zz}$) versus TC taper angle. For equal taper angles, or small differences between the two taper angles ($\bar{\varphi}_B = \bar{\varphi}_{TC}$ or $\bar{\varphi}_B - \bar{\varphi}_{TC} = \pm 0.1$), the axial stiffness decreases with increasing taper angle, almost reaching a constant value after $\bar{\varphi}_{TC} = 2.4$. When there is a slightly larger difference between the taper angles ($\bar{\varphi}_B - \bar{\varphi}_{TC} = \pm 0.2$) the axial stiffness reaches a minimum at approximately $\bar{\varphi}_{TC} = 2.0$ then increases with increasing taper angle. As the difference

between the TC taper and BG taper increases, the minimum film thickness in the lubricated zone decreases, leading to larger axial stiffnesses.

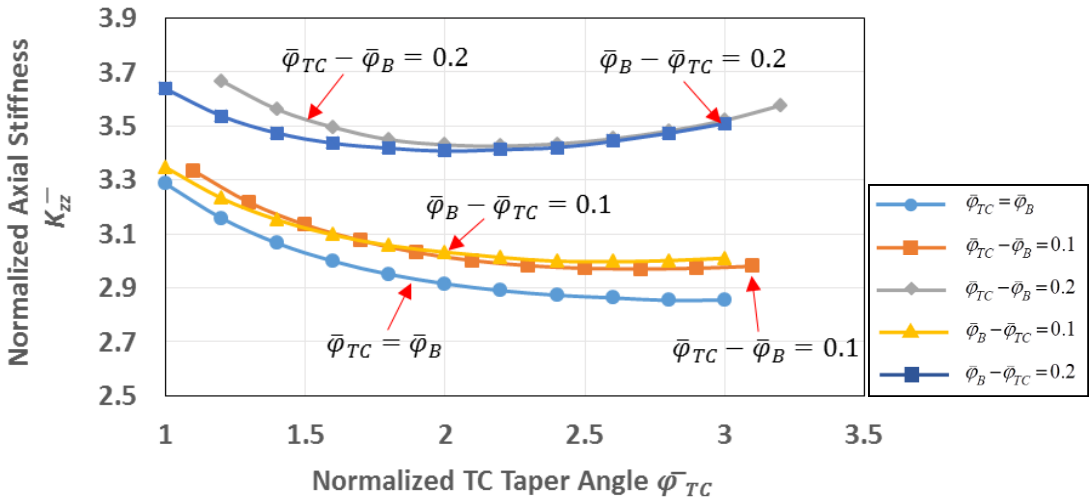

Figure 20. Axial stiffness ($\bar{K}_{zz}$) versus thrust collar taper angle ($\bar{\varphi}_{TC}$). $\bar{W} = 1, \bar{\omega} = 10, R_2/R_1 = 7.14$.

Figures 21 (a) & (b) display the moment-angle stiffnesses $\left(\overline{K}_{\alpha_x\alpha_x}, \overline{K}_{\alpha_y\alpha_y}, \overline{K}_{\alpha_x\alpha_y}, \overline{K}_{\alpha_y\alpha_x}\right)$ versus normalized TC taper angle for the five TC taper configurations. The majority of the moment coefficients, with the exception of $\overline{K}_{\alpha_y\alpha_x}$, decrease slightly with an increase in taper angles. The direct coefficients ($\overline{K}_{\alpha_x\alpha_x}, \overline{K}_{\alpha_y\alpha_y}$) are not equal, as expected, due to the asymmetric shape of the lubricated zone. In addition, $\left|\overline{K}_{\alpha_x\alpha_x}\right| < \overline{K}_{\alpha_y\alpha_y}$ since the moment arm is small (pressure is near the axis of

rotation). Despite the geometric asymmetry of the lubricated zone, the cross coupled moment-angle coefficients show $\overline{K}_{\alpha_x\alpha_y} \sim -\overline{K}_{\alpha_y\alpha_x}$ indicating a strong (hydrodynamic) cross-coupling.

When comparing the moment stiffnesses amongst the five taper configurations, notice that only one angular stiffness ($\overline{K}_{\alpha_y\alpha_y}$) (shown in Figure 21 (b)) differs amongst the TC/BG taper configurations. The three other angular stiffness coefficients ($\overline{K}_{\alpha_x\alpha_x}, \overline{K}_{\alpha_x\alpha_y}, \overline{K}_{\alpha_y\alpha_x}$) are approximately equal for the five taper configurations. As with the axial stiffness coefficients, the normalized moment-angle stiffness coefficients differ only slightly with each taper angle configuration, showing no direct advantage or disadvantage for either taper configuration or specific taper angle.

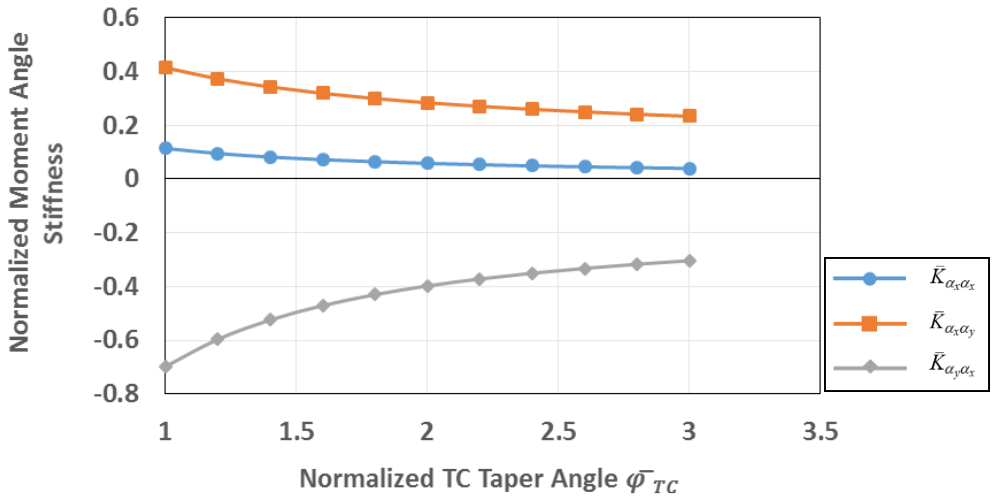

[a] $\overline{K}_{\alpha_x\alpha_x}, \overline{K}_{\alpha_x\alpha_y}, \overline{K}_{\alpha_y\alpha_x}$

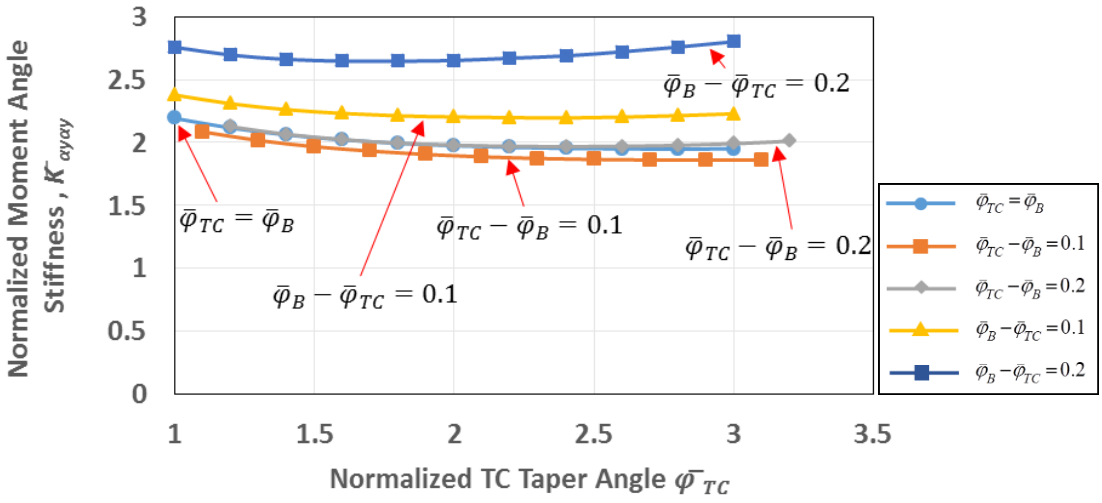

[b] $\overline{K}_{\alpha_y\alpha_y}$

Figure 21. Moment Angle stiffness [a] $\overline{K}_{\alpha_x\alpha_x}, \overline{K}_{\alpha_x\alpha_y}, \overline{K}_{\alpha_y\alpha_x}$ and [b] $\overline{K}_{\alpha_y\alpha_y}$ versus thrust collar taper angle ($\bar{\varphi}_{TC}$). $\bar{W} = 1, \bar{\omega} = 10, R_2/R_1 = 7.14$.

Figure 22 (a) & (b) display the axial force-angle stiffnesses $\left(\overline{K}_{z\alpha_x}, \overline{K}_{z\alpha_y}\right)$ and moment-axial displacement stiffnesses $\left(\overline{K}_{\alpha_x z}, \overline{K}_{\alpha_y z}\right)$ versus normalized thrust collar taper angle. Note that $\overline{K}_{\alpha_y z} = \overline{K}_{z\alpha_y}$ and $\overline{K}_{\alpha_x z} \sim -\overline{K}_{z\alpha_x}$ denoting a strong (hydrodynamic) cross-coupling. There is no discernable difference in stiffnesses $\left(\overline{K}_{z\alpha_x}, \overline{K}_{\alpha_x z}\right)$ amongst the five taper configurations, while both $\overline{K}_{z\alpha_y} = \overline{K}_{\alpha_y z}$ increase when $\bar{\varphi}_B > \bar{\varphi}_{TC}$ or $\bar{\varphi}_{TC} > \bar{\varphi}_B$.

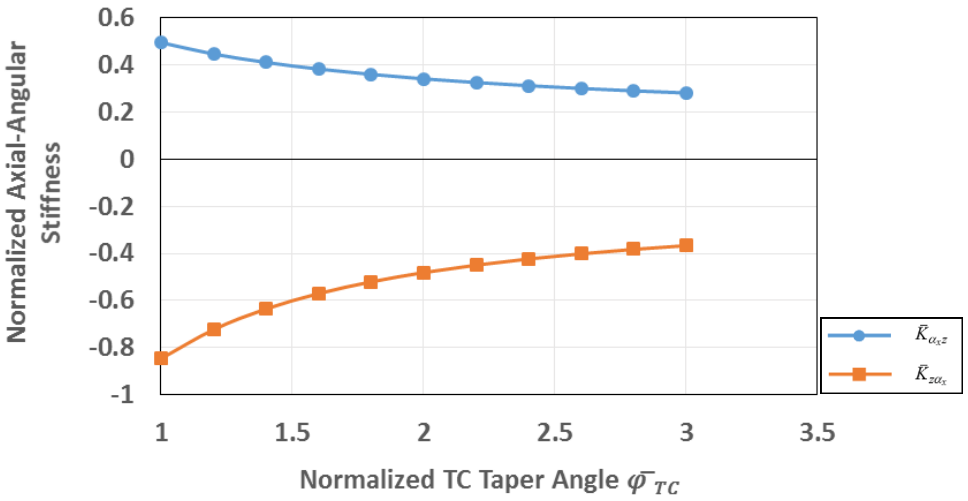

[a] $\overline{K}_{\alpha_x z} \sim -\overline{K}_{z\alpha_x}$

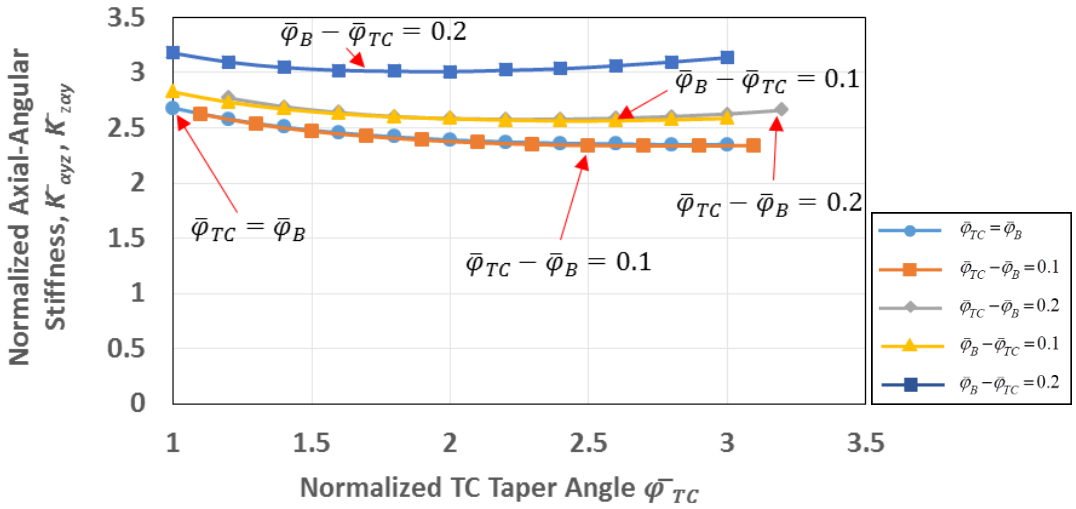

[b] $\overline{K}_{\alpha_y z} = \overline{K}_{z\alpha_y}$

Figure 22. Axial-angular stiffness [a] $\overline{K}_{\alpha_x z}$, $\overline{K}_{z\alpha_x}$ and [b] $\overline{K}_{\alpha_y z}, \overline{K}_{z\alpha_y}$ versus thrust collar taper angle ($\bar{\varphi}_{TC}$). $\bar{W} = 1, \bar{\omega} = 10, R_2/R_1 = 7.14$.

Figure 23 displays the axial force damping coefficient ($\bar{C}_{zz}$) versus TC taper angle for the five TC/BG taper configurations. $\bar{C}_{zz}$ decreases monotonically with an increase in TC taper angle. In addition, note there is no significant difference in axial damping between the taper configuration with $\bar{\varphi}_{TC} = \bar{\varphi}_B$ and the configuration in which $\bar{\varphi}_B > \bar{\varphi}_{TC}$; however, when the TC taper is slightly larger than the BG taper angle ($\bar{\varphi}_{TC} > \bar{\varphi}_B$ by 0.2), the axial damping increases slightly. The differences in damping amongst the configurations is minor, thus neither configuration offers a significant advantage over each other.

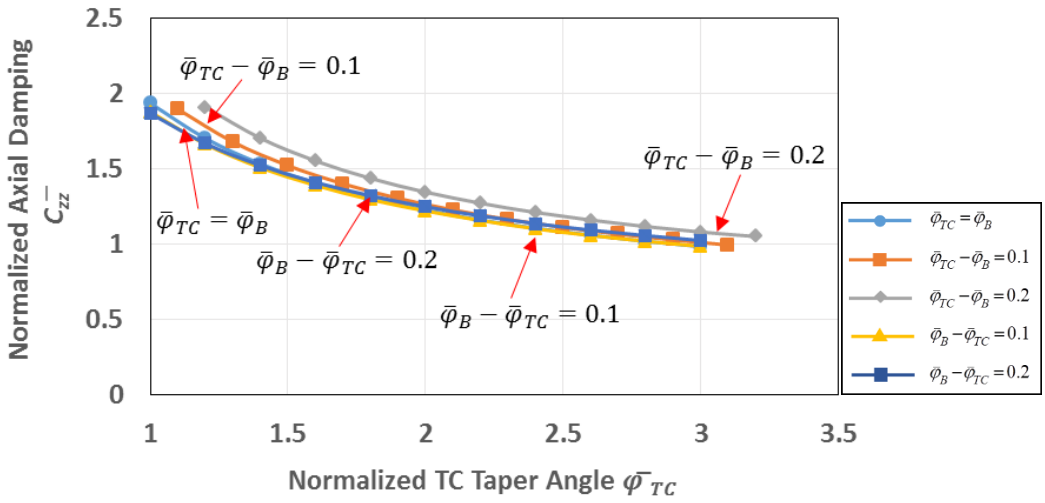

Figure 23. Axial damping ($\bar{C}_{zz}$) versus thrust collar taper angle ($\bar{\varphi}_{TC}$). $\bar{W} = 1, \bar{\omega} = 10, R_2/R_1 = 7.14$.

Figure 24 (a) and (b) display the moment-angular speed damping coefficients $\left(\bar{C}_{\alpha_x\alpha_x}, \bar{C}_{\alpha_y\alpha_y}, \bar{C}_{\alpha_x\alpha_y}, \bar{C}_{\alpha_y\alpha_x}\right)$ versus thrust collar taper angle. The direct moment damping

$\overline{C}_{\alpha_x\alpha_x}$ is approximately zero, again due to the small moment arm (i.e., pressure is near the axis of rotation, as denoted earlier). In addition, the cross-coupled damping coefficients ($\overline{C}_{\alpha_x\alpha_y}, \overline{C}_{\alpha_y\alpha_x}$) are nearly zero.

The direct moment-angular speed damping coefficient $\overline{C}_{\alpha_y\alpha_y}$ decreases with an increasing thrust collar taper angle, differing slightly amongst the taper configurations. As the taper angle increases and the gap between the TC and BG becomes larger, a decrease in film damping indicates a lessening of squeeze film effects.

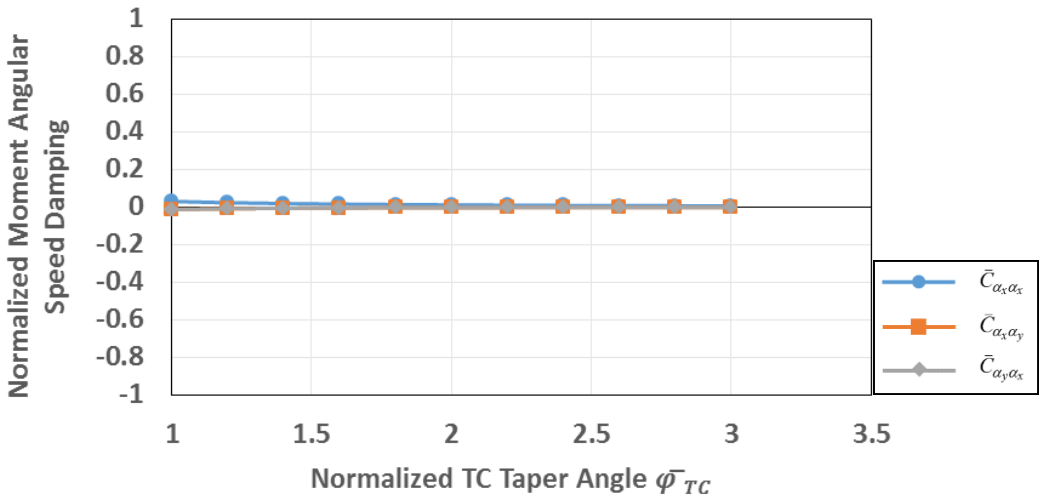

[a] $\overline{C}_{\alpha_x\alpha_x}$, $\overline{C}_{\alpha_x\alpha_y}$, $\overline{C}_{\alpha_y\alpha_x}$

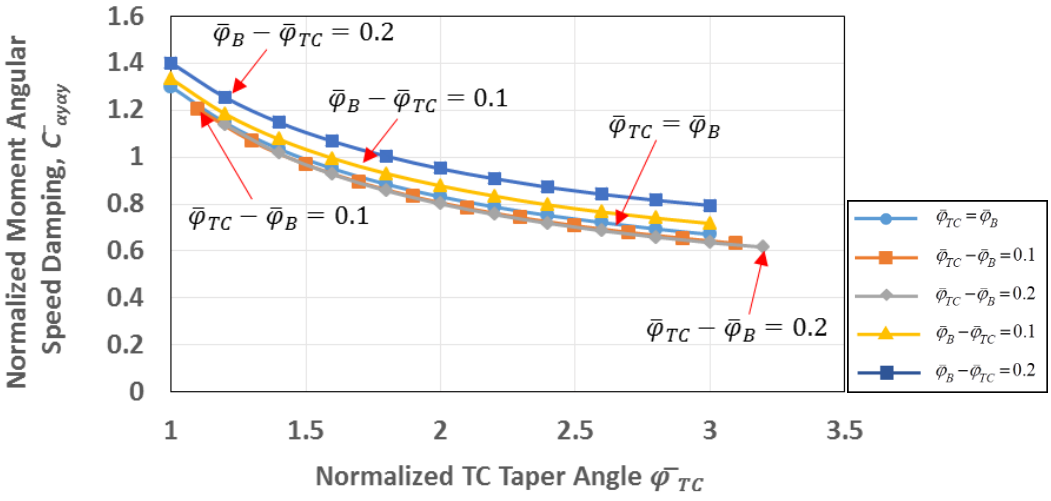

[b] $\overline{C}_{\alpha_y\alpha_y}$

Figure 24. Moment angular speed damping [a] $\overline{C}_{\alpha_x\alpha_x}, \overline{C}_{\alpha_x\alpha_y}, \overline{C}_{\alpha_y\alpha_x}$ and [b] $\overline{C}_{\alpha_y\alpha_y}$ versus thrust collar taper angle ($\bar{\varphi}_{TC}$). $\bar{W} = 1, \bar{\omega} = 10, R_2/R_1 = 7.14$.

Figure 25 (a) & (b) display the axial force-angular velocity damping coefficients ($\overline{C}_{z\alpha_x}, \overline{C}_{z\alpha_y}$) and moment-axial velocity damping coefficients ($\overline{C}_{\alpha_x z}, \overline{C}_{\alpha_y z}$) versus thrust collar taper angle. As with the axial-angular stiffness, $\overline{C}_{z\alpha_y}, \overline{C}_{\alpha_y z}$ for the various taper configurations and does not vary with taper configuration. In addition, note $\overline{C}_{z\alpha_x} = \overline{C}_{\alpha_x z} \approx 0$.

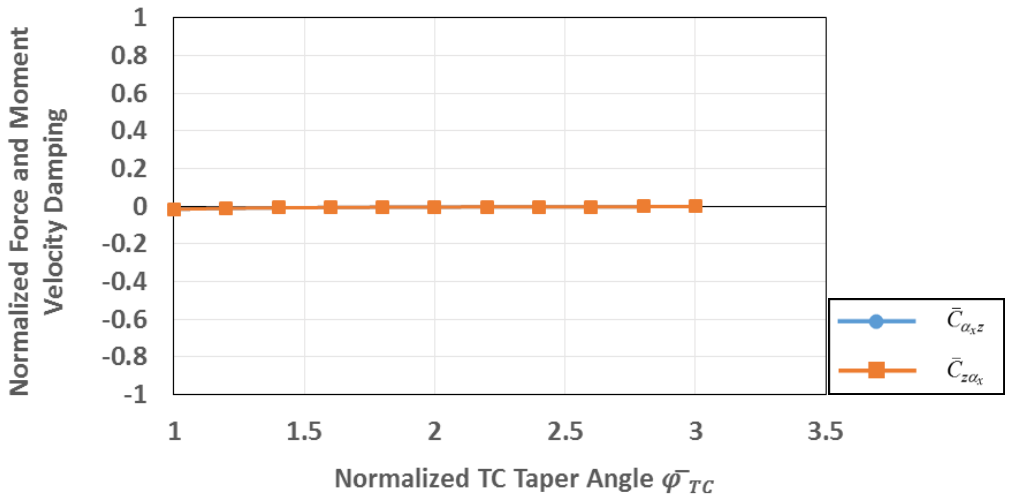

[a] $\bar{C}_{z\alpha_x} = \bar{C}_{\alpha_x z}$

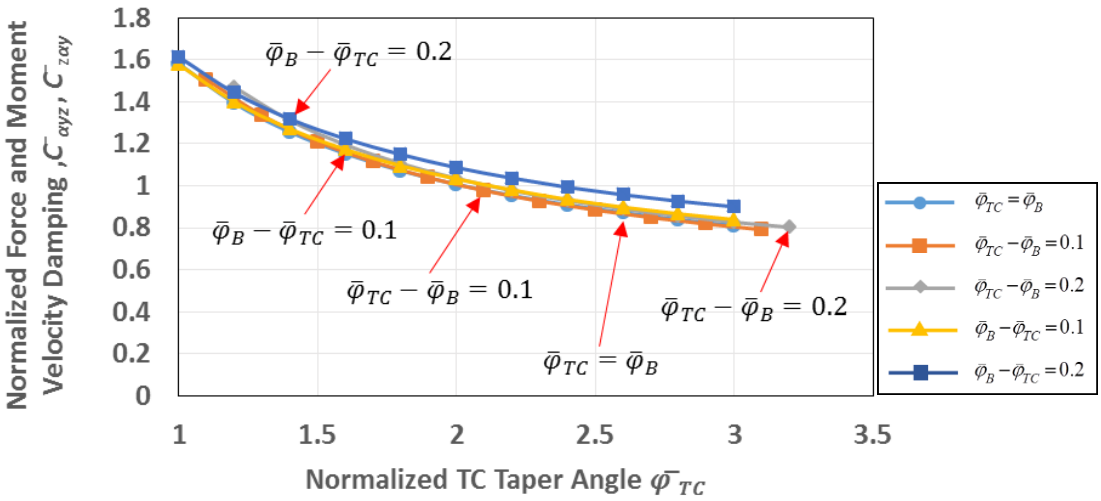

[b] $\bar{C}_{z\alpha_y} = \bar{C}_{\alpha_y z}$

Figure 25. Force and moment velocity damping [a] $\bar{C}_{z\alpha_x}, \bar{C}_{\alpha_x z}$ and [b] $\bar{C}_{z\alpha_y} = \bar{C}_{\alpha_y z}$ versus thrust collar taper angle ($\bar{\varphi}_{TC}$). $\bar{W} = 1, \bar{\omega} = 10, R_2/R_1 = 7.14$

.

Recall from Eq. (51) the equation for changes in axial force and moments on the TC is

$$-\begin{bmatrix} -\Delta F_{z,TC} \\ \Delta M_{TC,x} \\ \Delta M_{TC,y} \end{bmatrix} = \begin{bmatrix} H_{zz} & H_{z\alpha_x} & H_{z\alpha_y} \\ H_{\alpha_x z} & H_{\alpha_x\alpha_x} & H_{\alpha_x\alpha_y} \\ H_{\alpha_y z} & H_{\alpha_y\alpha_x} & H_{\alpha_y\alpha_y} \end{bmatrix} \begin{Bmatrix} \Delta z \\ \Delta\alpha_x - \Delta\beta_x \\ \Delta\alpha_y - \Delta\beta_y \end{Bmatrix} + d \begin{bmatrix} H_{zz} \\ H_{\alpha_x z} \\ H_{\alpha_y z} \end{bmatrix} \Delta\beta_y \qquad (82)$$

With the stiffness and damping coefficients presented in Figures 18-23, the dynamic stiffness matrix from Eq. (51) takes the form

$$-\begin{bmatrix} -\Delta F_{z,TC} \\ \Delta M_{TC,x} \\ \Delta M_{TC,y} \end{bmatrix} = \begin{bmatrix} K_{zz} + i\omega C_{zz} & K_{z\alpha_x} & K_{z\alpha_y} + i\omega C_{z\alpha_y} \\ -K_{z\alpha_x} & \sim 0 & K_{\alpha_x\alpha_y} \\ K_{z\alpha_y} + i\omega C_{z\alpha_y} & -K_{\alpha_x\alpha_y} & K_{\alpha_y\alpha_y} + i\omega C_{\alpha_y\alpha_y} \end{bmatrix} \begin{Bmatrix} \Delta z \\ \Delta\alpha_x - \Delta\beta_x \\ \Delta\alpha_y - \Delta\beta_y \end{Bmatrix} + d \begin{bmatrix} K_{zz} + i\omega C_{zz} \\ -K_{\alpha_x z} \\ K_{\alpha_y z} + i\omega C_{\alpha_y z} \end{bmatrix} \Delta\beta_y \qquad (83)$$

The first matrix in Eq. (83) reveals several symmetries for a lubricated TC. In addition, some of the axial-angular terms ($K_{z\alpha_x}$, $K_{z\alpha_y}$) are nonzero, indicating a coupling between axial and angular motions of the pinion and bull gear shafts. The matrix above suggests that lubricated thrust collars may have an effect on the lateral rotordynamics of the pinion and bull shaft in an IGC[8].

[8] Not studied in detail in this work.

PREDICTIONS FOR THE PERFORMANCE OF A STATICALLY MISALIGNED THRUST COLLAR

The previous analysis assumes that the thrust collar and bull gear are perfectly aligned during operation. In industrial integrally geared compressors, the TCs and BG are never perfectly aligned, due to imperfections in the machining or assembly process, or misalignment during operation. As such, to understand how lubricated TCs perform with various degrees of static angular misalignment is important.

Recall from the lubricated thrust collar model that the film thickness between a TC and BG is (refer to the schematic in Figure 5 on pg. 14)

$$h(r,\theta) = h_{R_1} + (R_1 - d + b)\tan(\varphi_B) - (R_1 - r)\tan(\varphi_{TC}) + r\cos(\theta)\{\alpha_y - \beta_y\} + d\ \beta_y + r\sin(\theta)\{\beta_x - \alpha_x\} \quad (1),(84)$$

where angles (α_x, α_y) refer to static misalignments (or tilts) of the TC, and angles (β_x, β_y) refer to static misalignments (or tilts) of the BG about the *x* and *y* axes, respectively.

Figures 26 and 27 display contours of the film thickness and hydrodynamic pressure field, respectively, in the lubricated zone for a TC with static angle misalignment about a specific axis while the other misalignment angles are nil. Note that in the following plots, the thrust load is $\bar{W} = 1$, as in the previous analysis, and $\bar{\varphi}_{TC} = \bar{\varphi}_B = 1.0$. Table 1 lists other operating conditions, including rotational speed. Normalized static tilts of the TC about the *x* and *y* axes are

$$\bar{\alpha}_x = \frac{\alpha_x}{\varphi^*}\ ,\ \bar{\alpha}_y = \frac{\alpha_y}{\varphi^*} \quad (85)$$

As seen in Eq. (84), Figure 26 shows graphically that a positive (towards the BG) rotation of the TC about the *x* axis ($\bar{\alpha}_x > 0.0$) produces the same film thickness as a negative rotation of the BG about the same *x* axis ($\bar{\beta}_x < 0$). If either the TC has $\bar{\alpha}_x < 0$ or the BG has $\bar{\beta}_x > 0$, the film thickness in the upper half of the lubricated zone ($\theta > 0$) is the smallest. On the other hand, if either the TC has $\bar{\alpha}_x > 0$ or the BG has $\bar{\beta}_x < 0$, the film thickness in the lower half of the lubricated zone ($\theta < 0$) is the smallest.

Considering the contours plots in both Figures 26 and 27, the peak pressure shifts to the location of the minimum film thickness. In addition, note that the hydrodynamic pressure acts over a larger area as the angle $\bar{\alpha}_x$ increases. This increase in the extent of the hydrodynamic pressure relates to a larger load carrying area. Conversely, the figures show that the lubricant cavitation area decreases with increasing angle ($\bar{\alpha}_x$). A larger load carrying area relates to a lower peak pressure but also produces an increase in shear power loss.

Misalignment of TC about *x* axis

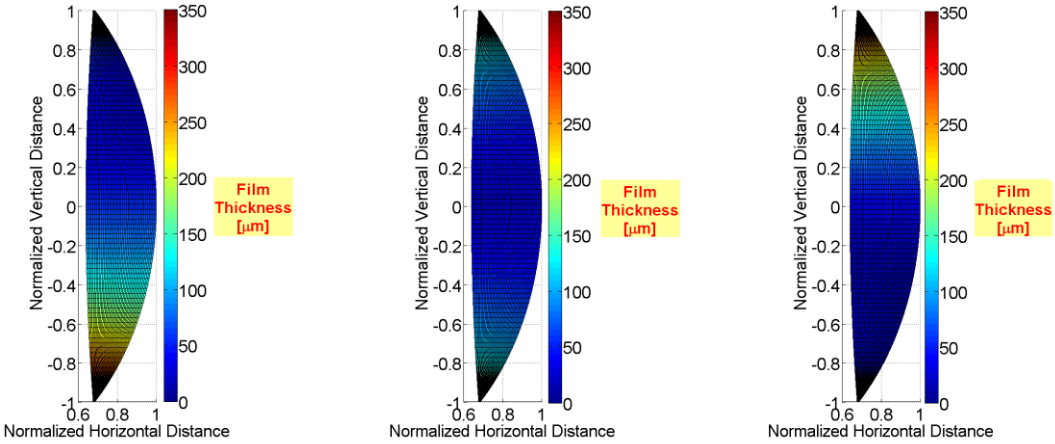

(a) Positive TC Misalignment $\bar{\alpha}_x = 0.4, \bar{\alpha}_y = \bar{\beta}_x = \bar{\beta}_y = 0$

(b) No misalignment $\bar{\alpha}_x = 0, \bar{\alpha}_y = \bar{\beta}_x = \bar{\beta}_y = 0$

(c) Negative TC Misalignment $\bar{\alpha}_x = -0.4, \bar{\alpha}_y = \bar{\beta}_x = \bar{\beta}_y = 0$

Misalignment of BG about *x* axis

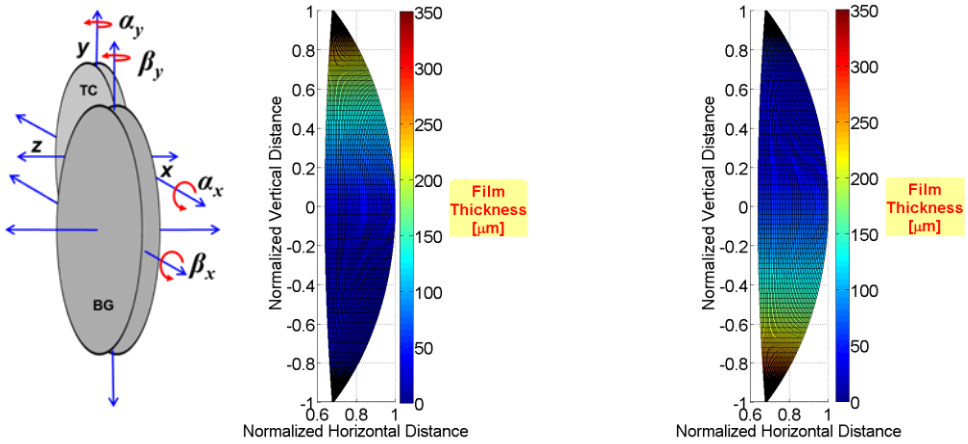

d) Negative BG Misalignment $\bar{\beta}_x = -0.4, \bar{\alpha}_x = \bar{\alpha}_y = \bar{\beta}_y = 0$

(e) Positive BG Misalignment $\bar{\beta}_x = 0.4, \bar{\alpha}_x = \bar{\alpha}_y = \bar{\beta}_y = 0$

Figure 26. Contour plots of film thickness in the lubricated zone for a TC and BG with angular misalignment about the *x* axis. Properties and operating conditions as in Table 1. $\bar{W} = 1.0,\ \bar{\varphi}_{TC} = \bar{\varphi}_B = 1.0,\ \bar{\omega}$=10 **.**

Misalignment of TC about *x* axis

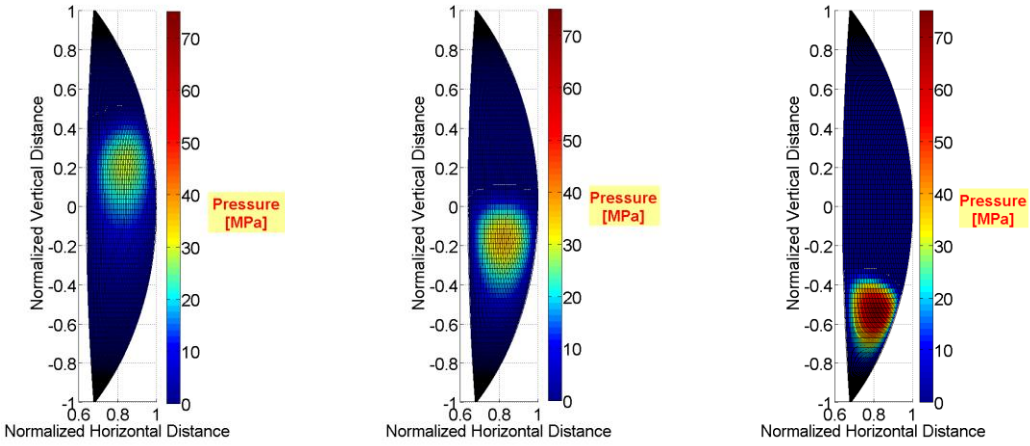

(a) Positive TC Misalignment $\bar{\alpha}_x = 0.4, \bar{\alpha}_y = \bar{\beta}_x = \bar{\beta}_y = 0$

(b) No misalignment $\bar{\alpha}_x = 0, \bar{\alpha}_y = \bar{\beta}_x = \bar{\beta}_y = 0$

(c) Negative TC Misalignment $\bar{\alpha}_x = -0.4, \bar{\alpha}_y = \bar{\beta}_x = \bar{\beta}_y = 0$

Misalignment of BG about *x* axis

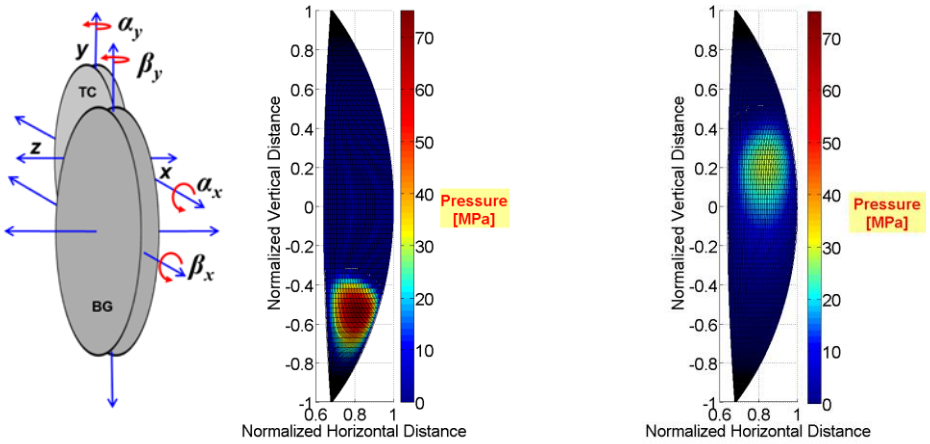

(d) Negative BG Misalignment $\bar{\beta}_x = -0.4, \bar{\alpha}_x = \bar{\alpha}_y = \bar{\beta}_y = 0$

(e) Positive BG Misalignment $\bar{\beta}_x = 0.4, \bar{\alpha}_x = \bar{\alpha}_y = \bar{\beta}_y = 0$

Figure 27. Contour plots of hydrodynamic pressure in the lubricated zone for a TC and BG with angular misalignment about the *x* axis. Properties and operating conditions as in Table 1. $\bar{W} = 1.0,\ \bar{\varphi}_{TC} = \bar{\varphi}_B = 1.0,\ \bar{\omega}$=10 **.**

From Eq. (84), clearly a misalignment ($\bar{\alpha}_y$) of the TC about the *y* axis produces a different film thickness than a misalignment ($\bar{\beta}_y$) of the BG about the *y* axis. If the TC remained in the same axial position as the BG tilts, the resulting film thickness from the small tilt ($\bar{\beta}_y = 0.2$) is too large to generate a hydrodynamic pressure field that balances the applied thrust load. As such, to support the axial load, the pinion shaft must translate axially to decrease the gap between the TC and BG.

Figure 28 (a) shows a perfectly aligned thrust collar and bull gear with $h_{R1} > 0$. If either the BG or TC is misaligned, $h_{R1} < 0$ at $r = R_1$ can still produce a film thickness, as depicted in the schematic in Figure 28 (b)[9]. Thus, when the TC or BG is misaligned about the vertical (*y*) axis, h_{R1} may be negative in order to produce a film thickness which generates a large enough pressure field to oppose a thrust load.

[9] Note that the helical gear teeth are not included in the schematic view in Figure 28 (b). In addition, the tilt of the BG is overdramatized.

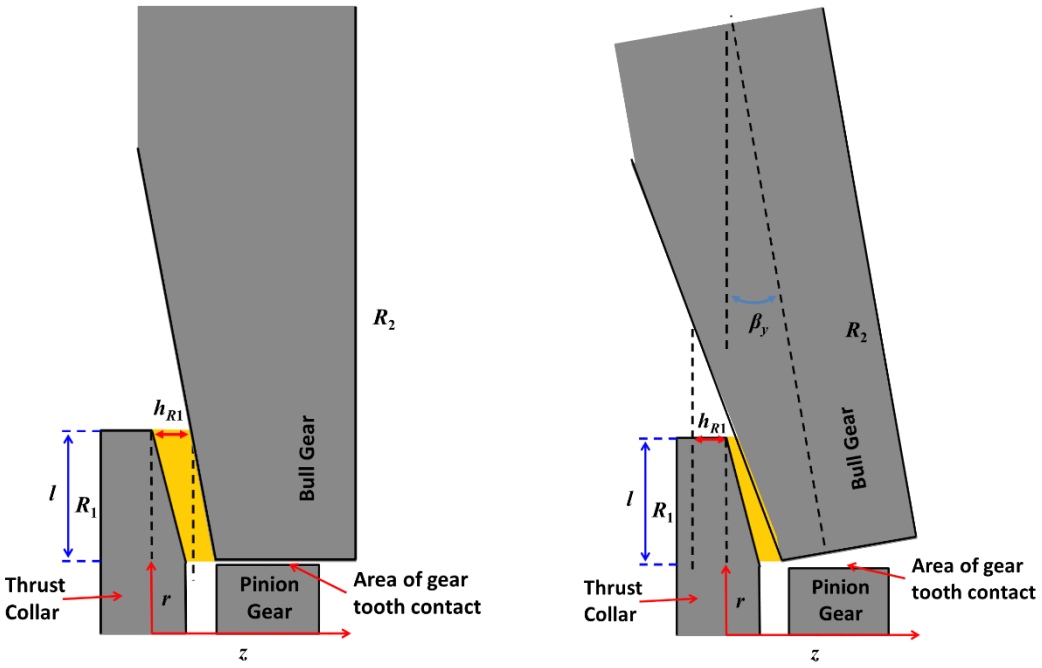

(a) TC/BG with no misalignment (b) $\bar{\beta}_y = 0.4, \bar{\alpha}_x = \bar{\alpha}_y = \bar{\beta}_x = 0$

Figure 28. Schematic views of the lubricated zone in which there is (a) no angle misalignment and (b) misalignment of the BG about the vertical axis ($\beta_y > 0$).

The geometry and operating conditions of the TC/BG pair, as well as the lubricant properties used in the following analysis are identical to those in the previous section, and listed in Table 1. In the preceding chapter, the performance parameters of the TC/BG pair are analyzed for various taper angles. For the following analysis the TC/BG taper angles are fixed ($\bar{\varphi}_{TC} = \bar{\varphi}_B = 1.0$), while the static misalignment angles of both bodies vary.

Figures 29 (a-d) display the normalized minimum film thickness versus static misalignment angle $\bar{\alpha}_x, \bar{\beta}_x, \bar{\alpha}_y,$ or $\bar{\beta}_y$. In the following plots, one misalignment angle is varied while the other angles are nil (i.e. $-0.2 \le \bar{\alpha}_x \le 0.2, \bar{\beta}_x = \bar{\alpha}_y = \bar{\beta}_y = 0$). Recall that a tilt ($\bar{\alpha}_x$) of the TC about the *x* axis produces an identical film thickness as a tilt of the BG in the opposite direction ($-\bar{\beta}_x$), as shown in Figures 29 (a) and (b). When the TC is misaligned about the *x* axis ($\bar{\alpha}_x < 0$) or the BG is misaligned about the *x* axis ($\bar{\beta}_x > 0$), the bottom portion of the lubricated zone ($\theta < 0$) has a dramatically smaller film thickness, as depicted in Figures 26 (a) and (e). On the other hand, for a TC with a misalignment $\bar{\alpha}_x > 0$ or a BG with a misalignment $\bar{\beta}_x < 0$, the film thickness in the upper half ($\theta > 0$) of the lubricated zone decreases; see Figures 26 (c) and (d).

As noted, tilts $\bar{\beta}_y$ of the BG or $\bar{\alpha}_y$ of the TC about the vertical axis do not produce the same film thickness if $h_{R1} > 0$. However, to support the thrust loads $\bar{W} = 1$ when the BG is misaligned, the pinion shaft translates axially to bring the TC closer to the BG (i.e., $h_{R1} < 0$) as displayed schematically in Figure 28. This produces a film thickness identical to the film thickness when the thrust collar is misaligned about the vertical axis. Thus, just as in Figure 26 (a & b), a tilt ($\bar{\alpha}_y$) of the TC about the *y* axis produces an identical film thickness as a tilt of the BG in the opposite direction ($-\bar{\beta}_y$). Figures 29 (c) and (d) show that the film thickness required to support the thrust load is nearly

symmetric about the aligned condition ($\bar{\alpha}_x = \bar{\alpha}_y = \bar{\beta}_x = \bar{\beta}_y = 0$). Because tilts $\bar{\alpha}_x$, $\bar{\beta}_x$ produce equal and opposite film thicknesses as $\bar{\alpha}_y$, $\bar{\beta}_y$, the remaining analysis focuses on the TC misalignment angles $\bar{\alpha}_x$ and $\bar{\alpha}_y$.

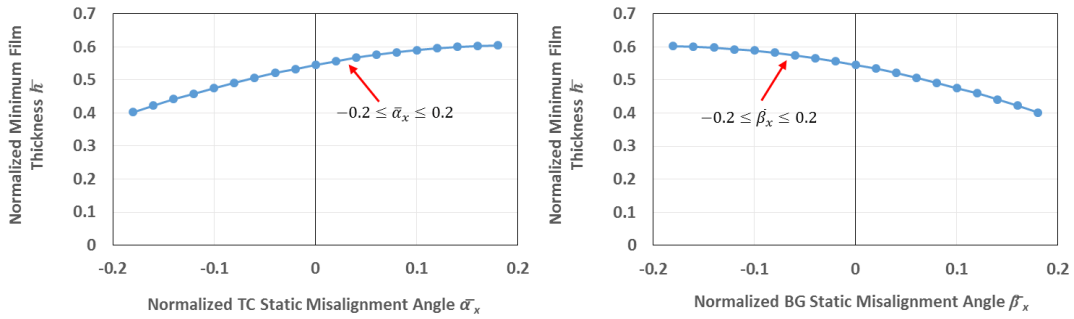

[a] $-0.2 \le \bar{\alpha}_x \le 0.2, \bar{\beta}_x = \bar{\alpha}_y = \bar{\beta}_y = 0$ [b] $-0.2 \le \bar{\beta}_x \le 0.2, \bar{\alpha}_x = \bar{\alpha}_y = \bar{\beta}_y = 0$

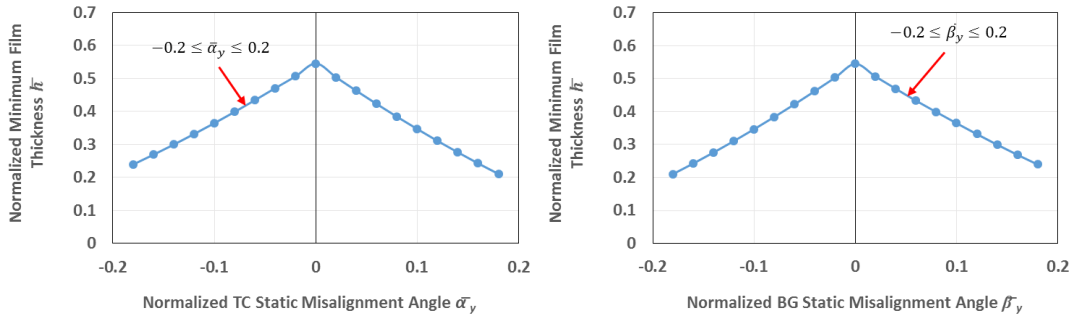

[c] $-0.2 \le \bar{\alpha}_y \le 0.2, \bar{\alpha}_x = \bar{\beta}_x = \bar{\beta}_y = 0$ [d] $-0.2 \le \bar{\beta}_y \le 0.2, \bar{\alpha}_x = \bar{\alpha}_y = \bar{\beta}_x = 0$

Figure 29. Normalized film thickness ($\bar{h}_{\min}$) versus [a] TC misalignment angle $\bar{\alpha}_x$, [b] BG misalignment angle $\bar{\beta}_x$, [c] TC misalignment angle $\bar{\alpha}_y$ and [d] BG misalignment angle $\bar{\beta}_y$. $\bar{W} = 1, \bar{\omega} = 10$, $R_2/R_1 = 7.14$, $\bar{\varphi}_{TC} = \bar{\varphi}_B = 1.0$.

Figure 30 presents the peak hydrodynamic pressure in the lubricated zone versus TC misalignment angle (either $\bar{\alpha}_x$ or $\bar{\alpha}_y$) for a TC/BG pair with operating conditions and geometry as presented in Table 1. In each of the following plots the individual trends are marked as either $\bar{\alpha}_x$ or $\bar{\alpha}_y$, to indicate which horizontal axis the trend is associated with. In Figure 30, for example, the trend labeled $\bar{\alpha}_x$ refers to the peak hydrodynamic pressure for static angular misalignments $-0.2 \le \bar{\alpha}_x \le 0.2, \bar{\beta}_x = \bar{\alpha}_y = \bar{\beta}_y = 0$. For reference, refer to the insert next to the plot for the directions of positive and negative rotations of the TC and BG about both axes.

The predictions in Figure 30 show that the peak hydrodynamic pressure is approximately symmetric about the aligned condition $\bar{\alpha}_x = \bar{\alpha}_y = \bar{\beta}_x = \bar{\beta}_y = 0$ for angular misalignments of the TC about the *y* axis ($\bar{\alpha}_y$). In contrast, the peak pressure is not symmetric about the aligned condition for angular misalignments about the *x* axis ($\bar{\alpha}_x$). This asymmetry is due to the change in the extent of the lubricant cavitation region. As noted in Figure 26 (a)-(c), the lubricant cavitation region decreases with increasing misalignment angle $\bar{\alpha}_x$, leading to a larger load carrying area, and a smaller peak pressure.

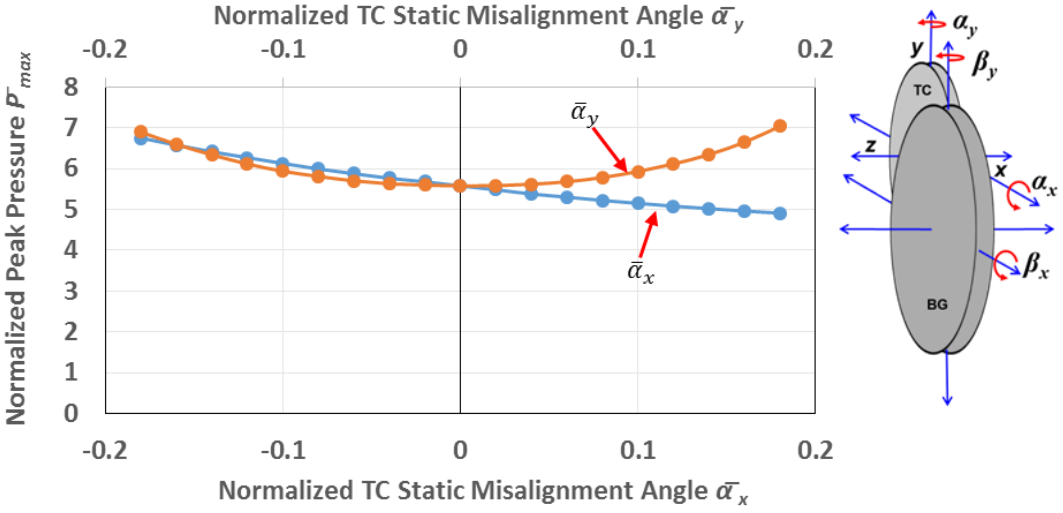

Figure 30. Peak pressure ($\bar{P}_{max}$) versus thrust collar misalignment angle ($\bar{\alpha}_x$ or $\bar{\alpha}_y$). $\bar{W} = 1, \bar{\omega} = 10$, $R_2/R_1 = 7.14$, $\bar{\varphi}_{TC} = \bar{\varphi}_B = 1.0$.

Figure 31 shows the friction factor (*f*) versus TC misalignment angle for a TC/BG with the properties and operating conditions displayed in Table 1. The friction factor (*f*) decreases by ~29% from $\bar{\alpha}_x = -0.2$ to $\bar{\alpha}_x = 0.2$, but does not vary significantly with misalignment angle $\bar{\alpha}_y$. Although the cavitation zone shrinks with increasing misalignment angle $\bar{\alpha}_x$, which increases lubricant shear and mechanical power losses, the resulting rise in flow rate (shown later) dictates the overall decrease in the friction factor.

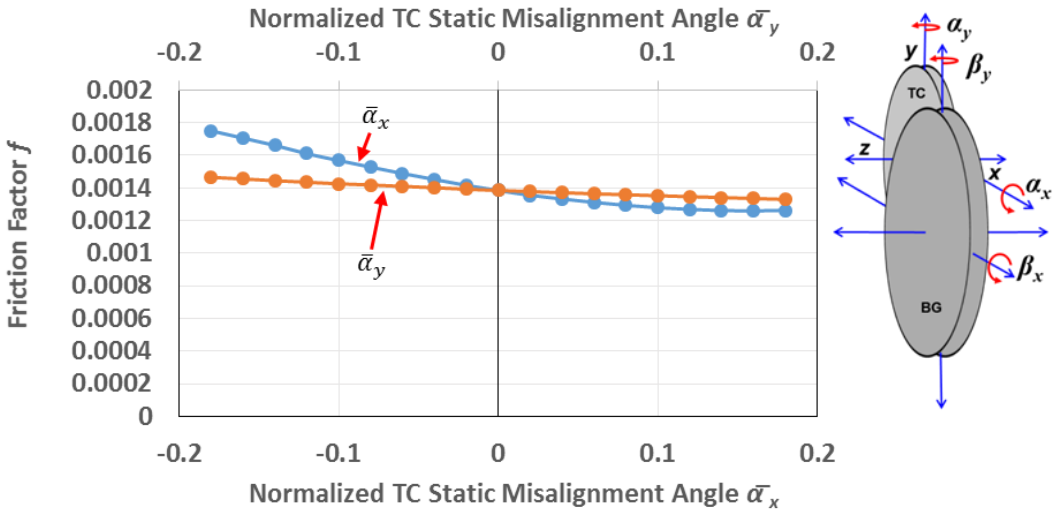

Figure 31. Friction factor (*f*) versus thrust collar misalignment angle ($\bar{\alpha}_x$ or $\bar{\alpha}_y$). $\bar{W} = 1, \bar{\omega} = 10$, $R_2/R_1 = 7.14$, $\bar{\varphi}_{TC} = \bar{\varphi}_B = 1.0$.

Figure 32 displays the lubricant flow rate (Q) required to maintain a full fluid film between the TC taper and BG taper. The predictions show that the lubricant flow rate increases linearly with misalignment angle $\bar{\alpha}_x$, and decreases slightly with increasing misalignment angle $\bar{\alpha}_y$. As with the friction factor, the required lubricant flow rate is effected more by the static angular misalignment of the TC about the *x* axis ($\bar{\alpha}_x$) than by misalignment about the *y* axis ($\bar{\alpha}_y$).

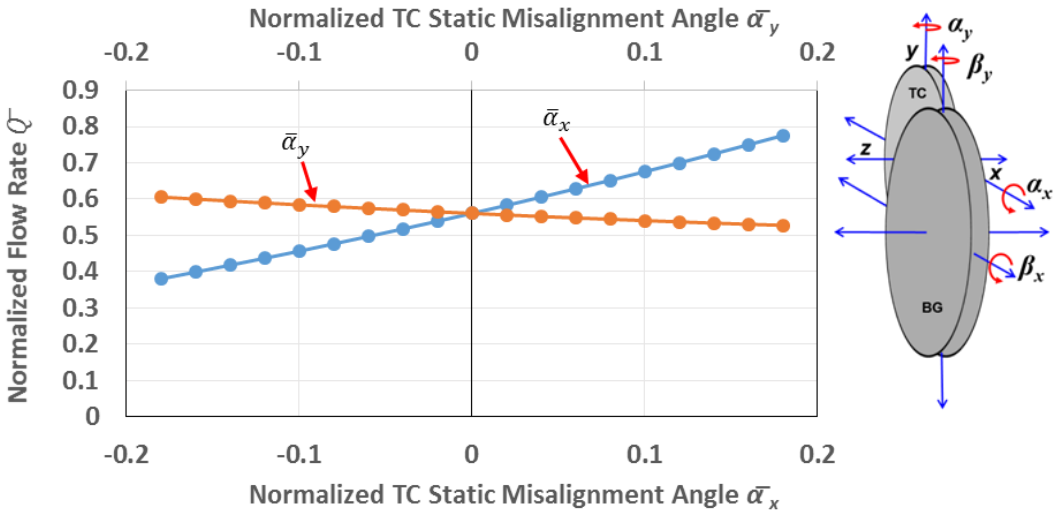

Figure 32. Lubricant flow rate ($\bar{Q}$) versus thrust collar misalignment angle ($\bar{\alpha}_x$ or $\bar{\alpha}_y$). $\bar{W}=1, \bar{\omega}=10$, $R_2/R_1=7.14$, $\bar{\varphi}_{TC}=\bar{\varphi}_B=1.0$.

Figure 33 displays the lubricant temperature rise ($\Delta\bar{T}$) versus TC static angular misalignment. Since the lubricant temperature rise is directly proportional to the mechanical power loss, and inversely proportional to the lubricant flow rate (i.e. proportional to the friction factor), the lubricant temperature rise follows the same trends displayed by *f* in Figure 31; namely, the lubricant temperature rise decreases with increasing misalignment angle $\bar{\alpha}_x$, and remains largely unaffected by angular misalignment $\bar{\alpha}_y$.

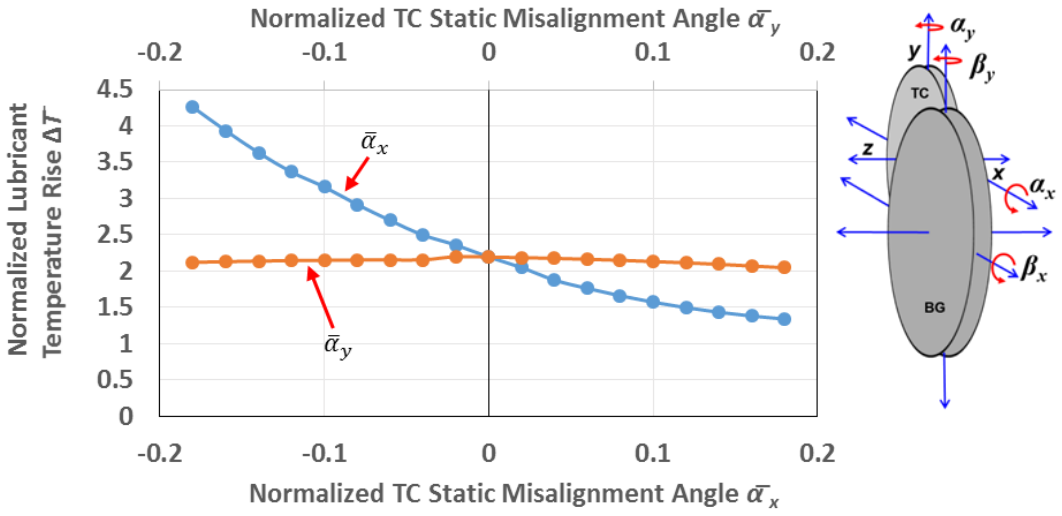

Figure 33. Lubricant temperature rise ($\Delta\bar{T}$) versus thrust collar misalignment angle ($\bar{\alpha}_x$ or $\bar{\alpha}_y$). $\bar{W}=1, \bar{\omega}=10$, $R_2/R_1=7.14$, $\bar{\varphi}_{TC}=\bar{\varphi}_B=1.0$.

Figure 34 displays the fluid film axial stiffness ($\bar{K}_{zz}$) versus TC static misalignment angles. As discussed in the previous chapter, the direct axial stiffness is inversely proportional to the minimum film thickness, and as such, the axial stiffness follows the opposite trend as the minimum film thickness presented in Figure 29 (a) & (c). The direct axial stiffness decreases with increasing angle $\bar{\alpha}_x$ due to the decrease in the extent of the cavitation region. In addition, the direct axial stiffness is nearly symmetric about the aligned condition for the static misalignment angle $\bar{\alpha}_y$.

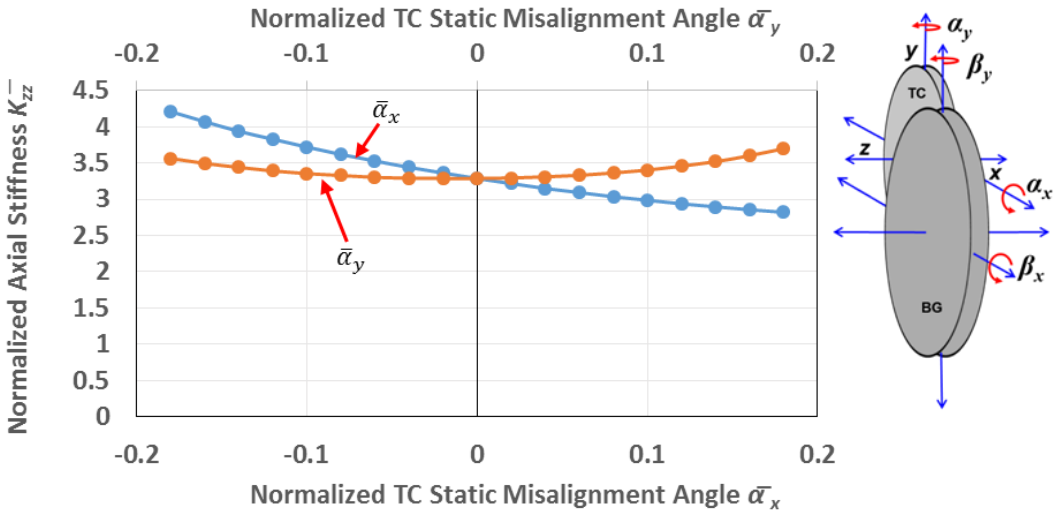

Figure 34. Axial stiffness ($\bar{K}_{zz}$) versus thrust collar misalignment angle ($\bar{\alpha}_x$ or $\bar{\alpha}_y$). $\bar{W}=1, \bar{\omega}=10$, $R_2/R_1=7.14$, $\bar{\varphi}_{TC}=\bar{\varphi}_B=1.0$.

Figures 35 displays the moment-angle stiffnesses $\left(\overline{K}_{\alpha_x\alpha_x}, \overline{K}_{\alpha_y\alpha_y}, \overline{K}_{\alpha_x\alpha_y}, \overline{K}_{\alpha_y\alpha_x}\right)$ versus normalized misalignment angles for TC/BG pair under investigation. Both $\overline{K}_{\alpha_y\alpha_x}$ and $\overline{K}_{\alpha_x\alpha_x}$ are invariant with respect to static misalignment angle (either $\bar{\alpha}_x$ or $\bar{\alpha}_y$) and are equal for the two sets of misalignments. The two other moment-angle coefficients $\overline{K}_{\alpha_x\alpha_y}$ and $\overline{K}_{\alpha_y\alpha_y}$ decrease with increasing misalignment angle $\bar{\alpha}_x$ and $\bar{\alpha}_y$. As with the aligned cases (Figure 21), $\left|\overline{K}_{\alpha_x\alpha_x}\right| < \left|\overline{K}_{\alpha_y\alpha_y}\right|$ since the moment arm is small (pressure is near the axis of rotation). However, unlike the aligned case, $\overline{K}_{\alpha_x\alpha_y} \neq -\overline{K}_{\alpha_y\alpha_x}$ when the TC is misaligned about the *x* axis.

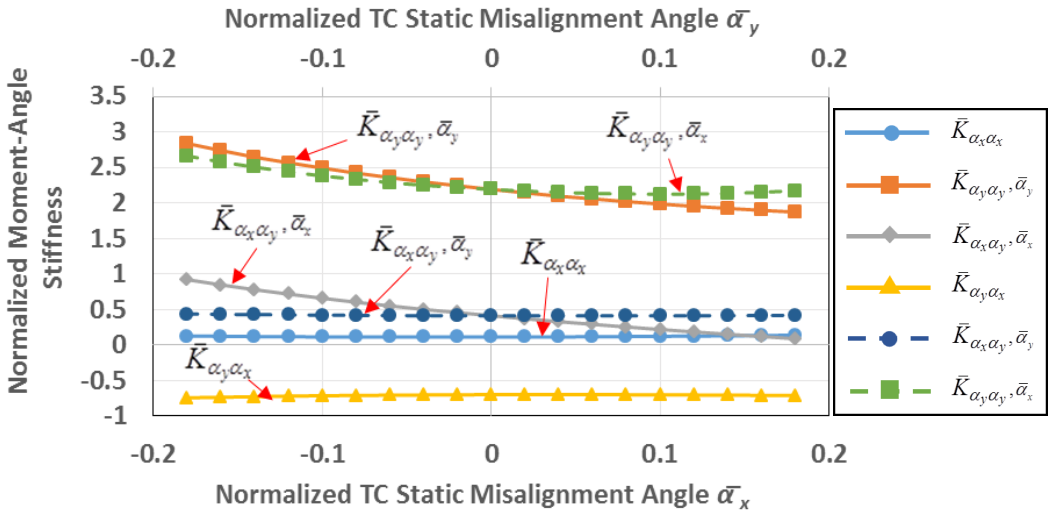

Figure 35. Moment-Angle stiffness versus thrust collar misalignment angle ($\bar{\alpha}_x$ or $\bar{\alpha}_y$). $\bar{W}=1, \bar{\omega}=10$, $R_2/R_1=7.14$, $\bar{\varphi}_{TC}=\bar{\varphi}_B=1.0$.

Figure 36 displays the axial force-angle stiffnesses $\left(\overline{K}_{z\alpha_x}, \overline{K}_{z\alpha_y}\right)$ and moment-axial displacement stiffnesses $\left(\overline{K}_{\alpha_x z}, \overline{K}_{\alpha_y z}\right)$ versus TC misalignment angle. Note that $\overline{K}_{\alpha_y z} = \overline{K}_{z\alpha_y}$, just as with the aligned case (Figure 22), but the asymmetry caused by the angular misalignment results in $\overline{K}_{\alpha_x z} \neq -\overline{K}_{z\alpha_x}$, denoting a decrease in the hydrodynamic cross-coupling present when the TC is perfectly aligned with the BG.

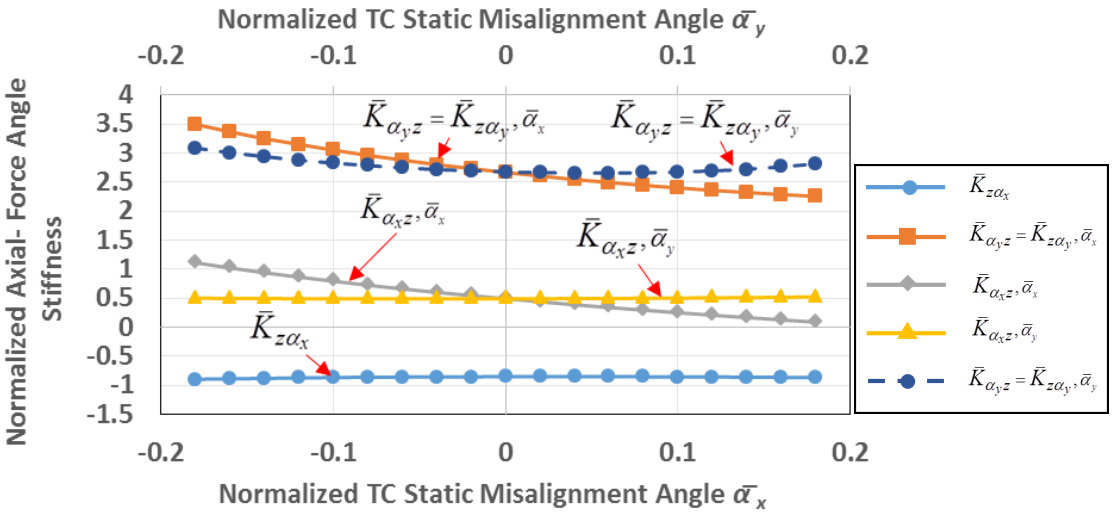

Figure 36. Axial-force angle stiffness versus thrust collar misalignment angle ($\bar{\alpha}_x$ or $\bar{\alpha}_y$). $\bar{W} = 1, \bar{\omega} = 10$, $R_2/R_1 = 7.14$, $\bar{\varphi}_{TC} = \bar{\varphi}_B = 1.0$.

Figure 37 displays the axial force damping coefficient ($\bar{C}_{zz}$) versus TC misalignment angle. $\bar{C}_{zz}$ decreases monotonically with an increase in TC misalignment angle $\bar{\alpha}_x$. In addition, note that there is no significant difference in axial damping for static misalignments $\bar{\alpha}_y$.

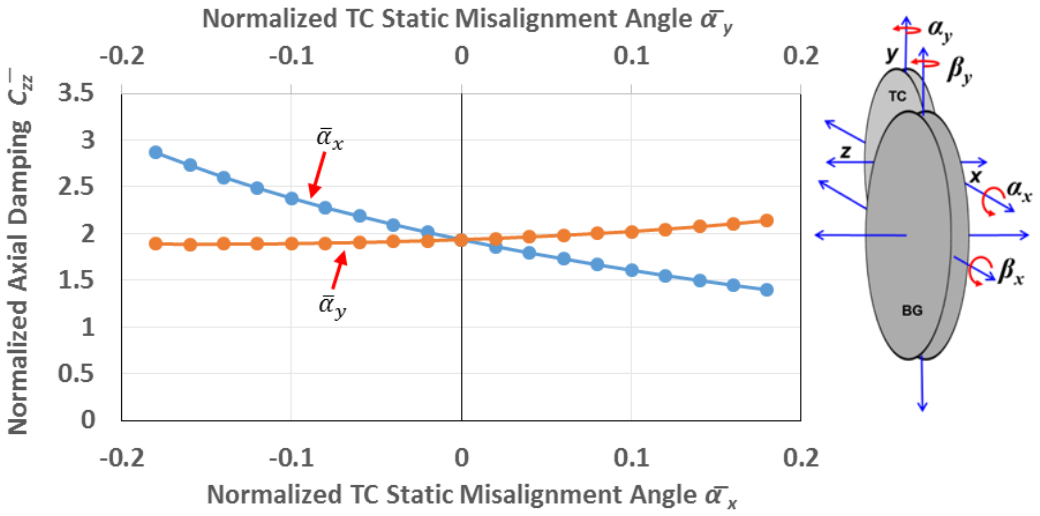

Figure 37. Axial damping coefficient ($\bar{C}_{zz}$) versus thrust collar misalignment angle ($\bar{\alpha}_x$ or $\bar{\alpha}_y$). $\bar{W} = 1, \bar{\omega} = 10$, $R_2/R_1 = 7.14$, $\bar{\varphi}_{TC} = \bar{\varphi}_B = 1.0$.

Figure 38 displays the moment-angle damping coefficients $\left(\bar{C}_{\alpha_x\alpha_x}, \bar{C}_{\alpha_y\alpha_y}, \bar{C}_{\alpha_x\alpha_y}, \bar{C}_{\alpha_y\alpha_x}\right)$ versus thrust collar misalignment angle. The direct moment-angle damping $\bar{C}_{\alpha_x\alpha_x}$ is approximately zero, regardless of the direction, or degree of the static angular misalignment. As with the aligned case ($\bar{\alpha}_x = \bar{\alpha}_y = \bar{\beta}_x = \bar{\beta}_y = 0$), the cross-coupled damping coefficients ($\bar{C}_{\alpha_x\alpha_y}, \bar{C}_{\alpha_y\alpha_x}$) are nearly zero for static misalignments of the TC about the *x* axis; however, the cross-coupled coefficient $\bar{C}_{\alpha_y\alpha_x}$ is nonzero and decreases with increasing misalignment angle $\bar{\alpha}_x$. In addition, the direct moment-angle damping coefficient $\bar{C}_{\alpha_y\alpha_y}$ decreases with an increasing angular misalignment about the *x* axis ($\bar{\alpha}_x$), but is invariant with misalignment angle $\bar{\alpha}_y$.

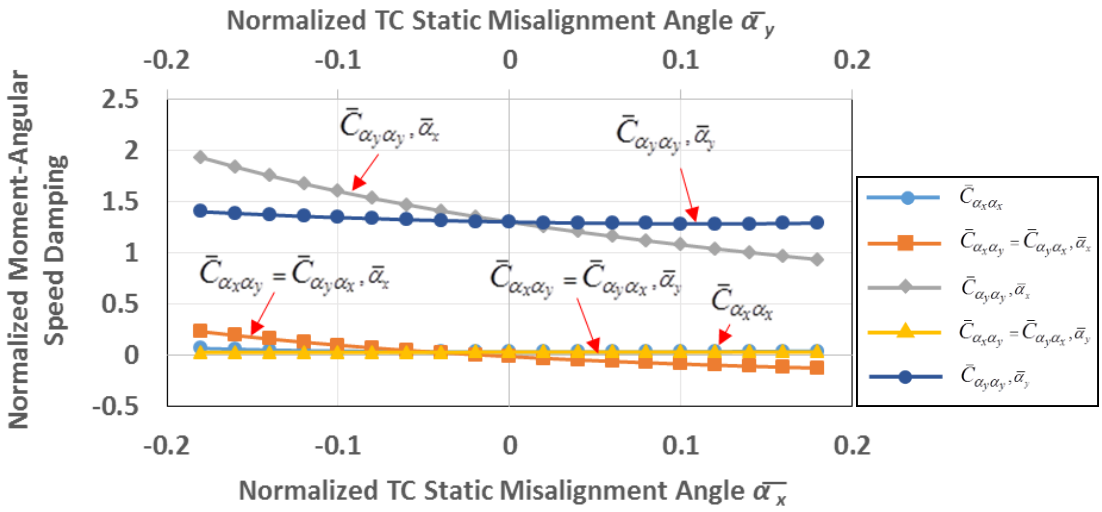

Figure 38. Moment-angular speed damping ($\bar{C}_{\alpha_x\alpha_x},\bar{C}_{\alpha_y\alpha_y},\bar{C}_{\alpha_x\alpha_y},\bar{C}_{\alpha_y\alpha_x}$) versus thrust collar misalignment angle ($\bar{\alpha}_x$ or $\bar{\alpha}_y$).
$\bar{W}=1,\bar{\omega}=10,\ R_2/R_1=7.14,\ \bar{\varphi}_{TC}=\bar{\varphi}_B=1.0$.

Figure 39 displays the axial force-angular velocity damping coefficients ($\bar{C}_{z\alpha_x},\bar{C}_{z\alpha_y}$) and moment-axial velocity damping coefficients ($\bar{C}_{\alpha_x z},\bar{C}_{\alpha_y z}$) versus thrust collar misalignment angle $\bar{\alpha}_x$ or $\bar{\alpha}_y$. The predictions in Figure 39 show that the force and moment-angle damping coefficients static misalignments do not vary with static tilts of the TC about the *y* axis ($\bar{\alpha}_y$). As with the axial-angular stiffness, $\bar{C}_{\alpha_x z}=\bar{C}_{z\alpha_x}\approx 0$ for static angular misalignments of the TC about the *y* axis; however, $\bar{C}_{\alpha_x z}$ is nonzero and

decreases with increasing misalignment angle $\bar{\alpha}_x$. Note that the coefficients $\overline{C}_{\alpha_y z} = \overline{C}_{z\alpha_y}$ decrease with increasing misalignment angle $\bar{\alpha}_x$.

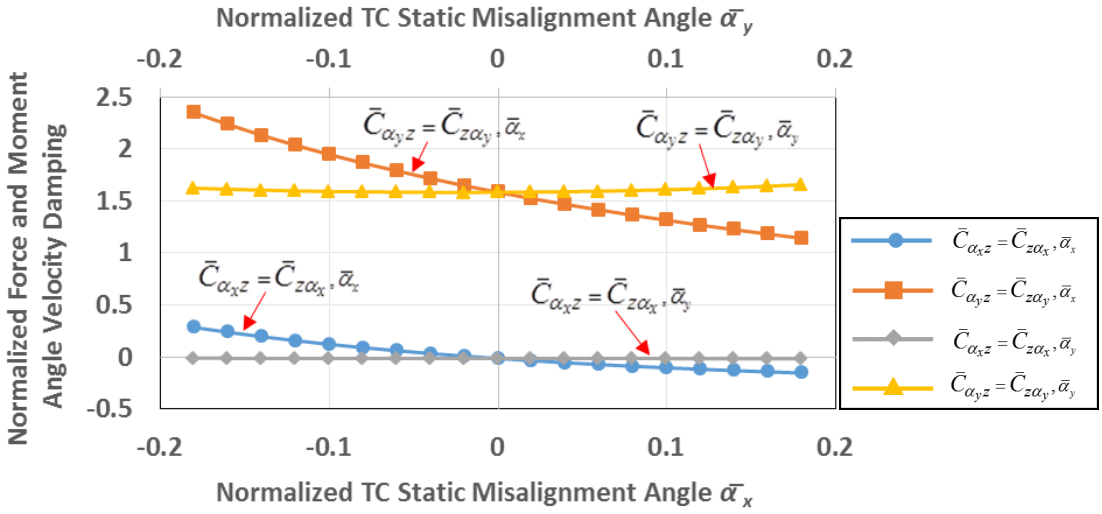

Figure 39. Force and moment-angle velocity damping ($\overline{C}_{z\alpha_x}, \overline{C}_{z\alpha_y}, \overline{C}_{\alpha_x z}, \overline{C}_{\alpha_y z}$) versus thrust collar misalignment angle ($\bar{\alpha}_x$ or $\bar{\alpha}_y$).
$\bar{W} = 1, \bar{\omega} = 10$, $R_2/R_1 = 7.14$, $\bar{\varphi}_{TC} = \bar{\varphi}_B = 1.0$.

PREDICTIONS FOR THE PERFORMANCE OF A TYPICAL THRUST COLLAR AND BULL GEAR PAIR FOR VARIOUS LOADS AND ROTATIONAL SPEEDS

The performance (mechanical power loss, stiffness and damping, etc.) of a lubricated thrust collar not only depends on the surface tapers of the TC and BG, but on the speeds of both bodies as well as the applied thrust load from the compressors stages. In industrial applications, thrust collar speeds can range anywhere from 15-45 krpm and the applied thrust loads on pinion shafts can be as high as 10 kN [18]. The following analysis presents the predicted performance of a lubricated thrust collar for a range of applied loads and rotational speeds.

For a TC/BG pair with the geometry and operating conditions displayed in Table 1, Figure 40 presents a semi-log plot of the normalized load capacity of the lubricated thrust collar versus a normalized taper difference $\Delta\bar{\varphi} = \left(\bar{\varphi}_B - \bar{\varphi}_{TC}\right)$. For the data in the following figure, the TC taper angle is held constant at $\bar{\varphi}_{TC} = 1$, while the BG taper angle varies. In addition, the speed ratio between the bull shaft and pinion shaft is $\bar{\omega} = 10$ (as in the previous two sections) and there is no static misalignment between the TC and BG $(\bar{\alpha}_x = \bar{\beta}_x = \bar{\alpha}_y = \bar{\beta}_y = 0)$.

The predictions in Figure 40 show an asymptotic behavior for the load capacity ($\bar{W}$) of a lubricated thrust collar as the difference between the two surface tapers approaches zero $(\Delta\bar{\varphi} \to 0)$. It should be noted that for very small taper differences $\Delta\bar{\varphi} < 0.1$, the

predicted load capacity of the lubricated thrust collar exceeds 15 kN (specific load capacity of $W / A_{lub} > 16.5$ MPa).

As the taper difference increases, the load capacity of the lubricated element decreases. Note that at the nominal case ($\bar{W} = 1$), the allowable taper difference is $\Delta\bar{\varphi} = \pm 0.35$. Although these predictions are presented for only a single TC/BG geometry and set of operating conditions, the following qualitative trend suggests that there is a maximum allowable taper difference for each TC/BG pair, and a situation where $\bar{\varphi}_{TC} = \bar{\varphi}_B$ is preferable for load support.

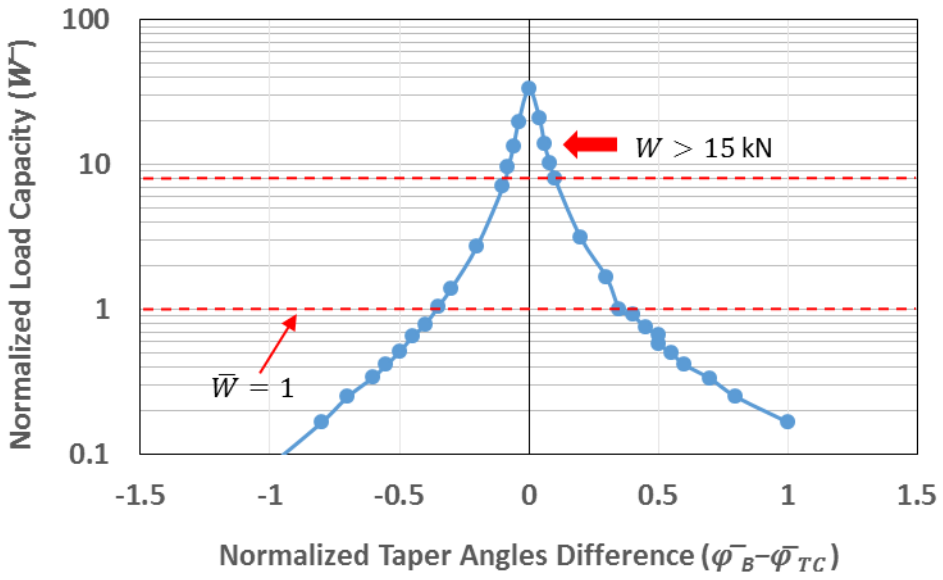

Figure 40. Normalized load capacity versus normalized difference in taper angles ($\Delta\bar{\varphi} = \bar{\varphi}_B - \bar{\varphi}_{TC}$). $\bar{\omega} = 10$, $R_2/R_1 = 7.14$, $\bar{\varphi}_{TC} = 1.0$.

The following section analyzes the effect of rotational speed $\bar{\omega}_{TC} = \omega_{TC} / \omega_{TC}^{*}$ and thrust load $\bar{W}$ on the performance parameters for a TC configuration presented in the previous sections (Table 1). The speed ratio is $\bar{\omega} = \dfrac{\omega_{TC}}{\omega_B} = 10$, a constant, while the rotational speed of both the pinion shaft and bull shaft vary. The TC/BG pairs in the following analysis have no angular misalignment $\bar{\alpha}_x = \bar{\beta}_x = \bar{\alpha}_y = \bar{\beta}_y = 0$, and have the TC taper angle equaling to the BG taper angle $\bar{\varphi}_{TC} = \bar{\varphi}_B = 2.0$.

The following figures display predictions for the performance of a TC/BG pair versus speed ($\bar{\omega}_{TC} = 0.5 - 1.5$) for three thrust loads ($\bar{W} = 0.5 - 1.5$)[10]. The ranges of TC speeds and loads span actual operating conditions for typical IGCs. As in the previous sections, the TC and BG surfaces are maintained at a constant (arbitrary) temperature of 50 °C, and heat transfer occurs by conduction and lubricant advection in the lubricated zone. The goal of the study is to determine if a currently preferred TC/BG taper angle ($\bar{\varphi}_{TC} = \bar{\varphi}_B = 2.0$) produces (for the chosen range of loads and TC speeds) a low friction factor, adequate axial stiffness and damping, low lubricant flow rate, and low lubricant temperature rise.

Figure 41 presents the normalized minimum film thickness versus normalized TC speed $\bar{\omega}_{TC}$ for a TC/BG pair under three thrust loads. Figure 41 shows that the minimum

[10] As described in a previous section, a typical load and speed combination for a TC/BG pair is $\bar{W} = 1.0,\ \bar{\omega}_{TC} = 1.0$ (this operating point is marked in the following figures).

film thickness increases with increasing speed $\bar{\omega}_{TC}$ and decreases with increasing thrust load $\bar{W}$. For the three applied thrust loads ($\bar{W} = 0.5 - 1.5$), the minimum film thickness increases by 183%, 191%, and 196%, respectively, from $\bar{\omega}_{TC} = 0.5$ to $\bar{\omega}_{TC} = 1.5$. In addition, the minimum film thickness decreases by approximately 50% over the range of applied loads $\bar{W} = 0.5 - 1.5$. This result shows that for a TC/BG pair with geometry as in Table 1, the minimum film thickness is slightly more sensitive to the applied thrust load than the rotational speed of the bull gear.

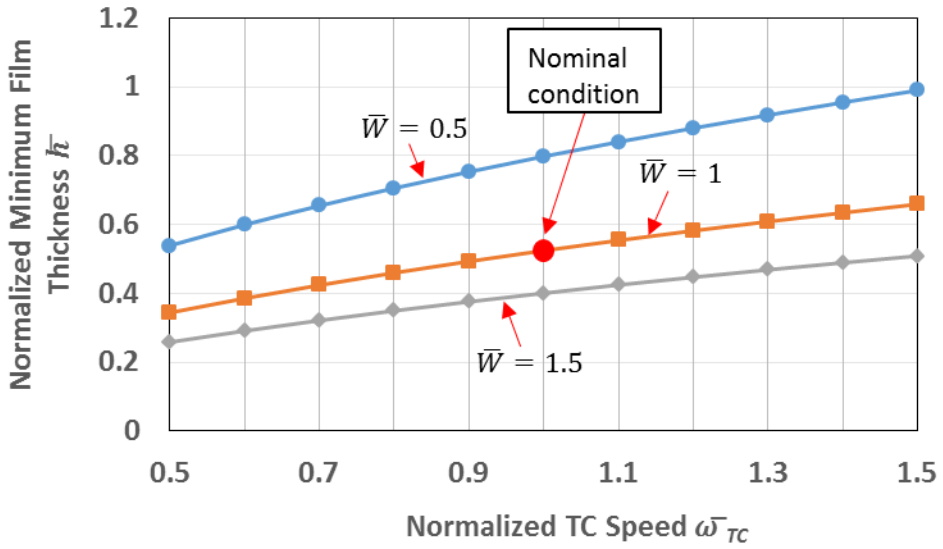

Figure 41. Minimum film thickness ($\bar{h}_{min}$) versus TC speed ($\bar{\omega}_{TC}$) for three loads. $\bar{\omega} = 10$, $\bar{\varphi}_{TC} = \bar{\varphi}_B = 2.0$, $\alpha_x = \alpha_x = \beta_x = \beta_y = 0$.

Figure 42 displays the peak hydrodynamic pressure versus TC speed ($\bar{\omega}_{TC}$) for three applied thrust loads ($\bar{W} = 0.5 - 1.5$). The predictions show that the peak hydrodynamic

pressure is nearly invariant with speed because (W / A_{lub}) is constant for each applied thrust load; however, the peak pressure is highly dependent on the applied thrust load. As with the peak hydrodynmic pressure, the shape of the hydrodynamic pressure profile, and extent of the lubricant cavitation region are also not significantly affected by the increase in TC speed $\bar{\omega}_{TC}$.

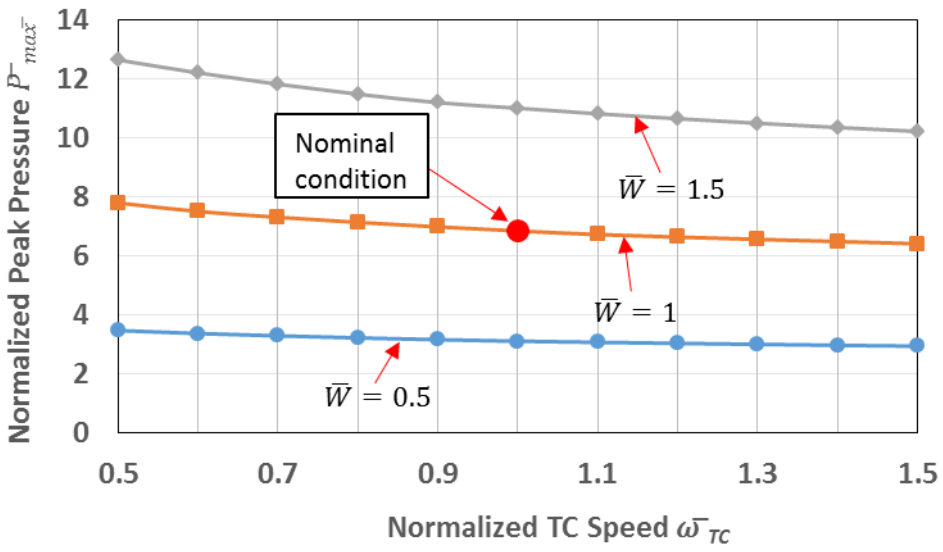

Figure 42. Peak pressure ($\bar{P}_{max}$) versus TC speed ($\bar{\omega}_{TC}$) for three loads. $\bar{\omega} = 10$, $\bar{\varphi}_{TC} = \bar{\varphi}_B = 2.0$, $\alpha_x = \alpha_x = \beta_x = \beta_y = 0$.

Figure 43 displays the friction factor (*f*) versus TC rotational speed $\bar{\omega}_{TC}$ for a TC/BG with applied thrust loads $\bar{W} = 0.5 - 1.5$. The predictions show the friction factor increases nearly linearly with the TC rotational speed $\bar{\omega}_{TC}$. In addition, note that *f* increases slightly with an increasing thrust load. Because the peak pressure (and therefore, the extrusion power loss) are nearly constant over the chosen speed range

(Figure 42), the predictions in Figure 43 denote that the power loss in a lubricated TC is mainly due to lubricant shear.

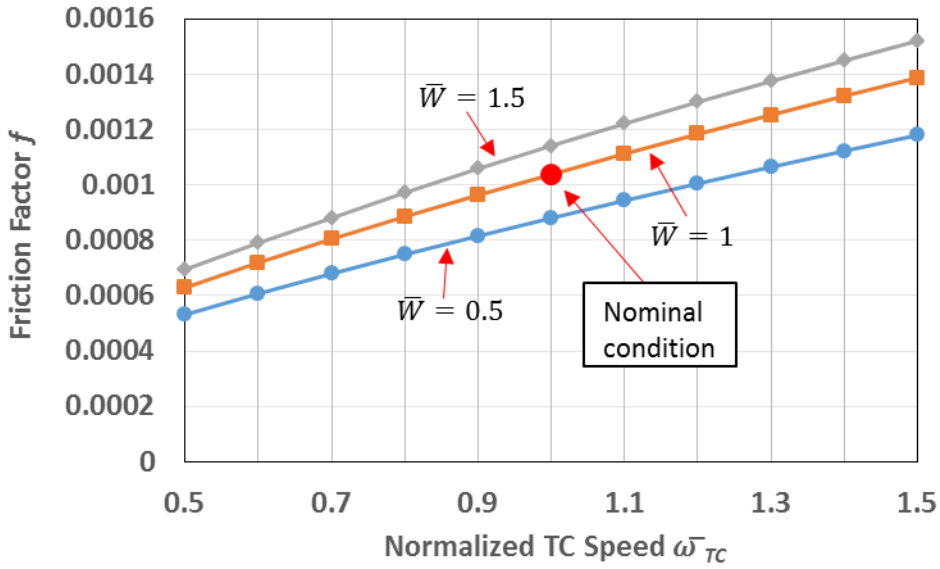

Figure 43. Friction factor (*f*) versus TC speed ($\bar{\omega}_{TC}$) for three loads. $\bar{\omega} = 10$, $\bar{\varphi}_{TC} = \bar{\varphi}_B = 2.0$, $\alpha_x = \alpha_x = \beta_x = \beta_y = 0$.

Figure 44 displays the lubricant flow rate ($\bar{Q}$) versus speed ratio ($\bar{\omega}_{TC}$) for the various loads analyzed in the previous figures. The lubricant flow rate increases linearly with the TC speed. As the speed increases, more lubricant is expelled from the lubricated zone, necessitating a larger flow rate to maintain the film thickness profile to support the applied thrust load. At low TC speed, the difference between the lubricant flow rates for the three different thrust loads is not apparent. Above $\bar{\omega}_{TC} = 1.0$, the TC/BG pair with

the lowest thrust load ($\bar{W} = 0.5$) has the largest required lubricant flow rate (and largest film thickness).

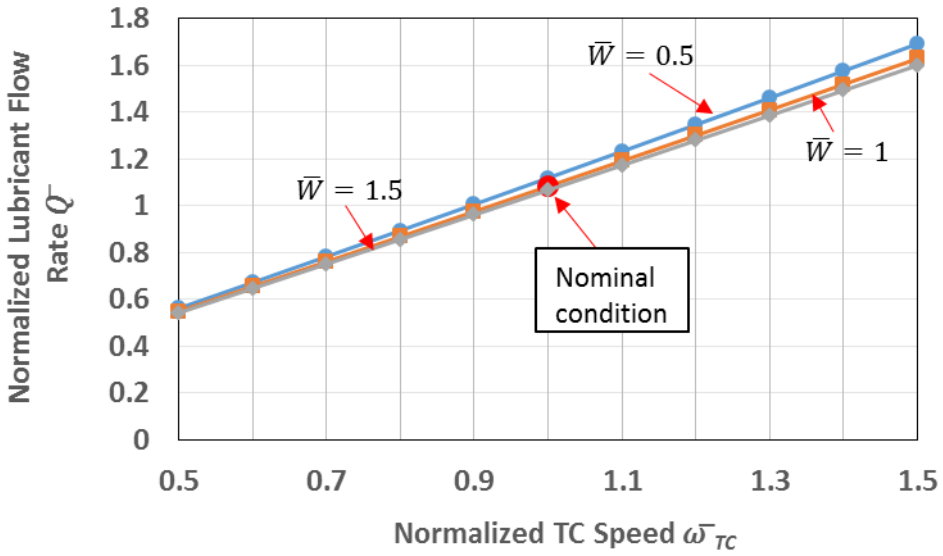

Figure 44. Lubricant flow rate ($\bar{Q}$) versus TC speed ($\bar{\omega}_{TC}$) for three loads. $\bar{\omega} = 10$, $\bar{\varphi}_{TC} = \bar{\varphi}_B = 2.0$, $\alpha_x = \alpha_x = \beta_x = \beta_y = 0$.

Figure 45 displays the lubricant temperature rise versus TC rotational speed ($\bar{\omega}_{TC}$). The qualitative trends in Figure 43 are similar to those of the friction factor, presented in Figure 43. Lubricant temperature rise is proportional to the mechanical power loss and inversely proportional to the lubricant flow rate. For the chosen range of loads and speeds, the mechancial power loss grows nearly twice as fast as the lubricant flow rate with the TC speed, leading to the increase in lubricant temperature rise with TC speed.

As with the friction factor, the lubricant temperature rise increases with increasing thrust load.

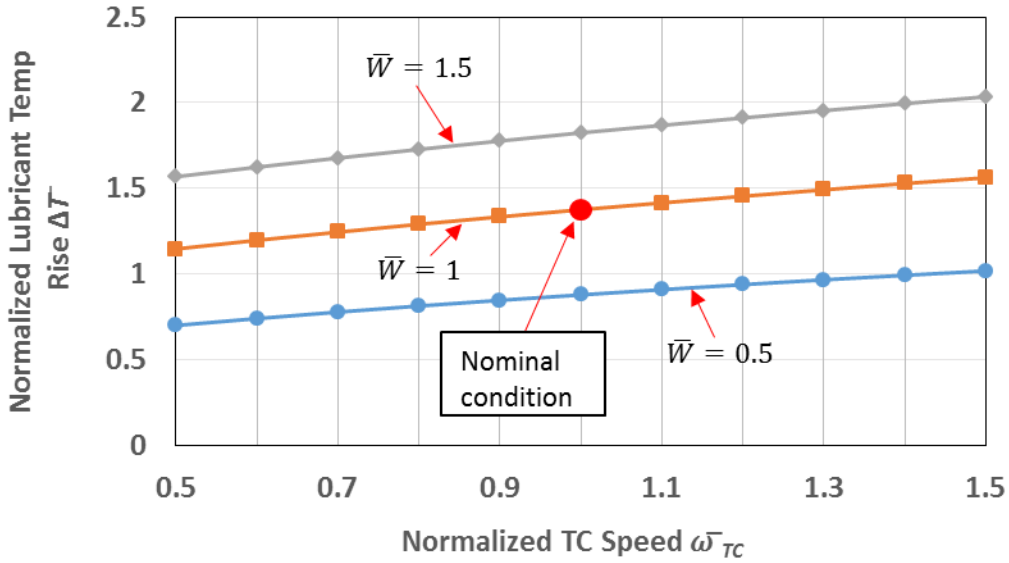

Figure 45. Lubricant temperature rise ($\Delta\bar{T}$) versus TC speed ($\bar{\omega}_{TC}$) for three loads. $\bar{\omega} = 10$, $\bar{\varphi}_{TC} = \bar{\varphi}_B = 2.0$, $\alpha_x = \alpha_x = \beta_x = \beta_y = 0$.

Figure 46 displays the fluid film axial stiffness versus rotational speed ($\bar{\omega}_{TC}$) for a TC/BG with applied thrust loads $\bar{W} = 0.5 - 1.5$. For the three thrust loads examined in the current analysis, the axial stiffness decreases by approximately 39% over the TC rotational speed range $0.5 \le \bar{\omega}_{TC} \le 1.5$. As noted earlier in Figure 41, the minimum film thickness in the lubricated zone decreases with increasing thrust load; and as such, Figure 46 shows that the fluid film axial stiffness ($\bar{K}_{zz}$) increases with the applied thrust load.

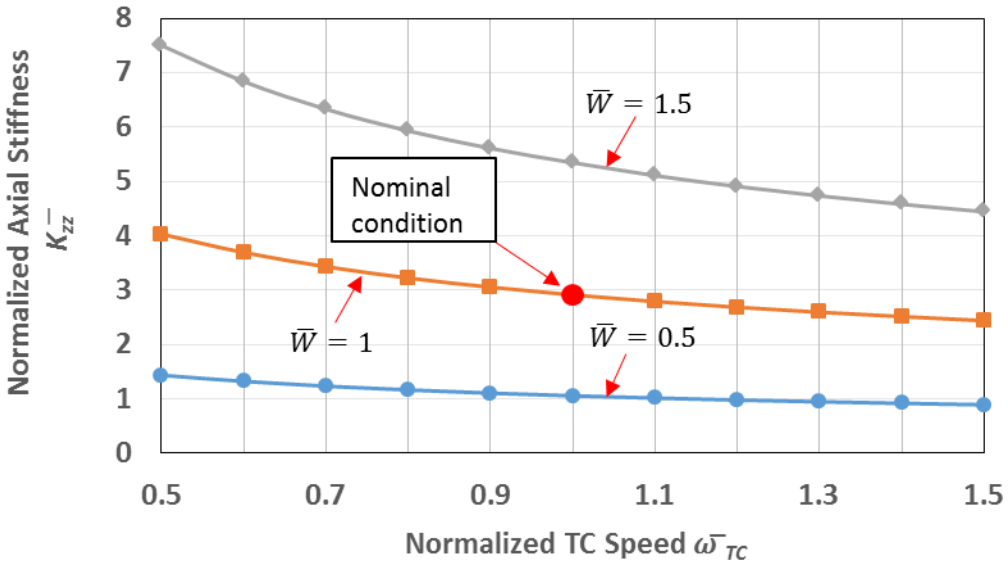

Figure 46. Axial stiffness ($\bar{K}_{zz}$) versus TC speed ($\bar{\omega}_{TC}$) for three loads. $\bar{\omega} = 10,\ \bar{\varphi}_{TC} = \bar{\varphi}_{B} = 2.0, \alpha_x = \alpha_x = \beta_x = \beta_y = 0$.

Figure 47 displays the fluid film axial damping versus TC rotational speed ($\bar{\omega}_{TC}$). The axial damping decreases with increasing speed for the three applied thrust loads. For the three applied thrust loads, the axial damping decreases by approximately 73% over the selected speed range $0.5 \le \bar{\omega}_{TC} \le 1.5$. Comparing trends in Figures 46 and 47, the fluid film axial damping is nearly twice as sensitive to the TC rotational speed as the fluid film axial stiffness (73% decrease compared to a 39% decrease).

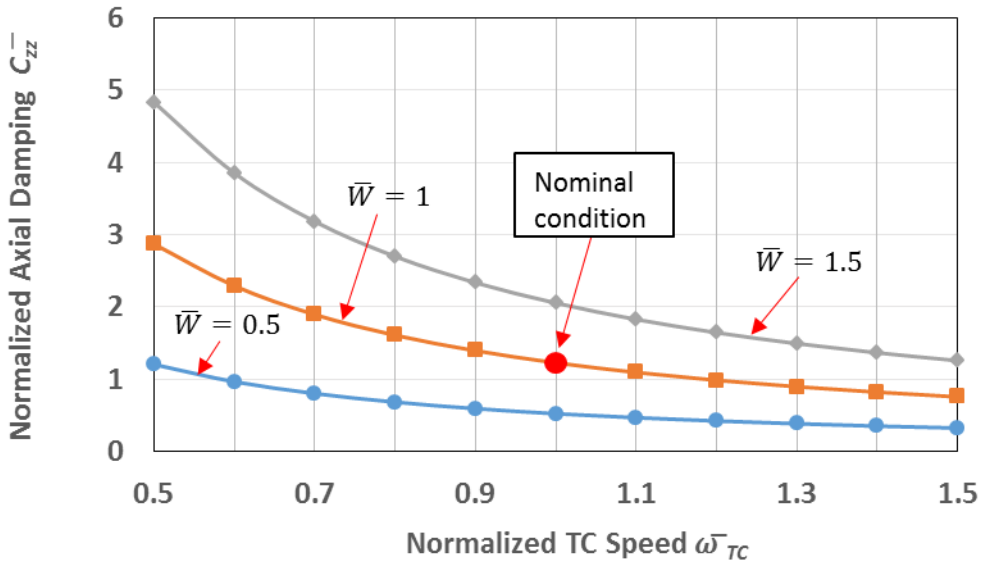

Figure 47. Axial damping ($\bar{C}_{zz}$) versus TC speed ($\bar{\omega}_{TC}$) for three loads. $\bar{\omega} = 10,\ \bar{\varphi}_{TC} = \bar{\varphi}_{B} = 2.0, \alpha_x = \alpha_x = \beta_x = \beta_y = 0$.

An axial damping ratio $\zeta = \left(\frac{1}{2}\omega^{*}_{TC} C_{zz} / K_{zz}\right) = \left(\frac{1}{2}\bar{C}_{zz} / \bar{K}_{zz}\right)$ for the thrust collar can be construed. Figure 48 displays the axial damping ratio (ζ) versus thrust collar rotational speed ($\bar{\omega}_{TC}$). At low rotational speeds ($\bar{\omega}_{TC} < 1$) the lubricated TC shows remarkably good axial damping characteristics ($0.2 \le \zeta \le 0.45$). Note that the axial damping ratio decreases by 50% over the speed range $0.5 \le \bar{\omega}_{TC} \le 1.5$ for each of the applied thrust loads.

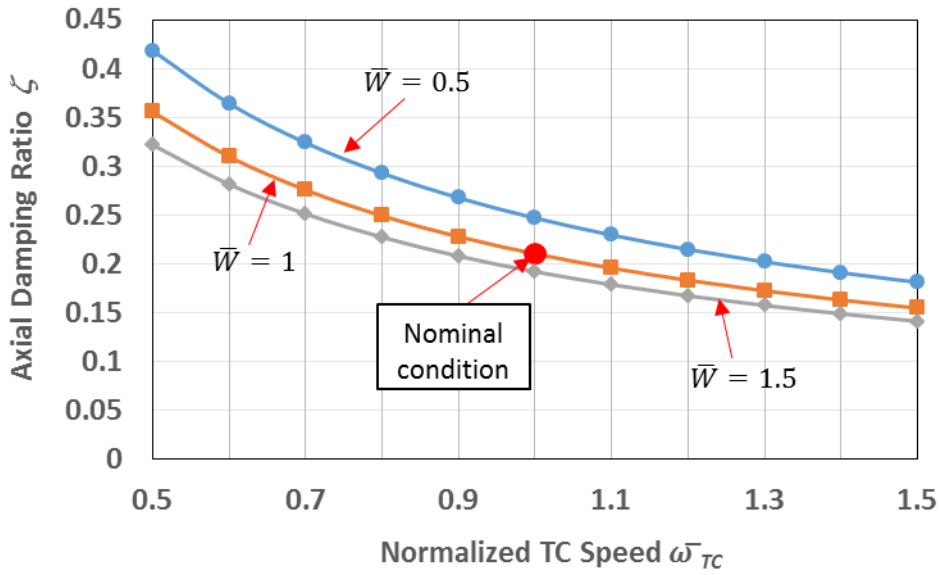

Figure 48. Axial damping ratio (ζ) versus TC speed ($\bar{\omega}_{TC}$) for three loads. $\bar{\omega} = 10$, $\bar{\varphi}_{TC} = \bar{\varphi}_B = 2.0$, $\alpha_x = \alpha_x = \beta_x = \beta_y = 0$.

Ref. [12] also presents and axial damping ratio (ζ) for a lubricated thrust collar. In. Ref. [12], the TC has a constant rotational speed ($\bar{\omega}_{TC} = 1.0$) while the applied load varies. In addition, the surface tapers of the TC and BG in Ref. [12] are $\bar{\varphi}_{TC} = \bar{\varphi}_B = 1.0$, whereas in the analysis herein, $\bar{\varphi}_{TC} = \bar{\varphi}_B = 2.0$. Because of the difference in taper angles between the two sets of predictions, the damping ratio (ζ) presented in Ref. [12] is 12% larger than ζ depicted in Figure 48, at the nominal condition ($\bar{\omega}_{TC} = 1.0$, $\bar{W} = 1.0$).

CONCLUSIONS

A thin film flow model of a lubricated thrust collar including static angle misalignments of the thrust collar and bull gear, as well as a fluid flow thermal energy transport model, are advanced to predict the forced performance of these lubricated elements in integrally geared compressors. A computational program and a graphical user interface deliver predictions for thrust collar performance, static and dynamic. The numerical model utilizes the finite element method and a Netwton-Raphson iterative scheme to determine an equilibrium film thickness for a given TC/BG geometry and set of operating conditions (speed, load, etc.). Small amplitude perturbations are introduced to the fluid film in order to determine the fluid film stiffness and damping coefficients in the axial and angular directions.

The shape of the hydrodynamic pressure field in the lubricated zone depends on the taper angle configuration of the TC/BG pair. For the specific TC/BG pair with a fixed geometry and set of operating conditions (speed, load, etc.) analyzed herein, the lubricated TC generates a hydrodynamic pressure field in the bottom half ($\theta \leq 0$) of the lubricated zone, while lubricant cavitation occurs in the top portion ($\theta > 0$). Increasing the taper angles of both the TC and BG decreases mechanical power loss and lubricant temperature rise, but also decreases the fluid film axial stiffness and damping coefficients, indicating a trade off in static and dynamic performance.

Altering the taper angles of a TC or BG from a nominal taper configuration ($\bar{\varphi}_B = \bar{\varphi}_{TC} = 1$) by a small amount ($\bar{\varphi}_B \pm 0.2, \bar{\varphi}_{TC} \pm 0.2$) does not significantly affect the static or dynamic force performance of a lubricated thrust collar. As such, existing industry (manufacturing) angular tolerances produce mechanical elements similar in performance.

Results show that the complex dynamic stiffness matrix ($K+i\omega C$) for the lubricated TC studied herein can be reduced to the form presented in Eq. (83), due to certain symmetries and asymmetries for the off diagonal elements. In addition, predictions show that some axial-force angle or rotation stiffness coefficients are nonzero, indicating a coupling between axial and angular motions for the pinion and bull gear shafts.

Static misalignments of the TC or BG can significantly affect the hydrodynamic pressure field and the extent of the lubricant cavitation region. Angular misalignments of either the TC or BG about the vertical *y* axis ($\bar{\alpha}_y, \bar{\beta}_y$) do not significantly affect the static performance (film thickness, power loss, lubricant temperature rise, etc.) of a lubricated TC; however, the fluid film stiffness and damping coefficients are sensitive to static angular misalignments $\bar{\alpha}_x, \bar{\beta}_x, \bar{\alpha}_y,$ and $\bar{\beta}_y$. Whenever the TC or BG is misaligned about the *x* axis the load carrying area in the lubricated zone changes, either increasing or decreasing (as shown in Figure 25). For a relatively large load ($\bar{W} = 1$), tilt angles ($\bar{\alpha}_x, \bar{\beta}_x = \pm 0.2$) lead to a 120% (or more) increase in peak pressure in the lubricated zone.

A larger load carrying area results in a smaller peak pressure, but also gives rise to larger shear power losses and an increase in drag friction factor.

For a TC/BG with a given geometry and set of operating conditions the load capacity of a lubricated thrust collar depends on the difference between TC and BG taper angles. When the TC taper equals the BG taper ($\bar{\varphi}_{TC} = \bar{\varphi}_B$), or when the two taper angles are nearly equal, a lubricated thrust collar can support large loads. When the TC taper angle equals the BG taper angle ($\bar{\varphi}_{TC} = \bar{\varphi}_B = 2.0$) and the TC/BG pair is perfectly aligned ($\bar{\alpha}_x = \bar{\beta}_x = \bar{\alpha}_y = \bar{\beta}_y = 0$) the predictions herein indicate that mechanical power loss and lubricant temperature rise increase with both TC rotational speed and applied thrust load. In addition, for a range of loads ($\bar{W} = 0.5 - 1.5$) and speeds ($0.5 \le \bar{\omega}_{TC} \le 1.5$), the mechanical power loss in the lubricated zone is dominated by lubricant shear. As is typical of fluid film bearings, higher thrust loads lead to an increase in fluid film axial stiffness and damping. A derived axial damping ratio indicated that the lubricated TC studied herein is underdamped ($0.2 \le \zeta \le 0.45$). Comparison of the damping ratio presented in the previous analysis and that in Ref. [12] shows that the damping ratio of a lubricated thrust collar increases with an increasing taper angle.

When designing radially tapered thrust collars for use in integrally geared compressors, designers should keep the thrust collar taper angle equal to the bull gear taper angle for an increase in load capacity. Predictions show that selecting a taper angle

of ~1° for each surface produces low mechanical power losses and lubricant temperature rise, while still providing adequate axial stiffness and damping.

In the current work the treatment of the thermal energy transport equation is simplified and local elastic deformations of the TC and BG surfaces are not considered. Future work should enhance the thermal energy transport model as well as assess the effect of elastic deformations in the lubricated zone. Currently, the predictive code for lubricated thrust collars is yet to be benchmarked against experimental data. In the near future, ongoing experiments at the Texas A&M Turbomachinery Laboratory will produce measurements for comparison with predictions from the model presented herein.

REFERENCES

[1] Wygant, K.D., 2013, "Samsung Techwin Integrally Geared Compressor," SamsungTechwin, Houston, TX, Personal Communication.

[2] Sadykov, V.A. and Shneerson, L.M, 1968, "Helical Gear Transmissions with Thrust Collars," Russian Engineering Journal – USSR, **48**, pp. 31-34.

[3] Fingerhut, U., Rothstein, E. and Sterz, G., 1991, "Standardized Integrally Geared Turbomachines – Tailor made for the Process Industry," Proceedings of the 20th Turbomachinery Symposium, Houston, TX, Sept. 17-19, pp. 131-145.

[4] Deitz, P. and Mupende, I., 2006, "Pressure ridge – An Old Machine Element with a New Potential Application," Konstruktion, **58**, pp. 69-75.

[5] Thoden, D., 2006, "Elasto-hydrodynamic Lubrication of Pressure Ridges," Mitteilungen aus dem Institut fur Maschinenwesender, TU, Clausthal, **31,** pp. 23-26.

[6] Thoden, D., 2009, "Deformation of Thick Annular Plates under Eccentric Axial Loading," Mitteilungen aus dem Institut fur Maschinenwesender, TU, Clausthal, **34,** pp. 5-12.

[7] Kucinschi, B.R., DeWitt, K.J. and Pascovisi, M.D., 2004, "Thermoelastohydrodynamic (TEHD) Analysis of a Grooved Thrust Washer," ASME J. Trib., **126**, pp. 267-274

[8] Jackson, R. and Green, I., 2001, "Study of the Tribological Behavior of a Thrust Washer Bearing," STLE Trib. Trans., **44**, pp. 504-508.

[9] Jackson, R. and Green, I., 2006, "The Behavior of Thrust Washer Bearings Considering Mixed Lubrication and Asperity Contact," Trib. Trans., **49**, pp. 233- 247.

[10] Jackson, R. and Green, I., 2008, "The Thermoelastic Behavior of Thrust Washer Bearings Considering Mixed Lubrication, Asperity Contact and Thermoviscous Effects," STLE Trib. Trans., **51**, pp. 19-32.

[11] Yu, T.H. and Sadeghi, F., 2002, "Thermal Effects in Thrust Washer Lubrication," ASME J Trib., **124**, pp. 166-177.

[12] San Andrés, L., Cable, T.A., Wygant, K. and Morton, A., 2015, "On the Predicted Performance of Oil Lubricated Thrust Collars in Integrally Geared Compressors," ASME J. Eng. Gas Turbines Power, **137 (5),** pp. 1-9.

[13] Bird, R.B., Stewart, W.E. and Lightfoot, E.N., 1960, *Transport Phenomena*, John Wiley & Sons, pp. 83, Chap. 3.

[14] Pinkus, O., 1990, *Thermal Aspects of Fluid Film Tribology*, ASME Press, New York, NY, pp. 80-85, Chap. 3.

[15] ASTM Standard D341, 2009, "Standard Practice for Viscosity-Temperature Charts for Liquid Petroleum Products," ASTM International, West Conshohocken, PA, 2003, DOI: 10.1520/C0033-03, www.astm.org.

[16] Faria, M., 1999, "Finite Element Analysis of High Speed Grooved Gas Bearings," PhD Dissertation, Mechanical Engineering Dept., Texas A&M University.

[17] San Andrés, L., 2010, *Modern Lubrication Theory,* "Thermal Analysis of Finite Length Journal Bearings Including Fluid Inertia," Notes 7, Texas A&M University Digital Libraries, http://repository.tamu.edu/handle/1969.1/93197 [07/10/13].

[18] Wygant, K.D., 2013, "Samsung Techwin Integrally Geared Compressor Experience Data," SamsungTechwin, Houston, TX, personal communication.

[19] Bejan, A. and Kraus, A., 2003, *Heat Transfer Handbook,* Volume 1, John Wiley & Sons, Inc., Hoboken, New Jersey, Ch 11.

APPENDIX A: COMPUTER IMPLEMENTATION

The hydrodynamic pressure field generated in a lubricated TC depends on the film thickness between the tapered TC and BG surfaces. For a given TC/BG geometry, and set of operating conditions (rotational speeds, lubricant viscosity, static misalignment angles, etc.), there exists a unique film thickness profile to balance the imposed thrust load from the compressor stages in an IGC. Computer implementation of the lubricated TC model, presented in Chapter 2, utilizes an algorithm to determine the film thickness between a tapered TC and BG using an iterative, Newton-Raphson based approach. The method and algorithm are similar to that for typical fluid film bearings [16].

Figure A1 presents a flow chart for finding the film thickness profile for a given TC/BG geometry and set of operating conditions. The procedure consists of two main, nested loops. The first loop determines the lubricant temperature rise for the set of operating conditions, updating the lubricant viscosity via Eq. (15), while the second (outer) loop balances the imposed thrust load by varying the film thickness and calculating the fluid film reaction force. Once the correct film thickness profile is obtained, the performance parameters (minimum film thickness, lubricant temperature rise, mechanical power loss, stiffness and damping coefficients) for the TC/BG pair are obtained.

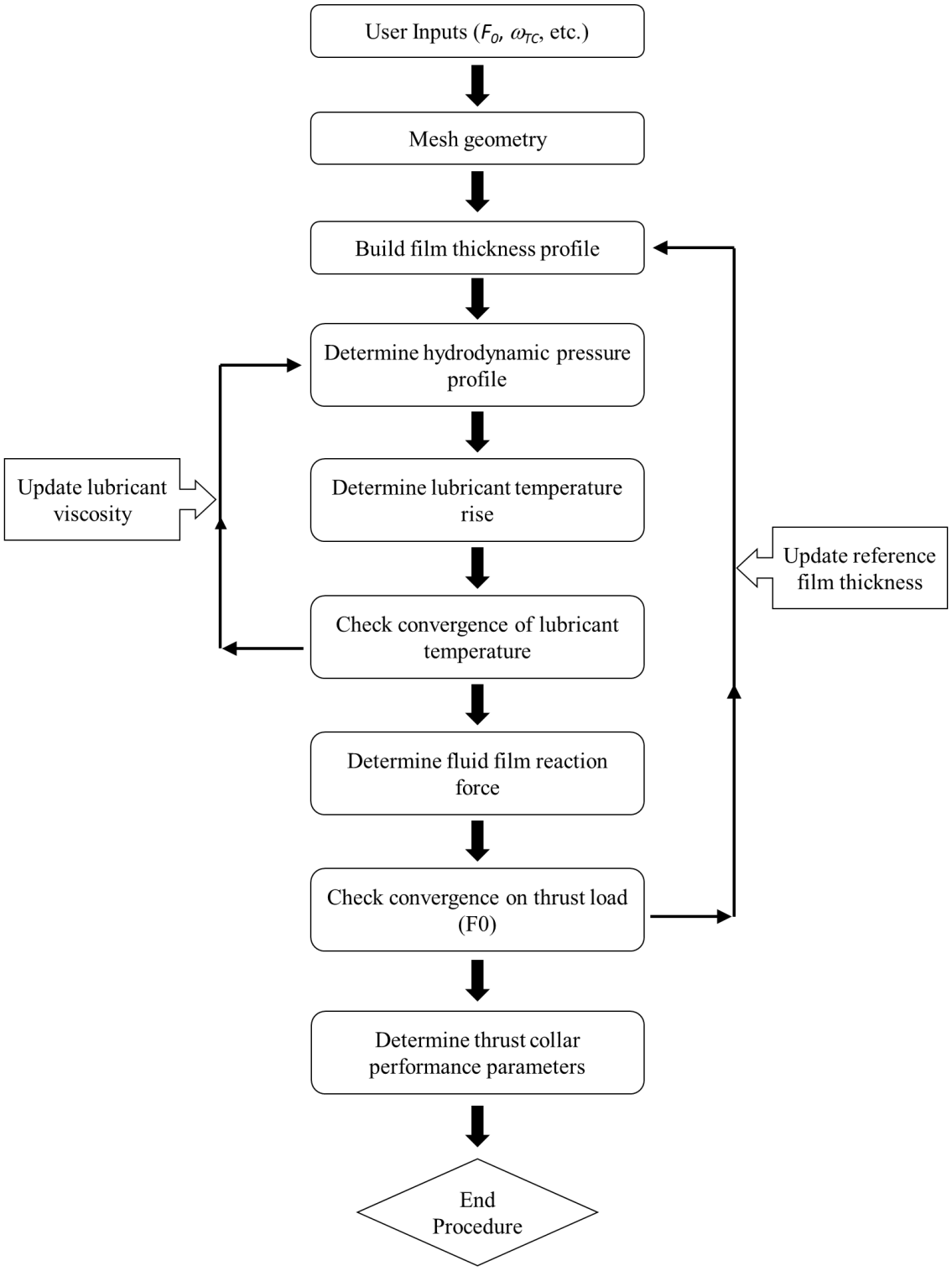

Figure A1. Flow chart for determining the operating film thickness and performance parameters of a lubricated thrust collar.

Newton-Raphson Iterative Scheme

In thin film lubrication, the magnitude of the hydrodynamic pressure field is inversely proportional to the film thickness. Based on this foundational knowledge, the numerical program described herein utilizes a common Newton-Raphson iterative scheme to update the film thickness in an attempt to balance a prescribed thrust load.

At the onset of the numerical program, the algorithm from Figure A1 builds the film thickness profile using a user supplied guess for the "reference" film thickness h_{R1}, which represents the film thickness between the TC taper and BG taper at the TC outer radius R_1, along the centerline of the thrust collar $\theta = 0$ (see Figure 4). Since there are no sources or sinks within the lubricated zone, continuity dictates that the summation of flows at the internal nodes of the domain equals to zero ($\sum q_i^e = 0$), and the zeroth order Reynolds equation (Eq. (59)) reduces to

$$\mathbf{k^e \bar{P}_0^e = f_0^e} \quad \text{or} \quad \sum_{j=1}^{n_{pe}} k_{ij}^e \bar{P}_{0i}^e = f_{0i}^e \tag{A.1}$$

For the zeroth order equation, a subroutine builds the fluidity matrix (Eq. 60) and the shear flow vector (Eq. 61) then solves the system of linear equations (Eq. (A.1)) to determine the nodal pressures $\mathbf{\bar{P}_0}$.

As described in a previous chapter, the lubricant temperature rise is based on lubricant shear and pressure extrusion, and as such, depends on the magnitude of the hydrodynamic pressure field. Once the nodal pressures are obtained, the lubricant temperature rise at each CV boundary is determined using Eqs. (73-74), and the nodal lubricant viscosity is updated via Eq. (15). The first iteration of the thermal loop (*TT*=1)

determines a reference lubricant temperature $T_{Top,1}$ for each CV boundary on which to base the convergence of the lubricant temperature. In subsequent iterations a temperature difference (ΔT) is established as

$$\Delta T_{TT} = \sum_{j=1}^{CV} T_{Top_{TT,j}} - T_{Top_{TT-1,j}} \tag{A.2}$$

Temperature iterations continue until the temperature difference between the current iteration and the previous iteration is less than a user prescribed value (ε_T).

After convergence of the lubricant temperature, the total fluid film force for the film thickness profile, established with the initial guess (h_{R1}), is determined by integrating the nodal pressures over the lubricated area,

$$F_z = \iint (p_0 - p_a) r dr d\theta \tag{A.3}$$

For the current load iteration (IT) the TC reaction force (F_z) is compared to the applied load (W) to establish a load difference (ΔF_{IT}).

$$\Delta F_{IT} = F_{z,IT} - W \tag{A.4}$$

The load difference and fluid film axial stiffness are then used to update the reference film thickness for the next load iteration.

$$h_{R_1,IT+1} = h_{R_1,IT} + \frac{\Delta F_{IT}}{K_{zz,IT}} \tag{A.5}$$

This process is repeated until the load difference (ΔF_{IT}) is less than a user prescribed value (ε_L).

APPENDIX B: MODEL FOR HEAT CONVECTION COEFFICIENTS

The heat convection coefficient ($\bar{h}$) denotes a fluid's ability to exchange heat with a bounding solid. This coefficient is extracted from the Nusselt number [19]

$$\mathrm{Nu} = \bar{h}\,\frac{D_h}{\bar{\kappa}} \tag{B.1}$$

where $\bar{\kappa}$ is the fluid thermal conductivity and D_h is the hydraulic diameter, specific to each flow geometry.

The heat convection coefficients for a TC and BG ($\bar{h}_B, \bar{h}_{TC}$) depend on the local flow condition (laminar or turbulent flow). The Nusselt number, usually empirically determined, depends on the local Reynolds number (Re) defining the flow regime, the Prandtl number $\mathrm{Pr} = \left(\frac{c_p \mu}{\bar{\kappa}}\right)$, the condition of the surface (smooth or rough textured), and also the heat flow process (constant or varying wall temperature, constant or varying heat flow into the surface), etc.

$$\mathrm{Nu} = f\left(\mathrm{Re}, \mathrm{Pr},\ \text{surface condition}\right) \tag{B.2}$$

For thermally and hydrodynamically developing laminar flow and constant wall temperatures, the Hausen model gives Nusselt numbers as [19]

$$\mathrm{Nu} = 3.657 + \frac{0.19\left(\mathrm{Re}\,\mathrm{Pr}\,\frac{D_h}{L}\right)^{0.8}}{1 + 0.117\left(\mathrm{Re}\,\mathrm{Pr}\,\frac{D_h}{L}\right)^{0.467}} \tag{B.3}$$

where L is a characteristic length and D_h is the hydraulic diameter of the flow domain.

Figure B1 displays the lubricated zone between a tapered TC and BG as a parallel channel with the associated dimensions in the body of the report (Table 1).

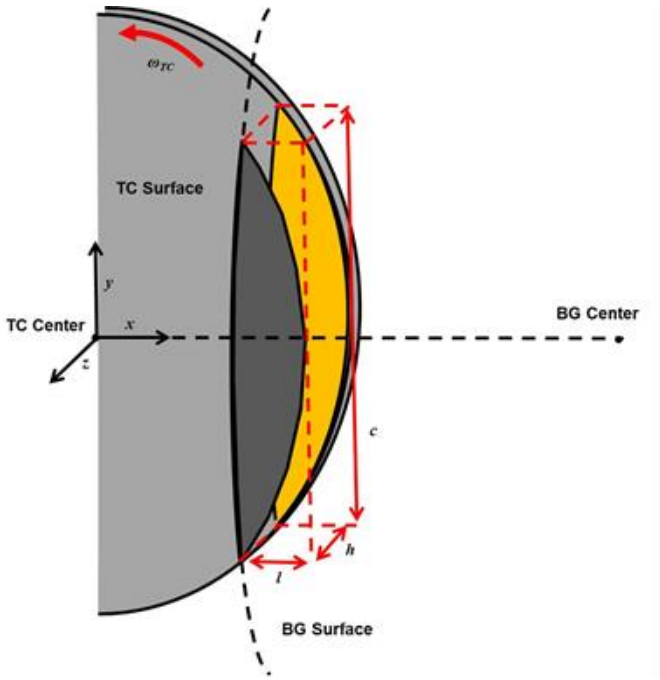

Figure B1. Depiction of the lubricated zone between a thrust collar and bull gear as a parallel channel.

The hydraulic diameter for the parallel channel depicted in Figure B1 is

$$D_h = 2\left(\frac{h_{avg} l}{h_{avg} + l}\right) \tag{B.4}$$

where h_{avg} is the average film thickness is the lubricated zone, and l is the width of the lubricated zone at $\theta = 0$. Likewise, the characteristic length (L in Eq. (B.3)) of the parallel channel is equal to the height of the lubricated zone (c).

Typically, fluid flows transition from laminar to turbulent flow at Re~2,300 [19]. To assess the flow condition in a TC, Reynolds numbers are defined from the fluid mean velocity and in relation to the surface speeds of the thrust collar ($V_{TC} = r\omega_{TC}$) and bull gear ($V_B = b_{(r,\theta)}\omega_{TC}$) are

$$\mathrm{Re}_{TC} = \frac{\rho h}{\mu}\left[\left(\bar{V}_r - V_{r_{TC}}\right)^2 + \left(\bar{V}_\theta - V_{\theta_{TC}}\right)^2\right]^{1/2} = \frac{\rho h}{\mu}\left[\bar{V}_r^2 + \left(\bar{V}_\theta - r\omega_{TC}\right)^2\right]^{1/2}$$
$$\mathrm{Re}_{B} = \frac{\rho h}{\mu}\left[\left(\bar{V}_r - V_{r_B}\right)^2 + \left(\bar{V}_\theta - V_{\theta_B}\right)^2\right]^{1/2} = \frac{\rho h}{\mu}\left[\left(\bar{V}_r - b\omega_B \sin(\varepsilon)\right)^2 + \left(\bar{V}_\theta - b\omega_B \cos(\varepsilon)\right)^2\right]^{1/2}$$

(B.5)

Where the radial and tangential components of the mean fluid flow velocity are [16]

$$\bar{V}_r = \frac{q_r}{h} = -\frac{h^2}{12\mu}\frac{\partial p}{\partial r} + \frac{1}{2}\left(b\omega_B \sin(\varepsilon)\right)$$
$$\bar{V}_\theta = \frac{q_\theta}{h} = -\frac{h^2}{12\mu}\frac{\partial p}{r\partial \theta} + \frac{1}{2}\left(b\omega_B \cos(\varepsilon) + r\omega_{TC}\right) \qquad \text{(B.6)}$$

With the definitions of the Reynolds numbers (Eq. (B.5)) and the Nusselt numbers determined with the Hausen model (Eq. (B.6)), Eq. (B.1) is rearranged to render expressions for the heat convection coefficients towards the TC and BG surfaces.

$$\bar{h}_{TC} = \mathrm{Nu}_{TC}\frac{\bar{\kappa}}{D_h}$$
$$\bar{h}_{B} = \mathrm{Nu}_{B}\frac{\bar{\kappa}}{D_h} \qquad \text{(B.7)}$$